Development of methodologies for X-ray diffraction at ultra low temperatures

JONATHAN ALEXANDER COOME

Development of Methodologies for X-ray Diffraction at Ultra Low Temperatures

Jonathan A. Coome

Thesis presented in part fulfilment of the requirements for the degree of
Doctor of Philosophy

Department of Chemistry
Durham University
May 2012

Abstract

The Xiphos is a new diffractometer that has been been designed and built to determine the solid-state structures of materials at ultra low temperatures. As one of very few single-crystal X-ray diffractometers capable of collecting diffraction data from crystals cooled to 2 K, the Xiphos has an enormous potential for improving our understanding of the relationship between the solid-state structure and the physical properties of many materials which show interesting and valuable behaviour at ultra low temperatures. However, there are some challenges to collecting good quality data due to the beryllium vacuum shrouds surrounding the crystal which are necessary components of the cryostat used for reaching these low temperatures.

A new program called *Masquerade* is described that helps to overcome these challenges by generating 'masks' describing the position of the beryllium scattering from the vacuum shrouds. These masks can be used during data integration to prohibit measuring the diffracted intensities of X-ray reflections which are contaminated by beryllium scattering. A new protocol for data collection is also presented to recover the reflection intensities that are missing as a result of the masks. Results are presented showing a marked improvement in the accuracy of the reflection intensities which can be obtained from diffraction patterns collected with the Xiphos when the data have been contaminated by beryllium scattering from the vacuum shrouds.

Several additional computer programs have been developed which enhance the data collection process by monitoring the sample temperature and offering the ability to monitor the status of the Xiphos and the progress of a diffraction experiment remotely. The development and use of these programs is described herein.

To show the Xiphos and *Masquerade* in action, structural studies at a range of temperatures between 2 K and 160 K are presented on charge-transfer complexes which exhibit superconductivity below 7 K, in addition to studies at ultra low temperatures of spin-crossover complexes, organic radicals and single molecular magnets. The relationship between the solid-state structure and interesting physical properties can be better understood by determining the structure at the same temperatures at which the properties are exhibited; a process that can now be undertaken routinely in a university laboratory with the Xiphos.

Declaration

The work described in this thesis was carried out at the University of Durham between October 2008 and December 2011 under the supervision of Dr Andrés E. Goeta and Prof. Judith A. K. Howard. Unless otherwise stated all the work is my own and has not been submitted previously for the award of a higher degree at this or any other university.

Acknowledgements

Firstly I would like to thank my supervisor Andrés Goeta for his support and guidance throughout the first two and a half years of this project until his untimely death in 2011. He is missed.

Many thanks also go to my co-supervisor Judith Howard for her help and support throughout the project, especially during its completion and the preparation of this thesis.

I would also like to thank Mike Probert for day-to-day guidance, teaching me the intricacies of the Xiphos and the control software and for help with crystal structure analysis when I needed it.

Thanks go to everyone who has been part of the Durham crystallography group while I've been there for their help and advice. In particular I would like to thank Helena for all her help in getting to grips with the practicalities of crystal structure solution and refinement, and Hazel, Dima, Olga, Horst and Oleg for answering many questions.

My thanks go to my collaborators on this project: Peter Day, Hiroki Akutsu, Malcolm Halcrow, Jeremy Rawson and Andrew Farrell. They have provided many interesting and challenging crystals to study and many interesting discussions about the results of these experiments.

Finally, I would like to thank my family and friends for all their love and support, and thanks go especially to Lizzy, for everything.

Contents

1 Introduction **1**
1.1 Diffraction Theory . . . 1
1.1.1 The Reciprocal Lattice . . . 2
1.1.2 Structure Factors . . . 3
1.1.3 Symmetry . . . 4
1.1.4 Diffraction Geometry . . . 5
1.1.4.1 Detector Calculations . . . 7
1.1.4.2 Goniometer Calculations . . . 7
1.1.4.3 Calculating Goniometer Angles for a Reflection . . . 8
1.2 Low Temperature Crystallography . . . 10
1.2.1 Sample Cooling Methods . . . 11
1.2.1.1 Nitrogen Based Cryostats . . . 11
1.2.1.2 Helium Based Cryostats . . . 12
1.2.2 Applications . . . 14
1.2.2.1 Routine Use of Low Temperature . . . 14
1.2.2.2 Study of Liquids and Gases . . . 15
1.2.2.3 Studying Changes in Material Properties . . . 15
1.2.3 Conclusions . . . 16

2 The Xiphos Diffractometer **17**
2.1 System Components . . . 18
2.2 Configuring the System . . . 20
2.2.1 Alignment . . . 20
2.2.1.1 Adjusting the Optics . . . 20
2.2.1.2 Generator . . . 22
2.2.2 The Displex . . . 24
2.2.2.1 Calibration . . . 24
2.2.2.2 Vacuum Shrouds . . . 24
2.3 Running Diffraction Experiments . . . 27
2.3.1 Sample Mounting . . . 27
2.3.2 Crystal Centring . . . 28
2.3.2.1 Known Corrections . . . 29
2.3.2.2 Moving the Crystal . . . 30
2.3.3 Data Collection . . . 31
2.4 A Study of *m*-Nitroaniline . . . 32
2.5 Conclusions . . . 34

3 *Masquerade*: Generating Masks for Beryllium Rings **35**

3.1 The Distance Between the Crystal and the Shroud Wall . . . 37
3.1.1 Initial Approach . . . 37
3.1.2 Ray-Casting . . . 39
3.2 Calculating the Offsets . . . 42
3.3 Generating the Masks . . . 45
3.3.1 Mask Format . . . 46
3.4 Cytidine at 100 K . . . 47
3.4.1 Generating the Masks . . . 47
3.4.2 Results . . . 50
3.5 Cytidine at 2 K . . . 53
3.6 Conclusions . . . 55

4 Superconducting Charge-Transfer Salts 57
4.1 Introduction . . . 57
4.1.1 BEDT-TTF Salts Containing Tris(oxalato)metallate(III) Anions . . . 58
4.2 β″–(BEDT–TTF)$_4$[(H$_3$O)Ga(C$_2$O$_4$)$_3$]PhNO$_2$ . . . 60
4.2.1 Experimental . . . 60
4.2.2 Results and Discussion . . . 61
4.2.2.1 Space Group Setting . . . 62
4.2.2.2 Unit Cell Parameters . . . 63
4.2.2.3 Charge Separation . . . 64
4.2.2.4 Structure Disorder . . . 66
4.2.2.5 Rotation of the Nitro Group in Nitrobenzene . . . 67
4.2.2.6 Summary . . . 68
4.3 β″–(BEDT–TTF)$_4$[(H$_3$O)Fe(C$_2$O$_4$)$_3$]PhNO$_2$ . . . 69
4.4 β″–(BEDT–TTF)$_4$[(H$_3$O)Fe(C$_2$O$_4$)$_3$]PhCN . . . 71
4.5 Conclusions . . . 72

5 Spin Crossover Complexes 74
5.1 Introduction . . . 74
5.1.1 Complexes with 2,6-di(pyrazol-1-yl)pyridine . . . 76
5.2 Experimental . . . 77
5.3 Results and Discussion . . . 79
5.3.1 [CoL$_2$](BF$_4$)$_2$ . . . 79
5.3.2 [NiL$_2$](BF$_4$)$_2$ . . . 81
5.3.3 [ZnL$_2$](BF$_4$)$_2$ . . . 83
5.3.3.1 Improving the Data with *Masquerade* . . . 83
5.3.3.2 Results . . . 85
5.3.4 Comparisons . . . 85
5.4 Conclusions . . . 87

6 Organic Radicals and Single Molecule Magnets 89
6.1 Spin Transitions in 3-cyanobenzo-1,3,2-dithiazolyl . . . 89
6.1.1 Experimental . . . 90
6.1.2 Results and Discussion . . . 92
6.1.3 Conclusions . . . 92
6.2 A Study of *para*-Chloroanilinium Tetrachlorocuprate . . . 94

6.2.1 Experimental . . . 94
6.2.2 Results and Discussion . . . 95
6.2.2.1 Low Temperature Studies . . . 96
6.2.3 Conclusions . . . 98
6.3 Single Molecule Magnets . . . 98
6.3.1 A Low Temperature Study of Mn_{12} Acetate . . . 99
6.3.2 A Low Temperature Study of a Mn_3 Cluster . . . 101
6.3.3 Low Temperature Studies of a Co_4 Citrate Cluster . . . 105
6.3.4 Conclusions . . . 108

7 Ancillary Programs **109**
7.1 Xiphos Tools . . . 109
7.1.1 BIS . . . 109
7.1.2 libbis . . . 110
7.1.3 Bis2Shore . . . 111
7.1.3.1 LakeShore Controller . . . 111
7.1.3.2 Program Execution . . . 113
7.1.4 Ramp . . . 114
7.1.4.1 Strategy Generation . . . 115
7.1.4.2 Execution . . . 116
7.1.5 XiSpy . . . 117
7.1.5.1 Displex Temperature . . . 119
7.1.5.2 Recent Frame . . . 119
7.1.5.3 Status Page Generation . . . 121
7.2 libcrystal . . . 122
7.2.1 Space Groups . . . 123
7.2.1.1 Background . . . 123
7.2.1.2 Code . . . 124
7.2.2 Goniometer Calculations . . . 125
7.2.3 Input/Output . . . 126
7.2.3.1 Bruker Frame Files . . . 127
7.2.3.2 Bruker P4P Files . . . 128
7.3 Conclusions . . . 130

8 Conclusions and Future Work **131**
8.1 The Xiphos Diffractometer . . . 131
8.2 *Masquerade* . . . 132
8.3 Future Work . . . 134

A Conferences, Schools and Presentations **136**
A.1 Conferences and Meetings . . . 136
A.2 Schools . . . 137
A.3 Publications . . . 137

B Experimental Data for Charge Transfer Salts **138**

References **144**

List of Figures

1.1 A representation of the geometry which is used as the basis of Bragg's Law. . 2
1.2 The Ewald sphere construction. 3
1.3 A diagram to show the geometry of a Eulerian cradle. 6
1.4 The coordinate system used by (a) Busing & Levy, and (b) Bruker. 6

2.1 The Xiphos diffractometer, with labels describing major components. 18
2.2 The primary beam as seen on the detector during alignment. 21
2.3 The position of the adjustment bolts of the X-ray source. 22
2.4 Simulated precession images for the h k 0 planes of $NH_4H_2PO_4$. 25
2.5 The β angle of the benzil unit cell as a function of temperature. 25
2.6 The splitting of the (0 0 12) reflection from the (0 −12 0) reflection in $TbVO_4$. 26
2.7 The splitting of the (0 0 6) reflection from the (0 6 0) reflection in $DyVO_4$. . 26
2.8 A diagram of the 'chuck' style sample holder. 28
2.9 The molecular structure of **1** at 2 K, showing atom labels. 33

3.1 Scattered beam vectors of reflections from the sample and a vacuum shroud. 37
3.2 The distance between the crystal and shroud walls as a function of ω and χ. . 38
3.3 The distance between the shroud wall and the crystal with offsets. 43
3.4 Calculating the shroud offsets. 44
3.5 An example mask image from the diffraction pattern of **6** at 2 K. 45
3.6 A comparision of the structures of **2** at 100 K with and without masks. 50
3.7 The molecular structure of **2** at 2 K. 54

4.1 The molecular structures of TCNQ and TTF. 58
4.2 The molecular structure of BEDT-TTF. 58
4.3 The crystal packing of **3a** at 160 K, perpendicular to the *a* axis. 61
4.4 The asymmetric unit of **3a** at 160 K. 62
4.5 The variation of unit cell volume in **3a** (crystal 1) with temperature. 64
4.6 The four bonds in the BEDT-TTF molecule used to calculate partial charges. 65
4.7 Partial charges for both independent BEDT-TTF molecules in **3a**. 65
4.8 The oxalate anion layer in **3a** at 160 K and 2 K. 67
4.9 The rotation of the nitrobenzene molecule with temperature. 68
4.10 The asymmetric unit of **3b** at 2 K. 70
4.11 The asymmetric unit of **3c** at 120 K. 71

5.1 The splitting of the *d*-orbitals as a function of the ligand-field strength. . . . 75
5.2 The 2,6-di(pyrazol-1-yl)pyridine ligand (L). 76
5.3 Variable temperature magnetic susceptibility curve of **4a**. 78
5.4 The molecular structure of **4a** at 2 K. 80

5.5 The molecular structure of **4b** at 2 K. 82
5.6 The molecular structure of **4c** at 2 K. 84

6.1 The formula of 3-cyanobenzo-1,3,2-dithiazolyl, **5**. 89
6.2 Views of the packing in **5** at 2 K. 91
6.3 The magnetic susceptibility, χ, of **6** between 5 K and 300 K. 95
6.4 Comparison of the packing in **6** at 290 K and 3 K. 96
6.5 The asymmetric unit of **6** at 290 K and 3 K. 97
6.6 The molecular structure of **7** at 2 K. 100
6.7 The structural formula of the salicylaldoxime ligand, Et–saoH_2. 101
6.8 The molecular structure of **8** at 2 K. 102
6.9 A diagram showing selected intermolecular hydrogen bonding in **8** at 2 K. . 103
6.10 Crystals of **9** under polarised light. 105
6.11 The molecular structure of **9** at 2 K. 106
6.12 Simulated precession images of **9** between 100 K and 2 K. 107

7.1 The main *Bis2Shore* interface. 111
7.2 The main *Ramp* interface, before strategy generation. 114
7.3 The main *Ramp* interface after strategy generation. 115
7.4 The main *XiSpy* interface. 118
7.5 An example image produced during a data collection by *XiSpy*. 120
7.6 An example of the status page generated during a data collection by *XiSpy*. . 121

List of Tables

2.1 The φ scans used as 'standard' to centre a crystal on the Xiphos. 29
2.2 The known corrections used after three recent machine alignments. 30
2.3 Crystal data and structure refinement of **1** at 2 K. 33

3.1 Calculating the distance between the shroud wall and the crystal in **2**. 48
3.2 The calculated shroud offsets using the distances in Table 3.1. 48
3.3 A comparison of the data quality observed with and without masks. 50
3.4 The number of reflections that could be integrated with and without masking. 51
3.5 The number of reflections regained with two detector distances. 51
3.6 A comparison of data quality with masks and two detector distances. 52
3.7 The number of reflections integrated with increasing detector distances. . . . 52
3.8 A comparison of unit cell parameters at 100 K and 123 K. 53
3.9 Crystal data and structure refinement for **2** at 2 K 54

4.1 The number of *c*-glide systematic absence violations with temperature. . . . 63
4.2 Changes in the unit cell parameters in **3a** between 160 K and 2 K. 63
4.3 Crystal data and structure refinement of **3b** at 2 K. 70

4.4 Crystal data and structure refinement of **3c** at 120 K. 72

5.1 Differences in unit cell parameters on cooling from 50 K to 2 K. 79
5.2 Crystal data and structure refinement of **4a** 80
5.3 Co–N bond lengths at each of the temperatures measured. 81
5.4 Ni–N bond lengths at 2 K and 150 K. 81
5.5 Crystal data and structure refinement of **4b** at 2 K. 82
5.6 Shroud offsets calculated for **4c** at 2 K and 50 K. 83
5.7 Crystal data and structure refinement of **4c** at 2 K and 50 K. 84
5.8 Zn–N bond lengths at 2 K, 50 K and 100 K in **4c**. 85
5.9 The Flack parameters for the crystal structures of **4a**, **4b** and **4c** at 2 K. 86
5.10 Selected bond angles (°) for all three complexes at 2 K. 86

6.1 Shroud offsets calculated for **5** at all the temperatures measured. 90
6.2 Selected atomic distances for **5** at the four temperatures measured. 91
6.3 Parameters from the masked and unmasked refinements of **5**. 92
6.4 Crystal data and structure refinement of **5** at the temperatures measured. . . 93
6.5 Selected bond lengths and atomic distances in **6**. 96
6.6 Crystal data and structure refinement of **6** at various temperatures. 97
6.7 Crystal data and structure refinement of **7** at 2 K. 100
6.8 Crystal data and structure refinement of **8**. 103
6.9 Selected bond lengths and atomic distances in **8** at 2 K and 150 K 104
6.10 Crystal data and structure refinement of **9**. 106

7.1 The commands used by *Bis2Shore* to communicate with the LakeShore. . . . 112
7.2 Example strategy to power the generator from standby to 40 kV and 30 mA. 116
7.3 The status messages sent by *BIS* which are used by *XiSpy*. 118

B.1 Crystal data and structure refinement of **3a** (crystal 2) in $C2/c$. 138
B.2 Crystal data and structure refinement of **3a** (crystal 2) in $P\bar{1}$. 139
B.3 Crystal data and structure refinement of **3a** (crystal 1) in $C2/c$. 140
B.4 Crystal data and structure refinement of **3a** (crystal 1) in $C2/c$ (cont). 141
B.5 Crystal data and structure refinement of **3a** (crystal 1) in $P\bar{1}$. 142
B.6 Crystal data and structure refinement of **3a** (crystal 1) in $P\bar{1}$ (cont). 143

List of Abbreviations

Compounds

1 *m*-Nitroaniline (Chapter 2)
2 Cytidine (Chapter 3)
3a β''–(BEDT–TTF)$_4$[$(H_3O)Ga(C_2O_4)_3$]$PhNO_2$ (Chapter 4)
3b β''–(BEDT–TTF)$_4$[$(H_3O)Fe(C_2O_4)_3$]$PhNO_2$ (Chapter 4)
3c β''–(BEDT–TTF)$_4$[$(H_3O)Fe(C_2O_4)_3$]PhCN (Chapter 4)
4a $[CoL_2](BF_4)_2$, where L = 2,6-di(pyrazol-1-yl)pyridine (Chapter 5)
4b $[NiL_2](BF_4)_2$, where L = 2,6-di(pyrazol-1-yl)pyridine (Chapter 5)
4c $[ZnL_2](BF_4)_2$, where L = 2,6-di(pyrazol-1-yl)pyridine (Chapter 5)
5 3-cyanobenzo-1,3,2-dithiazolyl (Chapter 6)
6 $[p\text{–}ClC_6H_4NH_3]_2CuCl_4$ (Chapter 6)
7 Mn_{12}-acetate, $[Mn_{12}O_{12}(CH_3COO)_{16}(H_2O)_4] \cdot 4\,H_2O \cdot 2\,CH_3COOH$ (Chapter 6)
8 $[Mn_3O(Et\text{–}sao)_3(ClO_4)(MeOH)_3]$ (Chapter 6)
9 $[C(NH_2)_3]_8\{Co_4(citrate)\}.4\,H_2O$ (Chapter 6)

Abbreviations

ASCII	American standard code for information interchange
BEDT-TTF	Bis(ethylenedithio)-tetrathiafulvalene
CCD	Charge-coupled device
CCR	Closed-cycle refrigerator
CR	Carriage return character (‘\r’)
CSV	Comma separated value
CT	Charge-transfer
Et	Ethyl
GUI	Graphical user interface
HS	High spin
LF	Line-feed character (‘\n’)
LIESST	Light induced excited spin state trapping
LS	Low spin
Ph	Phenyl
SCO	Spin crossover
SMM	Single molecule magnet

SQUID	Superconducting quantum interference device
SXRD	Single-crystal X-ray diffraction
TCNQ	Tetracyanoquinodimethane
TMTSF	Tetramethyltetraselenafulvalene
TTF	Tetrathiafulvalene
TXS	Turbo X-ray source

Chapter 1

Introduction

Single-crystal X-ray diffraction (SXRD) is a powerful analytical technique, enabling the atomic structure of a crystal to be determined. Atoms in crystals are arranged in a regularly spaced repeating lattice, and since the wavelength of X-rays is of the same order of magnitude as the interatomic spacing of molecules in the lattice, the incoming X-ray beam can be diffracted in a coherent pattern from the crystal. The beam is scattered in all directions by each of the atoms in the crystal and these scattered X-rays undergo constructive and destructive interference so that the scattered beams are only observed in particular directions.

The first diffraction pattern was recorded from a crystal of copper sulphate by Max von Laue, Walter Friedrich and Paul Knipping in 1912, one hundred years ago. The following year, Sir William Lawrence Bragg and his father, Sir William Henry Bragg, recorded the diffraction pattern of sodium chloride from a monochromatic beam of X-rays and used it to describe the molecular structure of a crystal for the first time. These breakthroughs earned von Laue a Nobel prize in 1914, and the Braggs a Nobel prize in 1915.

1.1 Diffraction Theory

The Braggs developed a convenient description of the geometry required for a diffracted X-ray beam to interfere constructively and therefore potentially be observed. They imagined each diffracted beam as a reflection from a set of parallel planes separated by a spacing, d_{hkl}, within the crystal. Each plane is described by three integers known as Miller indices, h, k and l, which describe the plane with respect to the three unit cell edges, a, b and c.

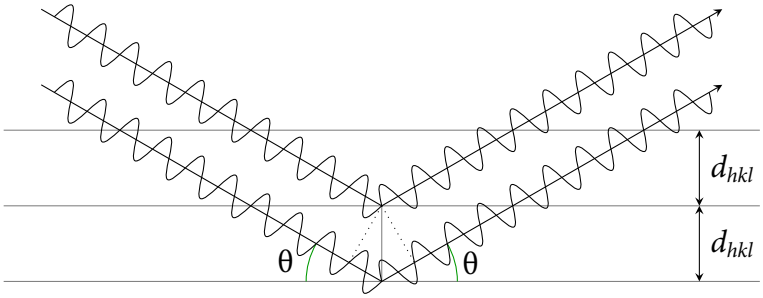

Figure 1.1: A representation of the geometry which is used as the basis of Bragg's Law.

In order for X-ray beams scattered from adjacent planes in a crystal to interfere constructively, the path length difference between them must be an integer multiple of the wavelength of the beam, as shown in Figure 1.1. The difference in path length is a function of the plane spacing and the angle at which the incoming beam hits the plane, θ. The conditions under which a diffracted beam with wavelength λ is observed from a plane with spacing d_{hkl} is described by Bragg's Law:

$$n\lambda = 2d_{hkl}\sin\theta \tag{1.1}$$

A full diffraction pattern for a crystal is obtained by rotating the crystal such that this law is satisfied for a large number of the possible Miller planes. As there are an infinite number of these planes, data are collected to a specified resolution limit, usually a minimum of d_{hkl} = 0.8 Å for small molecular crystals. A description of the rotations required to observe a particular reflection is given in Section 1.1.4.

A diffraction pattern provides two different types of information. The size and shape of the lattice, and hence of the unit cell, is provided by the spatial distribution of the diffracted X-rays, while the intensities of these beams are related to the electron density within the unit cell.

1.1.1 The Reciprocal Lattice

It is often convenient to describe the diffraction pattern by a set of vectors in an imaginary construct known as reciprocal space. Each vector has a direction defined by the normal to the *hkl* planes which gave rise to the reflection, and a magnitude of $\frac{1}{d_{hkl}}$. The end points of all these vectors, each representing one reflection in the diffraction pattern, produce a lattice, known as the reciprocal lattice.

A further construct, the Ewald sphere, provides a particularly useful description of the geometry of a crystal reflection. Developed by P. P. Ewald (1913), this exists only in reciprocal space, but it does correspond to the physical processes involved in a diffraction

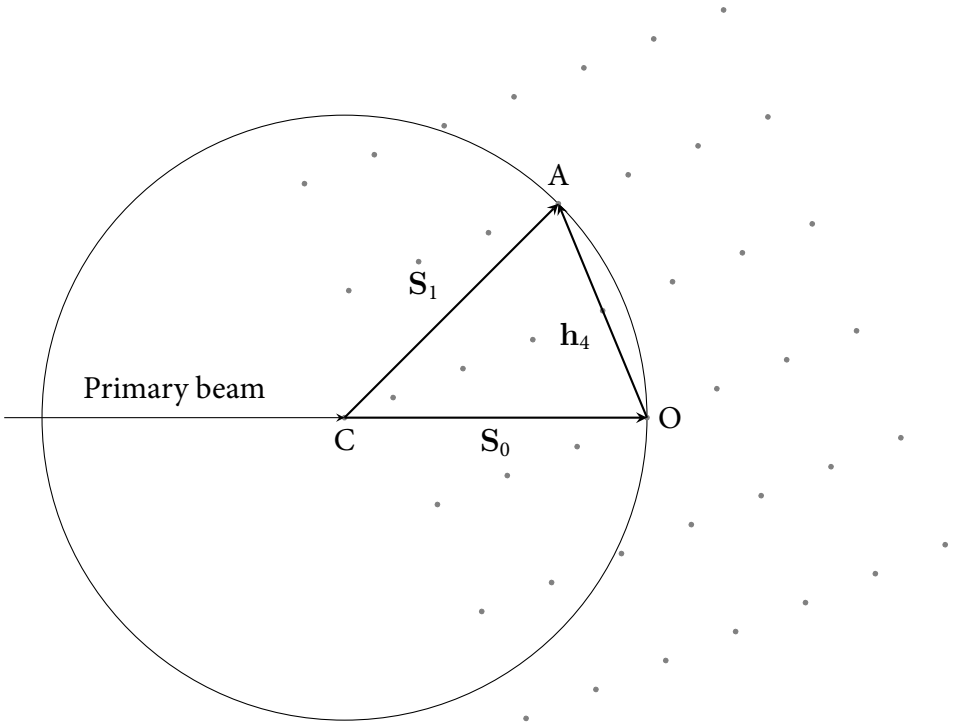

Figure 1.2: Ewald sphere construction, with the crystal position at C, the origin of the reciprocal lattice at O, and a reciprocal lattice point in the reflecting position at A. Reciprocal lattice nodes are shown as grey circles.

experiment. A sphere of radius $\frac{1}{\lambda}$ is drawn around the crystal position, as shown in Figure 1.2. The reciprocal lattice is then drawn with the origin of the lattice at the edge of the sphere, at the position where the primary X-ray beam exits the sphere. The reciprocal lattice rotates as the crystal is rotated, and Bragg's Law is satisfied for a reflection when its reciprocal lattice point passes through the boundary of the sphere.

The direction in which a beam is diffracted is given by the vector from the crystal position (C) to the reciprocal lattice point on the sphere (A). This vector is described in the sections below as $\mathbf{S}_1$. The vector from the crystal position to the origin of the reciprocal lattice is known as $\mathbf{S}_0$, and the vector from the lattice origin (O) to the lattice point at A is known as $\mathbf{h}_4$. From the definition of the reciprocal lattice, the direction of the $\mathbf{h}_4$ vector is normal to the Miller plane giving rise to the diffraction.

1.1.2 Structure Factors

The diffraction intensity of a given reflection is related to the electron density within the crystal by a Fourier transform, given for a particular reflection with Miller indices *h*, *k* and *l* by the structure factor equation:

$$F_{hkl} = \sum_{n=1}^{N} f_n \cos 2\pi(hx_n + ky_n + lz_n) + i \sum_{n=1}^{N} f_n \sin 2\pi(hx_n + ky_n + lz_n) \tag{1.2}$$

where there are N atoms in the unit cell, each with atomic position x_n, y_n and z_n and with an atomic scattering factor of f_n. The quantity F_{hkl} is the structure factor. Each reflection has an amplitude and a phase, of which only the amplitude (also known as the intensity of a reflection) is observed experimentally. This observed intensity is proportional to the square of the structure factor: $I_{hkl} \propto F_{hkl}^2$.

1.1.3 Symmetry

The unit cell is a section of the crystal which is repeated by translations in all directions to give the whole crystal. For primitive cells this is the smallest section which may be so defined, while for centred cells a larger volume is chosen. The contents of the unit cell may also be related to each other by other symmetry operations such as rotations, screw axes and glide planes. The smallest part of the unit cell which can generate the whole cell by the use of these symmetry operations is known as the asymmetric unit. A complete set of symmetry operations, including translational symmetry for centred cells defines a space group, and there are 230 possible sets. A complete list of all these space groups and their symmetry operations is tabulated in the International Tables for Crystallography, Volume A (Hahn, 2005).

Many of these space groups can be calculated from the intensity variations present in the diffraction pattern of the crystal. For instance, some symmetry operations give rise to systematic absences, in which certain reflections have an intensity of 0. As an example, in an I-centred unit cell, an atom at position (x, y, z) has a symmetry equivalent at $(x + \frac{1}{2}, y + \frac{1}{2}, z + \frac{1}{2})$. This means that Equation 1.2, the structure factor equation, can be rewritten as follows:

$$\begin{aligned} F_{hkl} = &\sum_{n=1}^{N/2} f_n \left[\cos 2\pi \left(hx_n + ky_n + lz_n\right) + \cos 2\pi \left(hx_n + ky_n + lz_n + \tfrac{h}{2} + \tfrac{k}{2} + \tfrac{l}{2}\right)\right] \\ &+ i \sum_{n=1}^{N/2} f_n \left[\sin 2\pi \left(hx_n + ky_n + lz_n\right) + \sin 2\pi \left(hx_n + ky_n + lz_n + \tfrac{h}{2} + \tfrac{k}{2} + \tfrac{l}{2}\right)\right] \end{aligned} \tag{1.3}$$

This can be rewritten by defining $a = hx_n + ky_n + lz_n$, and using the sine and cosine addition formulae:

$$F_{hkl} = \sum_{n=1}^{N/2} f_n \left[\cos 2\pi a + \cos 2\pi a \cos \pi(h+k+l) - \sin 2\pi a \sin \pi(h+k+l)\right] + i \sum_{n=1}^{N/2} f_n \left[\sin 2\pi a + \sin 2\pi a \cos \pi(h+k+l) + \cos 2\pi a \sin \pi(h+k+l)\right] \tag{1.4}$$

For any integer value of n, $\sin n\pi$ has a value of 0. Since h, k and l are all integers, this means that the equation may be simplified as follows:

$$F_{hkl} = \sum_{n=1}^{N/2} f_n \left[\cos 2\pi a + \cos 2\pi a \cos \pi(h+k+l)\right] + i \sum_{n=1}^{N/2} f_n \left[\sin 2\pi a + \sin 2\pi a \cos \pi(h+k+l)\right] \tag{1.5}$$

By the same reasoning, $\cos n\pi$ has two possible values if n is an integer: 1 if n is even, and -1 if n is odd. Therefore, if $h + k + l$ is odd, the expressions containing $\cos 2\pi a$ and $\sin 2\pi a$ both cancel out, and F_{hkl} will have a value of 0. As the reflection intensity is proportional to F_{hkl}^2, it also becomes 0, and the reflection is absent from the diffraction pattern.

1.1.4 Diffraction Geometry

In order to measure a diffraction pattern to a particular resolution, the crystal must be rotated within the X-ray beam so that the Bragg equation is satisfied for all the Miller planes up to the specified resolution. This is achieved with a goniometer, which usually has several dependent rotation axes, allowing the crystal to be rotated to any desired position.

Commercially available instruments tend to use one of two geometries, both of which offer four rotation angles. The crystal is mounted on the φ axis, which rotates around the z axis when all other angles are at 0°. This is mounted on the χ axis for Eulerian geometries, or on the κ arm for kappa geometries. In turn, these are mounted on the ω axis. The fourth rotation angle is 2θ, which allows for positioning the detector. The geometry of a Eulerian cradle is shown in a diagram in Figure 1.3.

In both these cases, φ and ω rotate around the z axis when all other angles are set to 0°. The χ circle rotates around the y axis when ω is at 0°. In 'three-circle' Eulerian goniometers, the χ angle is fixed at a value between 0° and 90°. The κ angle is more complicated, as the φ axis is not mounted directly on the κ rotation angle, but at a fixed angle from that rotation axis.

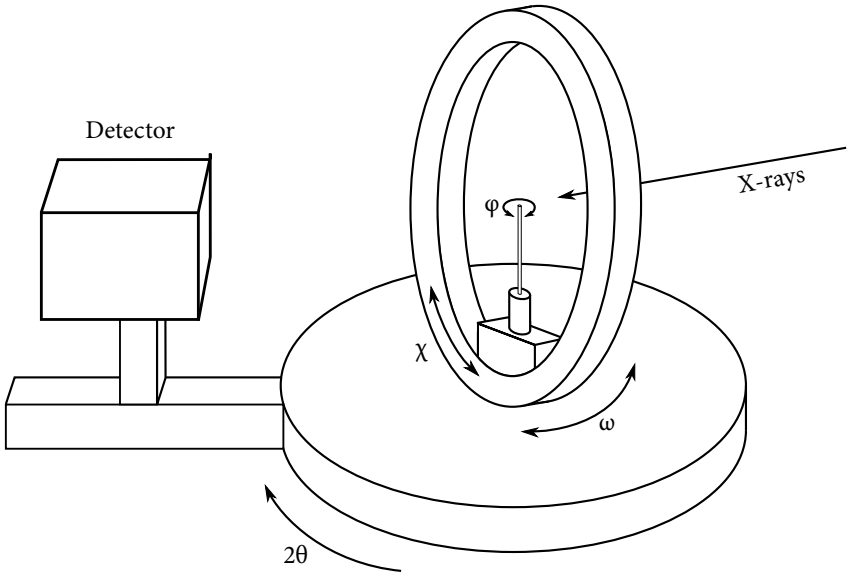

Figure 1.3: A diagram to show the geometry of a Eulerian cradle.

The most compact way to represent these rotations mathematically is to use matrix algebra. Each circle may be represented by one or more rotation matrices. The resulting crystal rotation may then be described by a combination of these matrices.

To specify these matrices, a consistent coordinate system should be used. The system used in this work is the same as that used by Busing & Levy (1967). The z axis points directly upwards, the y axis is parallel to the primary beam and the x axis is perpendicular to both, forming a right-handed set. Instrument manufacturer Bruker AXS (hereafter Bruker) use the same right-handed coordinate system, but rotated by 90° about z so that x is parallel to the primary beam. Both conventions are shown in Figure 1.4.

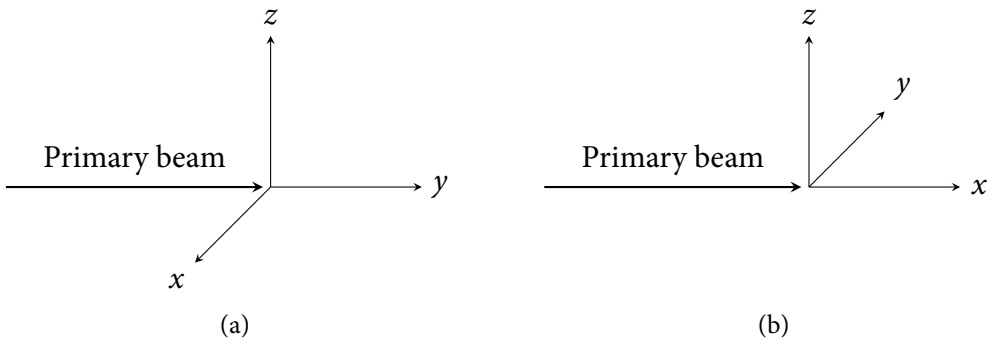

Figure 1.4: The coordinate system used by (a) Busing & Levy, and (b) Bruker.

1.1.4.1 Detector Calculations

The $\mathbf{h}_4$ vector from the Ewald sphere (Figure 1.2) may be calculated from a position (P) on a position-sensitive area detector if various details are known about the detector. These are: the pixel size in mm (S); the position of the primary X-ray beam when the detector 2θ angle is 0° (C); the distance of the detector from the crystal (d); and the detector 2θ angle. The detector 2θ angle is converted to a rotation matrix about the z axis, represented by $\mathbf{R}_{2\theta}$. When these are known, the $\mathbf{S}_1$ vector can be calculated as follows:

$$\mathbf{S}_1 = \mathbf{R}_{2\theta}(n_x, d, n_z) \tag{1.6}$$

where

$$n_x = S_x(P_x - C_x)$$

$$n_z = S_y(P_y - C_y)$$

This vector should be normalised and then multiplied by $\frac{1}{\lambda}$ after calculation to bring it onto the same scale as the Ewald sphere construction. All pixel positions are transformed before use so that they are relative to the bottom-left corner of the detector. The x ordinate is then parallel to the laboratory x axis, and the y ordinate is parallel to the laboratory z axis before the detector angle (and any corrections which may be applied) are taken into account.

Corrections may be required if the face of the detector is not perfectly aligned so it is perpendicular to to the 2θ arm of the goniometer. The misalignment can be described by three angles: the pitch, roll, and yaw, which rotate around the x, y and z axes respectively (in the Busing & Levy conventions). Assuming that the corrections are applied in that order, describe rotations about the face of the detector, and that they are described by matrices labelled $\mathbf{R}_{\text{pitch}}$, $\mathbf{R}_{\text{roll}}$ and $\mathbf{R}_{\text{yaw}}$, the $\mathbf{S}_1$ vector calculation in Equation 1.6 may be modified as follows:

$$\mathbf{S}_1 = \mathbf{R}_{2\theta}\left[(0, d, 0) + \mathbf{R}_{\text{yaw}}\mathbf{R}_{\text{roll}}\mathbf{R}_{\text{pitch}}(n_x, 0, n_z)\right] \tag{1.7}$$

1.1.4.2 Goniometer Calculations

Once the $\mathbf{S}_1$ vector has been calculated from a pixel position on the detector, the *hkl* index may be calculated if the goniometer angles and the unit cell of the crystal are known. The $\mathbf{S}_1$ vector is first converted to the scattering vector, $\mathbf{h}_4 = \mathbf{S}_1 - \mathbf{S}_0$.

To convert this scattering vector to an *hkl* vector, it must be rotated by the inverse of the

goniometer angles, and then by the inverse of the **UB** matrix. The **UB** matrix relates the unit cell axes to the laboratory axes of the diffractometer, and is described in Busing & Levy (1967). It is generally provided by the manufacturers' software, *e.g. Apex2*, when the unit cell is calculated from the diffraction pattern. The result of the calculation should have integral components if the **UB** matrix is correct and the pixel position describes a crystal reflection.

$$\mathbf{hkl} = \mathbf{UB}^{-1}\,\mathbf{\Phi}^{-1}\,\mathbf{X}^{-1}\,\mathbf{\Omega}^{-1}\,\mathbf{h}_4 \tag{1.8}$$

The reverse of this equation can be used to calculate $\mathbf{h}_4$ from an *hkl* vector:

$$\mathbf{h}_4 = \mathbf{\Omega}\,\mathbf{X}\,\mathbf{\Phi}\,\mathbf{UB}\,\mathbf{hkl} \tag{1.9}$$

Intermediate vectors are also specified, *i.e.* $\mathbf{h}_4 = \mathbf{\Omega h}_3$, $\mathbf{h}_3 = \mathbf{X h}_2$, $\mathbf{h}_2 = \mathbf{\Phi h}_1$.

1.1.4.3 Calculating Goniometer Angles for a Reflection

The Bragg equation is satisfied for a reflection when the scattering angle $\mathbf{S}_1$ has length $\frac{1}{\lambda}$, and therefore satisfies the following equation:

$$|\mathbf{S}_1| = |\mathbf{S}_0 + \mathbf{h}_4| = \frac{1}{\lambda} \tag{1.10}$$

Omega: A commonly used mode of data collection for four-circle diffractometers is the ω scan, in which χ and φ are fixed, and ω is varied through a range of angles. In order to calculate at which values of ω the reflections will be visible, the following equations are used (McIntyre, 2009).

Since $\mathbf{h}_4 = \mathbf{\Omega h}_3$, Equation 1.10 expands to the following equation:

$$\frac{1}{\lambda} = |\mathbf{S}_0 + \mathbf{\Omega h}_3| = \left| \begin{pmatrix} 0 \\ \frac{1}{\lambda} \\ 0 \end{pmatrix} + \begin{pmatrix} \mathbf{h}_{31}\cos\omega + \mathbf{h}_{32}\sin\omega \\ -\mathbf{h}_{31}\sin\omega + \mathbf{h}_{32}\cos\omega \\ \mathbf{h}_{33} \end{pmatrix} \right| \tag{1.11}$$

Evaluating this gives:

$$\frac{1}{\lambda^2} = \left(\mathbf{h}_{31}\cos\omega + \mathbf{h}_{32}\sin\omega\right)^2 + \left(\frac{1}{\lambda} - \mathbf{h}_{31}\sin\omega + \mathbf{h}_{32}\cos\omega\right)^2 + \mathbf{h}_{33}^2 \tag{1.12}$$

which can be rearranged to give:

$$\lambda(\mathbf{h}_{31}^2 + \mathbf{h}_{32}^2 + \mathbf{h}_{33}^2) = 2\mathbf{h}_{31}\sin\omega - 2\mathbf{h}_{32}\cos\omega \tag{1.13}$$

Two sine waves with the same frequency but different phase shifts, such as $\sin\omega$ and $\cos\omega$ in Equation 1.13, can be combined to give another sine wave with the same frequency, but a different phase shift, according to the equation below.

$$x\sin\alpha + y\cos\alpha = \sqrt{x^2 + y^2} \cdot \sin\left[\alpha + \arctan\left(\frac{y}{x}\right)\right] \tag{1.14}$$

Using this equation, Equation 1.13 can be rewritten as,

$$\lambda(\mathbf{h}_{31}^2 + \mathbf{h}_{32}^2 + \mathbf{h}_{33}^2) = 2\sqrt{\mathbf{h}_{31}^2 + \mathbf{h}_{32}^2} \cdot \sin\left[\omega + \arctan\left(\frac{-\mathbf{h}_{32}}{\mathbf{h}_{31}}\right)\right] \tag{1.15}$$

which can be rearranged to solve for ω, to give the following equation (1.16). There are two solutions for ω, which correspond to the two angles at which the reciprocal lattice point will pass through the boundary of the Ewald sphere.

$$\omega = \arcsin\left(\frac{\lambda(\mathbf{h}_{31}^2 + \mathbf{h}_{32}^2 + \mathbf{h}_{33}^2)}{2\sqrt{\mathbf{h}_{31}^2 + \mathbf{h}_{32}^2}}\right) - \arctan\left(\frac{-\mathbf{h}_{32}}{\mathbf{h}_{31}}\right) \tag{1.16}$$

Phi: Another common mode of data collection is the φ scan, in which χ and ω are fixed, and φ is varied through a range of angles. The same process as that used by McIntyre (2009) for $\mathbf{\Omega}$ can be followed for calculating the φ angles at which a reflection is visible as can be used for ω above. Here, $\mathbf{h}_4 = \mathbf{\Omega X \Phi h}_1$, hence Equation 1.10 expands to the following:

$$\frac{1}{\lambda} = |\mathbf{S}_0 + \mathbf{\Omega X \Phi h}_1| \tag{1.17}$$

This leads to a considerably more complicated equation due to the presence of terms for χ and ω:

$$\begin{aligned}\frac{\lambda}{2}(\mathbf{h}_{11}^2 + \mathbf{h}_{12}^2 + \mathbf{h}_{13}^2) + \mathbf{h}_{13}\sin\chi\sin\omega = \\ -\cos\omega(\mathbf{h}_{12}\cos\varphi - \mathbf{h}_{11}\sin\varphi) + \cos\chi\sin\omega(\mathbf{h}_{11}\cos\varphi + \mathbf{h}_{12}\sin\varphi)\end{aligned} \tag{1.18}$$

In analogy to the equations for ω scans, this is rearranged to give,

$$\frac{\lambda}{2}(\mathbf{h}_{11}^2 + \mathbf{h}_{12}^2 + \mathbf{h}_{13}^2) + \mathbf{h}_{13}\sin\chi\sin\omega = (\mathbf{h}_{12}\cos\chi\sin\omega + \mathbf{h}_{11}\cos\omega)\sin\varphi + (\mathbf{h}_{11}\cos\chi\sin\omega - \mathbf{h}_{12}\cos\omega)\cos\varphi \tag{1.19}$$

and hence,

$$\varphi = \arcsin\left(\frac{\frac{\lambda}{2}(\mathbf{h}_{11}^2 + \mathbf{h}_{12}^2 + \mathbf{h}_{13}^2) + \mathbf{h}_{13}\sin\chi\sin\omega}{\sqrt{a^2 + b^2}}\right) - \arctan\left(\frac{b}{a}\right) \tag{1.20}$$

where

$$a = \mathbf{h}_{12}\cos\chi\sin\omega + \mathbf{h}_{11}\cos\omega$$

$$b = \mathbf{h}_{11}\cos\chi\sin\omega - \mathbf{h}_{12}\cos\omega$$

As in the case for calculating ω, there are two possible results for φ, for the two angles at which the reciprocal lattice point passes through the boundary of the Ewald sphere.

1.2 Low Temperature Crystallography

One of the most important uses of crystal structure analysis is to probe the relationship between the structural features of a material and its physical properties. These structural features may be affected by changes in external environment, or by the chemical environment within the crystal, where solvents of counter-ions may be exchanged for alternatives. The results of these investigations may lead to new materials with enhanced physical or chemical properties due to the increased understanding of the underlying phenomena.

By far the most common environmental variable which can be controlled in a single-crystal diffraction experiment is the sample temperature. Open-flow nitrogen cryostats are very widely used, allowing control of sample temperatures from $\sim$ 80 K to $>$ 450 K. Systems which allow crystals to be cooled below this temperature are rarer, but may provide valuable information. Techniques for cooling samples and their applications are described below.

1.2.1 Sample Cooling Methods

Single crystal X-ray diffraction data have been measured below room temperature for at least 75 years; for example, in 1936 the crystal structures of bromine (Vonnegut & Warren, 1936) and chlorine (Keesom & Taconis, 1936) were reported at −150˚C and −185˚C respectively. The bromine crystal was cooled with a container of liquid air, which was exhausted over the sample. Without pumps or heating elements, there was no control over the flow rate or temperature of the air, and the reported temperature is described as 'approximate'.

Later devices used a cooled stream of gas which had been passed through a Dewar of refrigerant in a copper coil. In order to prevent ice formation, a second stream of dry gas at room temperature was used to form a cylinder around the stream of cold gas. The temperature, measured by a thermocouple on the sample holder, could be adjusted by altering the flow rate of the cold gas or by introducing some of the room temperature gas into the cold gas stream. With this system, the crystal temperature could be maintained within a range of 5˚C, down to liquid air temperatures (Post *et al.*, 1951).

1.2.1.1 Nitrogen Based Cryostats

The most commonly used gas at this point was nitrogen, although experiments were made with alternatives. One system is described which could be used with both nitrogen and hydrogen, allowing temperatures of 25 K to be reached (Robertson, 1960). Various problems were reported when using hydrogen as a coolant, not least the necessity of removing the exhaust hydrogen during the experiment to prevent the risk of explosion!

An important milestone was reached when a method for automatically controlling the temperature of a gas-stream cryostat was published by Young (1966). A skein of wires in the gas exit tube acted as a resistance heater, allowing the temperature to be regulated with standard furnace controllers of the time. A furnace was also fitted, allowing temperatures between 90 K and 975 K to be accessed, with a stability of ±0.1˚C in the best case at low temperatures, and a stability of ±2˚ at 600˚C.

The next major innovation came with the invention of the Cryostream system (Cosier & Glazer, 1986). Nitrogen gas cooling systems up to this point used pressurised dewars in which liquid nitrogen was boiled, before escaping at a certain flow rate through a heater and onto the sample (Rudman & Godel, 1969). This led to heat leaks in the insulated tube and in the low temperature valves controlling the flow rate, as well as large instabilities in gas flow and temperature when the dewar was refilled.

The Cryostream solved these problems by introducing a pump, operating close to room temperature. The liquid nitrogen is passed through a small evaporator coil, and the cold vapour then travels through a heat exchanger, warming it to near room temperature. It then flows through a pump, before passing back through the heat exchanger, cooling back down to close to its boiling point. A heater then controls the final gas temperature when it reaches the sample. This system reduces the opportunity for heat leaks, and allows for a constant flow rate even when the supply dewar is refilled, and the quoted temperature range was 77.4–323.0 K with a precision of ±0.1 K.

This system proved highly successful, and this design (now sold by Oxford Cryosystems) is one of the most popular cooling systems used in SXRD experiments. This and other similar systems enable the sample to be mounted easily on a diffractometer, often within an oil drop which is flash frozen on entering the gas stream. The ability to see the sample also allows the sample environment to be changed by irradiating the crystal with light, in addition to offering more control over the *in situ* crystallisation of liquids and gases (Goeta & Howard, 2004).

1.2.1.2 Helium Based Cryostats

Devices for cooling crystals to below liquid nitrogen temperatures using helium have existed for at least 50 years. Many designs from before the 1980s used liquid helium with reservoirs near the sample position (see *e.g.* Streib & Lipscomb, 1962; Woodley *et al.*, 1971; Thomas, 1972; Hohlwein & Wright, 1981). Other systems were designed without this reservoir which allowed for a greater range of crystal movements, although these systems still required a supply of liquid helium (Coppens *et al.*, 1974; Albertsson *et al.*, 1979). One rather extreme alternative (Chieh *et al.*, 1977) involved immersing an entire camera system in liquid helium along with the crystal, although unfortunately the crystal which was used to test the system became detached from the mount before data could be measured.

Liquid helium coolers such as those described above have several drawbacks. One of the greatest of these is the amount of liquid helium required, which can incur considerable expense over the duration of a data collection, if it is even possible to obtain in the first place. This can be mitigated to a certain extent by recovering the exhaust helium, but this is not always possible in practice. Another disadvantage stems from handling the liquid helium to the point at which it can cool the crystal, which can restrict the movement of the cryostat considerably due to the stiff vacuum-jacketed lines required (Larsen, 1995).

More recently, closed-cycle helium coolers have appeared, which offer many advantages over liquid helium coolers (Woodard & Straumanis, 1971; Samson *et al.*, 1980; Henriksen

et al., 1986; Zobel *et al.*, 1992). In these systems, helium is pressurised with a compressor, before being delivered to the expander through flexible gas lines. This high pressure helium passes through regenerators, which were cooled during the previous cycle, before undergoing adiabatic expansion at the heat stations, which are thereby cooled. The expanded gas then passes back through the regenerators, cooling them, before entering the compressor again and starting the cycle anew (Larsen, 1995). These systems generally allow cooling samples to around 10 K.

Closed-cycle refrigerators (CCRs) recirculate all the gas used for sample cooling, so their operational costs are very low as far as helium is concerned. Helium gas is also much simpler to transport than liquid helium, making the connecting lines used within the system much simpler as well. Finally, with no reservoir of liquid, the cooler may be operated in a wide range of orientations, allowing more crystal positions within the beam, and increasing the range of reflection data which may be collected.

Two such systems have been developed in Durham, first the *Fddd* diffractometer (Copley *et al.*, 1997), with a rotating anode source and a point detector, allowing temperatures of 10 K to be accessed. Recently a new system has been developed: the Xiphos (Probert *et al.*, 2010), featuring a two-stage CCR with an additional open cycle Joule-Thomson third stage giving a base temperature of 2.0 K, which is a significant reduction in temperature from most diffractometers which use CCRs. This system is described in Chapter 2.

The main disadvantage of these systems is that the sample must be kept under vacuum to prevent ice formation. The vacuum shrouds which are therefore required are often made from beryllium, which obscure the crystal from view, and make centring difficult. Alternatives to beryllium such as Kapton® which allow the crystal to be seen have been used in a system described by Meserschmidt *et al.* (2003), although due to differences in cryostat design this approach has not met the same success with the Xiphos (see Chapter 2).

The experimental difficulties caused by obscuring crystals from view in a diffraction experiment have led to the development of systems which use a stream of cold helium gas to cool the sample. This has many of the advantages of the nitrogen based gas streams, in which the crystal may be seen at all times, but allows data to be collected at lower temperatures. One such example is the N-HeliX, manufactured by Oxford Cryosystems, which uses a CCR internally to cool the helium, before the gas escapes on to the sample. With this system, data can be collected at temperatures as low as 30 K, at a cost of approximately one helium cylinder per day (Goeta & Howard, 2004).

1.2.2 Applications

1.2.2.1 Routine Use of Low Temperature

One of the main effects of lowering the temperature of a crystal is that the vibrations of the crystal lattice are reduced. This has a number of consequences, which help to explain why SXRD is now commonly performed at low temperatures. One of the simplest is that with open-flow gas cryostats, samples may be mounted in an inert oil which vitrifies in the low temperature to hold the crystal in place during the experiment. This allows samples to be mounted rapidly, and allows sample mounts to be reused when an experiment has finished.

Another consequence concerns the resolution of the observed data. Increasing thermal motion will increase the volume occupied by the electrons of an atom, and it is the electrons that scatter X-rays. The X-ray wavelength is of the same order of magnitude as the dimensions of this volume, and so there is an appreciable path difference between X-rays scattered from different electrons within the same area.

At higher 2θ angles, this path difference increases, and hence the destructive interference will also increase, decreasing the observed reflection intensity. By reducing the atomic motion, the difference in path length will decrease, and hence reflection intensities will become greater at larger 2θ angles. This increases the resolution to which reflection intensities can be measured at lower temperatures.

The length of time required to measure experimental reflection intensities is orders of magnitude larger than the period of atomic motion, and hence the atomic displacements extracted from an experiment are averaged over time, as well as space. At higher temperatures (*e.g.* room temperature), this can give rise to dynamic disorder, in which many orientations of a molecule may be separated by only very small energy barriers. Examples of this include spherical anions such as BF_4^-, PF_6^-, and many others.

Dynamic disorder can be difficult to distinguish from static disorder, in which atoms may be in different places in different unit cells. By lowering the temperature and reducing the thermal motion of atoms, the dynamic disorder is reduced, but the static disorder will not be affected. Not only does this allow distinguishing between the forms of disorder, but also makes atoms affected by dynamic disorder easier to model in the final structural model.

1.2.2.2 Study of Liquids and Gases

The most obvious class of materials for which it is a requirement to measure diffraction data at low temperatures are those which are liquids or gases at room temperature. Early examples of this are the crystal structures of chlorine and bromine, both published in 1936 (Keesom & Taconis, 1936; Vonnegut & Warren, 1936). This area of research is still very active, with investigations into pure molecular structures such as chloroform (Yufit & Howard, 2010), studies into polymorphism (*e.g.* Choudhury *et al.*, 2004), and co-crystals of two or more compounds (*e.g.* Kirchner *et al.*, 2008), among other examples.

1.2.2.3 Studying Changes in Material Properties

An important use of crystallography is to probe the relationship between the structure of a material in the solid state and its properties. It is therefore highly desirable to be able to determine the molecular structure and crystal packing of materials above and below a phase transition, in order to aid in the understanding of the underlying physical processes.

Spin crossover complexes (described further in Chapter 5) are one class of materials that are commonly studied with crystallographic techniques at a range of temperatures. These are materials with several possible electronic states, which it is possible to switch between with changes in temperature and other ambient conditions (Gütlich *et al.*, 2000).

Many of the transitions in such materials occur at temperatures above the boiling point of nitrogen, so can be studied with nitrogen gas-stream cryostats. There is a related phenomena, however, in which at much lower temperatures ($\sim$ 50 K and below) the material may be excited by laser light into a meta-stable state in which it remains trapped. These states have also been studied with SXRD, using helium gas-stream cryostats (*e.g.* Money *et al.*, 2003), and also with helium CCRs (*e.g.* Kusz *et al.*, 2005).

Another class of materials which undergo changes in physical properties at low temperature are single molecule magnets, described in Chapter 6. At low temperatures these materials undergo a change in their magnetic state, and although the magnetism is a property of individual molecules, the intermolecular contacts in the solid state have an effect on the transition temperature (Aromí *et al.*, 1998; Gatteschi & Sessoli, 2003). The transition temperatures reported so far are very low, below 10 K, and understanding the solid state structure is very important to be able to create materials with higher transition temperatures. No structures of these materials below the transition temperature are known to the author, and one of the lowest temperature structures has been measured with neutron radiation at 20 K (Langan *et al.*, 2001). The lack of structures demonstrates the huge value

of an ultra-low temperature X-ray diffractometer such as the Xiphos.

1.2.3 Conclusions

Low temperature SXRD is highly useful for studying the solid-state structures of materials in order to probe the relationship between this structure and the physical properties displayed. Experiments at temperatures of 80 K and above are now common, using cold nitrogen gas streams. The ability to lower the temperature further is also very important, but is considerably more rare. Various approaches have been taken, most of which use helium gas, either as a gas stream to cool the sample, or in closed-cycle refrigerators. Few of these devices are installed in university laboratories, and the lowest temperatures, those approaching 2 K and below, are generally confined to neutron diffraction centres, highlighting the need for a new X-ray instrument, such as the Xiphos.

Chapter 2

The XIPHOS Diffractometer

There are a huge range of materials which display interesting and potentially valuable physical properties at very low temperatures such as organic superconductors, single molecule magnets and systems with spin transitions. Studying these materials below their transition temperatures could provide insights into the origins of these properties, potentially enabling the synthesis of materials displaying the behaviours at much higher temperatures (Larsen, 1995; Goeta & Howard, 2004).

These low temperatures are impossible to reach for most diffractometers and those that have this capability are often installed in central facilities, many of which offer neutron diffraction experiments only. While these are highly useful for many purposes, the neutron flux available is much lower than that available with X-rays, even with sealed tube and rotating anode sources, and so experiments are relatively slow and much larger crystals are often required. In addition to this, it may take many months between submitting a proposal to use such an instrument and actually performing the experiment.

To provide routine access to structural data at ultra low temperatures in a university laboratory, a unique diffractometer has been designed. The XIPHOS[1] (**X**-ray **i**nterface for **p**hoto-induced, **h**igh pressure, and l**o**w temperature **s**tructural studies) is a custom designed single-crystal X-ray diffractometer, featuring a Displex® cryosystem with an additional third stage which allows structural data to be collected with samples cooled to temperatures as low as 2.0 K (Probert *et al.*, 2010). The design and operation of this diffractometer is described below.

[1]From the Greek, ξίφος: a double-edged, single handed sword used in ancient Greece.

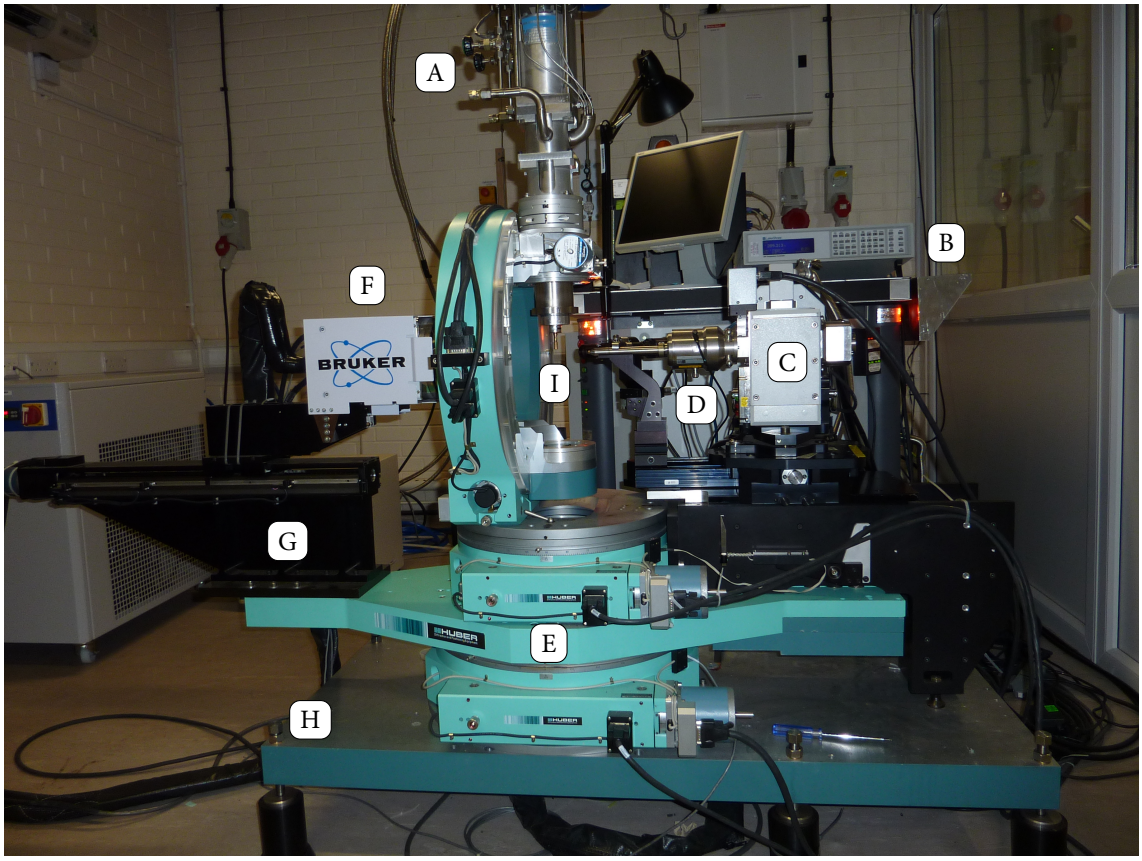

Figure 2.1: The XIPHOS diffractometer, with labels describing major components: [A] Displex, [B] LakeShore 340 temperature controller, [C] TXS X-ray source, [D] Helios mirrors, [E] Huber goniometer, [F] *APEX2* detector, [G] motorised detector track, [H] aluminium plate, with the vibration dampening mounts below, [I] sample position.

2.1 System Components

The closed-cycle cryostat used for sample cooling on the XIPHOS diffractometer is an APD DE-202E Displex [A in Figure 2.1], which has been modified by AS Scientific Products Ltd to add an additional third Joule-Thompson stage, allowing temperatures of 2.0 K to be reached. The modification requires a high pressure helium line running at 7 bar, and a vacuum pumped exhaust line to provide the additional cooling. The temperature is monitored and controlled by a LakeShore 340 controller [B], utilising a LakeShore DT-470-CO-13 diode.

The X-ray source is a TXS direct-drive molybdenum rotating-anode generator from Bruker AXS [C], with Helios multilayer optics [D] giving an optimum beam size of 120 µm at the sample position (FWHM). These optics use two perpendicular mirrors mounted side-by-side, of the design proposed by Montel (1957). The mirrors consist of many layers of material, and the spacing of these layers is designed so that Bragg's law is satisfied for only

a small range of desired wavelengths, which are reflected from both mirrors and focussed to a single point at a fixed distance from the mirrors. This produces an intense, highly monochromatic X-ray beam at the sample position.

The generator head and optics are mounted on a support with five degrees of freedom, allowing the beam origin to be moved independently of the goniometer for alignment purposes. This enables much easier machine alignment than systems with a fixed beam origin, in which the goniometer must be moved instead (*e.g.* Copley *et al.*, 1997).

The goniometer is a 512.1 four-circle design manufactured by Huber Diffraktiontechnik, with an offset χ cradle [E]. As the Displex has a mass of more than 15 kg, large and robust circles were needed to ensure that the weight of the Displex could be supported and accurately positioned throughout the full range of movements required during a single crystal diffraction experiment.

A Bruker APEXII CCD area detector [F] is mounted on a long motorised track [G], allowing movement of up to 500 mm from the sample position. The detector can therefore be moved sufficiently far to avoid the goniometer circles if ω is rotated so as to collect data in the 'non-bisecting' mode, in which the diffracted X-rays pass to one side of, rather than through, the χ circle before reaching the detector. The motorised track also allows for data to be collected at more than one detector distance during an experiment with no human involvement required during the data collection.

The system uses a Bruker D8 controller to interface with all the positioning drives. This allows the use of unmodified Bruker control software (*D8Tools*, *BIS*, *Apex2*, etc.) which saved considerable time compared to adapting existing software or developing new control software from scratch by avoiding time-consuming coding and debugging.

Finally, the whole system is mounted on a rigid aluminium block [H], supported on six vibration-dampening mounts. This helps to isolate the system not only from external vibrations, but also allows vibrations caused by the pistons in the Displex to affect all parts of the system equally, removing the independent motion of the sample and the X-ray source during experiments.

To allow for full freedom of movement of the Displex and its associated cables, it was decided to sit the goniometer and X-ray source on the floor beside the D8 base, rather than on top of the base as is common with most off-the-shelf single-crystal diffractometers. The Xiphos sits in an enclosed area known as a hutch, which also contains all the equipment required to run the machine, such as the chillers for the TXS and the CCD, the compressor for the first and second stages of the Displex, the LakeShore controller, and the computer used to control the machine. In order to avoid accidental exposure of users to X-rays, the

hutch is sealed when the diffractometer is in operation, and several safety switches are employed to instantly shut off the X-ray generator if the door is opened when the shutters are open.

2.2 Configuring the System

2.2.1 Alignment

The X-ray source is mounted on a stand with five degrees of freedom, allowing the direction and origin of the X-ray beam to be aligned with the crystal position at the centre of the goniometer circles. The primary beam must hit the crystal position along a known vector to allow the diffracted reflections from samples to be interpreted correctly.

An additional degree of freedom enables the generator to be moved closer to or further away from the crystal position. Since the XIPHOS system uses focussing optics with a fixed focal length, this enables the position of the focal point of the X-ray beam to be adjusted. This may be useful in the case of large crystals, for which the beam can be defocussed at the crystal position, in order to illuminate the entire crystal at once.

2.2.1.1 Adjusting the Optics

Helios optics are designed so that the beam used during an X-ray diffraction experiment is reflected twice, once from each of the two mirrors, and is referred to as the 'doubly diffracted' beam. The mirrors can be adjusted using rotations and translations so that they are in the correct position to focus the doubly diffracted beam into a single point. Although the focal length is fixed at the point of manufacture, the mirrors can also be positioned to change the direction of the beam once it is focussed.

The procedure that is followed to focus the principal X-ray beam uses a 'Xyclops' CCD camera with an X-ray sensitive phosphor, supplied by Bruker AXS. This allows the X-ray beam from the mirrors to be visualised on a computer monitor. The mirrors are first adjusted so that the beam splits into four sections, comprising the undiffracted beam, two singly diffracted beams, and the doubly diffracted beam, which is the one used for diffraction experiments.

Once the beam has been split into these four sections, the mirrors are adjusted so that there is a small but clear separation between the sections and the doubly diffracted beam does not move when the Xyclops is rotated. There are several mirror positions for which this

may be possible, one of which also focusses the K_β emission in a very similar position. This is not filtered out in normal operation, and interferes with diffraction experiments. Unfortunately this is not visible with the Xyclops, but it is visible on the CCD detector, so it must be checked before aligning the generator. An example is shown in Figure 2.2.

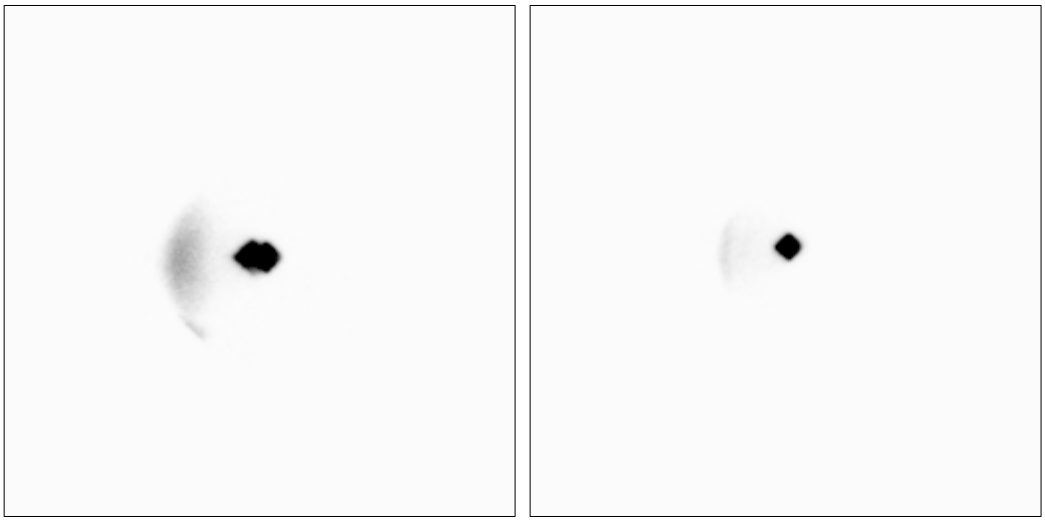

(a) (b)

Figure 2.2: The primary beam seen on the detector during alignment, showing (a) a split beam comprising K_α and K_β radiation, and (b) a single beam showing only K_α. The additional scattering to the left of the beam in both (a) and (b) is a result of air scattering, and would be blocked by the collimator in normal operation.

If K_β is seen, a specific adjustment to the mirrors may be made so that only the K_α radiation is focussed. With the Xyclops again in place, a horizontal translation of the mirrors is used to bring the four sections of the beam back together, and then rotations of the mirrors are used to split the beam again. When moving the beam so that the doubly diffracted beam is in the centre of the Xyclops, care should be taken to keep the separation between the sections of the beam.

Once the final focussing position has been found, a pin-diode may be attached to the collimator to measure the beam intensity, and minor adjustments made to the mirrors to maximise this.

These procedures all require the mirrors to be adjusted while the user is inside the hutch with both the X-ray shutters open, so **extreme care is required to ensure that the operator is not exposed to X-radiation**. Radiation monitors must be worn at all times, and a Geiger counter must be used to check for any radiation leakage between the mirrors and the Xyclops.

2.2.1.2 Generator

Once the alignment of the mirrors is complete, the direction of the primary beam needs to be adjusted to bring the beam through the sample position. This can be achieved using the five adjustment bolts, which move the entire X-ray source, shown in Figure 2.3. The optics described above are attached directly to the source and can therefore be moved freely without affecting the focus of the X-ray beam.

The beam position is determined with the CCD detector, using the *Apex2* software to determine the centroid of the beam. The primary beam is significantly more intense than the sample reflections which are normally measured in a diffraction experiment, and is normally blocked by the beam-stop to avoid overloading the detector. Therefore, when measuring the primary beam position during alignment, two attenuators are used to reduce the intensity of the beam. The first is built into the rotary shutter and is used automatically during experiments when particularly strong sample reflections are measured and is always used during alignment. The second is mounted in place of the beam stop, and is made from brass foil. Even with these attenuators in place, the detector is only exposed to the beam for 1–2 seconds for each measurement.

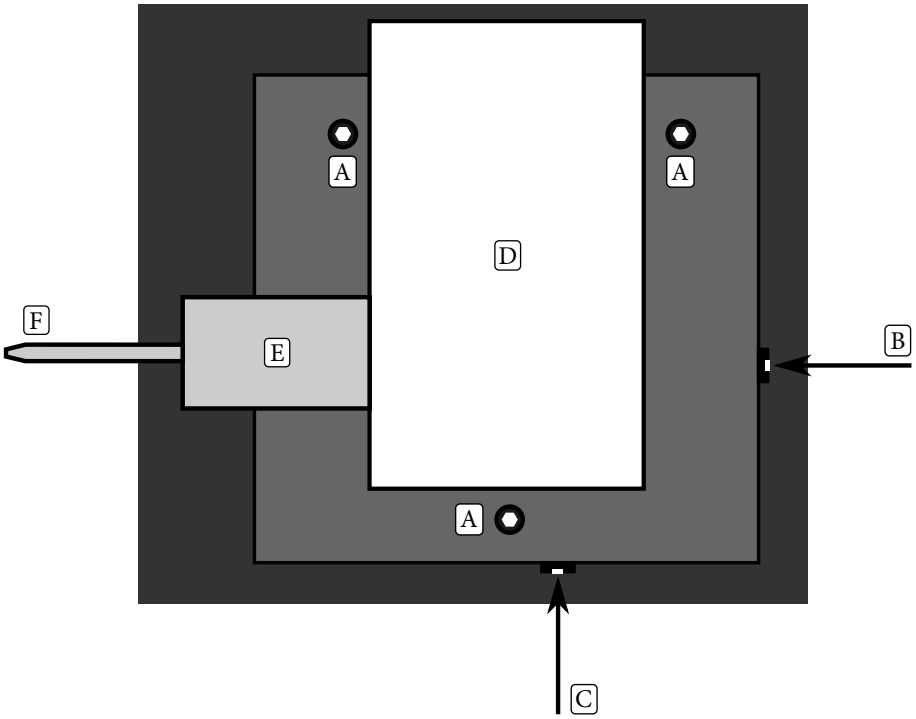

Figure 2.3: A schematic diagram of the X-ray source from above, showing the position of the adjustment bolts: [A] vertical adjustment, [B] yaw adjustment (in plane), [C] horizontal translation (in plane). The source components are: [D] rotating anode housing, [E] mirror housing, [F] collimator.

The five degrees of freedom available to adjust the X-ray source platform are not mutually perpendicular, so several must often be used to achieve a desired effect. For example, there are three bolts [A in Figure 2.3] which are used to adjust the platform vertically. When all three are moved by the same amount in the same direction, the source is translated vertically. However, movement of different amounts or of fewer than three of the bolts will affect the pitch and yaw (rotations around the x and z axes, respectively), as well as the vertical translation of the source. The yaw can also be adjusted by a fourth bolt [B], but the plane of rotation is affected by the three bolts described above. Finally, the fifth bolt [C] adjusts the horizontal translation approximately perpendicularly to the ideal beam vector, but this is also dependent on the pitch and yaw of the platform as affected by the first three bolts.

For this reason, it is useful to minimise the pitch and yaw of the primary beam first, such that it is parallel to the translation vector of the motorised track on which the detector is mounted. This is achieved by measuring the beam position with the detector arm at 0° and at two different distances from the sample position. One position is close to the sample position (70 or 80 mm) and one much further away (320 mm or more).

Once the pitch and yaw of the beam have been minimised, the primary beam must then be translated so that it intersects with the crystal position. This is achieved by mounting a 0.4 mm diameter steel ball at the crystal position, which will block some of the beam from the detector. The steel ball is optically centred carefully within the goniometer circles, with the use of a video camera. The φ and χ circles are moved repeatedly through 90° and the steel ball is adjusted so that no change in the position is seen for any possible angle.

Once the steel ball has been centred, the generator is moved so that the shadow of the ball is visible at the centre of the primary beam on the detector. The horizontal translation should result in minimal changes to the pitch and yaw of the beam, but care must be taken when translating vertically so that the beam is still parallel to the detector track.

During the alignment of the primary beam the collimator is not attached, as the position of the collimator stand is independent of the position of the X-ray source. The stand position was set during the initial installation of the machine, and should not need to be changed unless the position of the circles ever changes or there is a collision of the equipment.

Unlike the alignment of the mirrors, the alignment of the source takes place while the shutters are closed, and these are only opened once the hutch is empty of people, the door is closed and the safety circuits are engaged. As such, no special safety precautions are required other than those taken when conducting a diffraction experiment in normal operation.

2.2.2 The Displex

2.2.2.1 Calibration

As with any cryogenic equipment, calibration of the sample temperature is vitally important. This was performed using several known structural phase transitions, covering a temperature range of 14 K to 148 K. The samples used for these phase transitions were $NH_4H_2PO_4$ (148 K), benzil (83 K), $TbVO_4$ (33 K) and $DyVO_4$ (14 K). Data points were measured above and below each phase transition, allowing at least 10 minutes for the system to equilibrate before each data point was collected.

Ammonium dihydrogen phosphate, $NH_4H_2PO_4$, (ADP) undergoes a phase transition at 148 K in which the space group changes from the tetragonal $I\bar{4}\,2\,d$ above the transition temperature to the orthorhombic $P\,2_1\,2_1\,2_1$, driven by a shift in hydrogen atom positions (Fukami *et al.*, 1987). This transition was monitored by observing the appearance of the *I*-centred systematic absences below the transition temperature, as shown in Figure 2.4.

Benzil ($C_{14}H_{10}O_2$) undergoes a phase transition at 83 K, in which the space group changes from the trigonal $P\,3_1\,2\,1$ above the transition temperature to the monoclinic $P\,2_1$ (More *et al.*, 1987). This transition was observed by measuring the unit cell at 1˚ intervals between 90 K and 75 K and monitoring the change in β angle. This angle begins to deviate from 90˚ at 83 K, as shown in Figure 2.5.

$TbVO_4$ undergoes a phase transition at 33 K from the tetragonal $I\,4_1/a\,m\,d$ at higher temperatures to the orthorhombic $F\,d\,d\,d$ at lower temperatures (Will *et al.*, 1972). This was followed by observing the 2θ angles of two reflections, (0 0 12), and (0 –12 0), which are equivalent in the tetragonal setting but not in the orthorhombic setting. The results are shown in Figure 2.6.

The lowest temperature phase transition which was chosen occurs in $DyVO_4$. At 13.8 K, the space group changes from the tetragonal $I\,4_1/a\,m\,d$ to the orthorhombic $I\,m\,m\,a$ (Göbel & Will, 1972). At higher temperatures, the (0 6 0) and (0 0 6) reflections are equivalent, but after the phase transition to the orthorhombic space group, these reflections are no longer equivalent. The variation in observed 2θ angle of these two reflections is shown in Figure 2.7.

2.2.2.2 Vacuum Shrouds

The Displex was initially supplied with two vacuum shrouds, made from beryllium. These two shrouds keep the sample under vacuum and also shield against thermal radiation. With

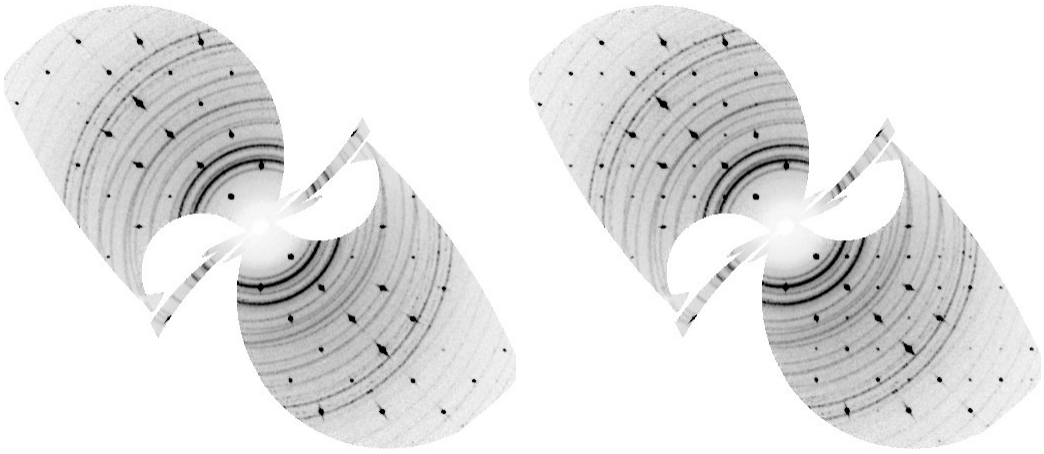

(a) 148 K (b) 147 K

Figure 2.4: Simulated precession images for the h k 0 planes of $NH_4H_2PO_4$ at (a) 148 K and (b) 147 K, showing the appearance of the *I*-centered absences below the structural phase transition.

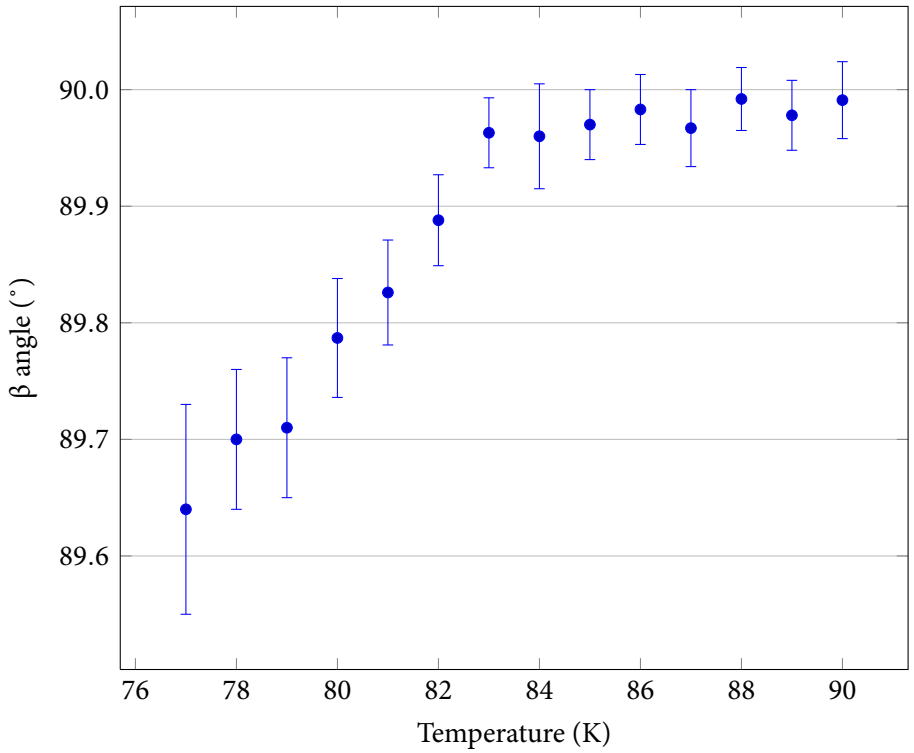

Figure 2.5: The β angle of the benzil unit cell as a function of temperature.

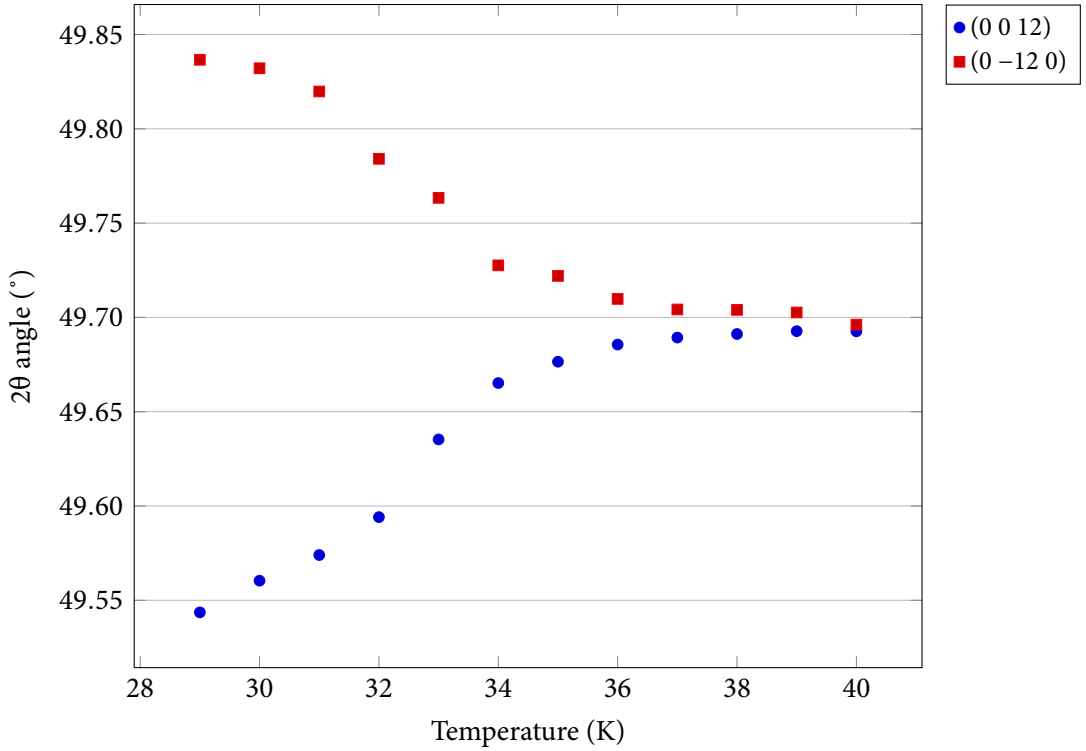

Figure 2.6: The splitting of the (0 0 12) reflection from the (0 −12 0) reflection in $TbVO_4$.

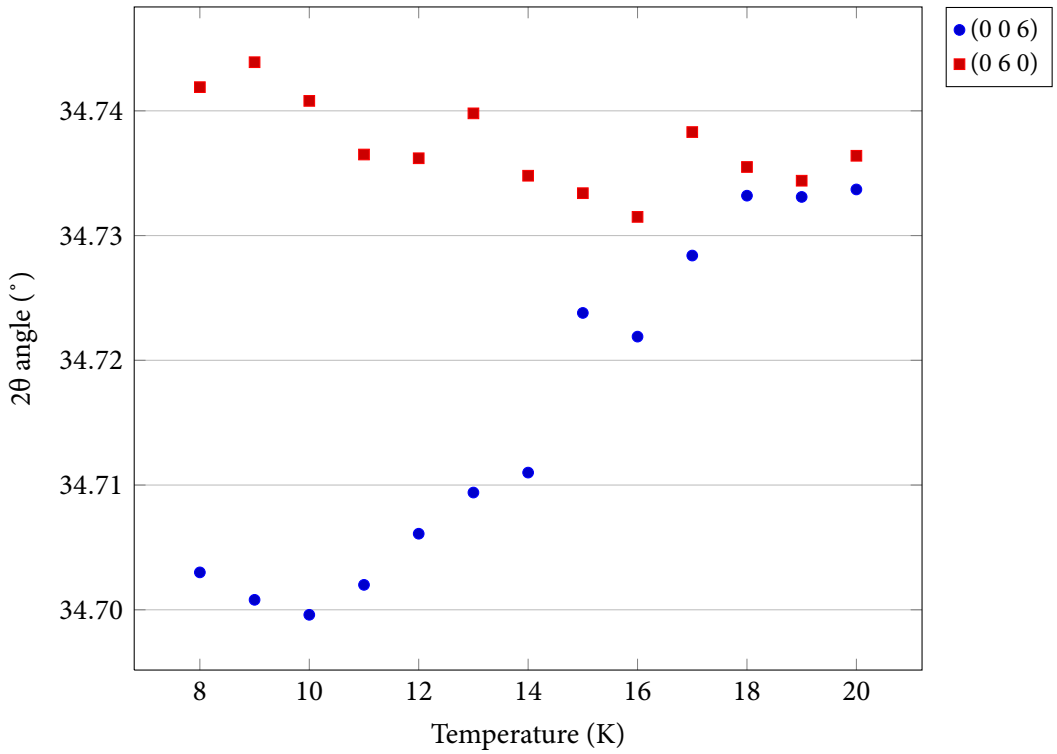

Figure 2.7: The splitting of the (0 0 6) reflection from the (0 6 0) reflection in $DyVO_4$.

these two shrouds a base temperature of 2.0 K can be reached and held for at least fourteen days. The beryllium metal does increase the background scattering, mainly in the form of powder rings in the diffraction image, but these can be mitigated (see Chapter 3).

An alternative inner shroud was constructed by Dr M. Probert from aluminium foil. The use of this shroud, along with an outer beryllium shroud, result in a slightly elevated base temperature of 3.0 K but reduce the background scattering significantly. This shroud was used during the collection of **5** and **6**.

An alternative outer shroud has also been constructed from Kapton® by Dr M. Probert, as used by Meserschmidt *et al.* (2003). This has not yet been tested due to increased risk of of the shroud breaking, necessitating an automatic shut-off switch for the vacuum pumps. Further evaluation of this shroud is ongoing (see Chapter 8).

2.3 Running Diffraction Experiments

The maximum power setting used in the Xiphos system is 5.4 kW, which corresponds to generator settings of 50 kV and 108 mA. This is also the most common power setting used to collect data, although for very strongly diffracting crystals 4 kW (50 kV and 80 mA) is sometimes used. The minimum power setting of 120 W, known as the 'standby' setting, corresponds to 20 kV and 6 mA. These are the settings used when the Xiphos is not in operation.

When starting a diffraction experiment, the generator must be powered up slowly over a series of steps. This helps to avoid arcing from the filament and the resulting damage to the electronics of the generator. As this is time consuming and error prone to do by hand, a piece of software called *Ramp* has been written to automate this process and is described in Section 7.1.4 of this work.

2.3.1 Sample Mounting

With open-flow cryostats, crystals are often mounted on glass fibres with an epoxy glue or an inert oil which freezes at low temperatures. Due to the increased thermal range over which the Displex operates, and the fact that the sample must be mounted at room temperature and then slowly cooled, the use of inert oil is not practical, and the epoxy resin chosen must be highly thermally stable.

The process for attaching samples to the third stage of the Displex is similar to that described for use with the *Fddd* diffractometer (Copley *et al.*, 1997). Crystals are mounted on a sharpened 0.5 mm graphite fibre, and attached with an epoxy resin from Oxford Instruments (TRZ0004), requiring at least 12 hours to cure. The graphite is sharpened with the use of a Dremel® multitool. The graphite is mounted in the chuck where drill bits are normally mounted and rotated at low speed against a small piece of sand-paper until a shallow point is achieved. As little graphite as possible should remain at the sample position as this adds to the background of the measured diffraction pattern.

The sample mount has been modified from the mount used on the *Fddd* diffractometer, principally to reduce the volume of material which has to be cooled between the sample and the diode which measures the temperature. The 'chuck' style arrangement to secure the graphite fibre is still used, a diagram of which is shown in Figure 2.8.

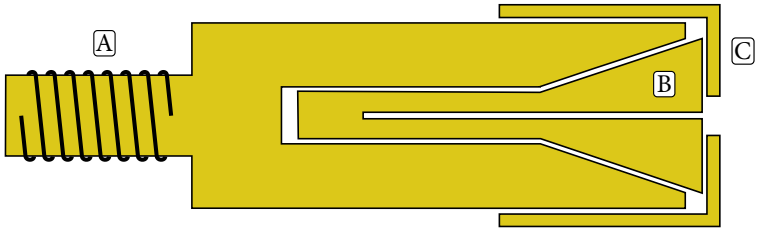

Figure 2.8: A diagram of the 'chuck' style sample holder. The mount screws into the copper block at the end of the third stage of the Displex at [A]. The graphite is placed in the block [B], and is held in place by tightening [C].

2.3.2 Crystal Centring

When performing a single-crystal diffraction experiment, the crystal is usually centred optically using a microscope or a camera by adjusting the crystal position at different values of φ. This process is also followed on the Xiphos at room temperature before the vacuum shrouds are in place. However, the sample mount and the copper block to which it is attached are cooled to the same temperature as the crystal and undergo contraction at low temperatures which can change the crystal position significantly. As a result, the crystal may have to be re-centred when the temperature is changed. Unfortunately optical centring is not possible when the beryllium or foil vacuum shrouds are used as the sample is completely obscured from view, so a different method must be employed as is described below.

The unit cell and orientation matrix of a crystal may be determined by measuring the positions of a number of sample reflections. These parameters can then be refined by least-squares against all the measured reflections. A feature of the software used for this pro-

cess, *Apex2*, allows various other parameters which may affect the unit cell determination to be refined at the same time, such as corrections for the goniometer angles and detector position, or the position of the centre of the primary beam. Crucially, another of these parameters which can be refined is the origin of the scattered reflections, *i.e.* the position of the crystal.

The corrections for the detector position are directly correlated with the parameters describing the crystal position, so if the corrections for the goniometer angles and the detector position are known in advance, these can be fixed in the refinement and the crystal position can then be freely refined. The process of determining the corrections for the goniometer angles and the detector position is described below.

The refinement of the crystal position has been found to be sensitive to uneven coverage of reciprocal space, so a set of φ scans has been designed which are used to centre the crystal in every diffraction experiment run on the XIPHOS. This provides four sections of reciprocal space, each 25° wide and spaced 90° apart, as described in Table 2.1.

Table 2.1: The φ scans used as 'standard' to centre a crystal on the XIPHOS.

2θ (°)	ω (°)	χ (°)	φ (°)	scan width (°)	Image width (°)	Direction
25.00	25.00	180.00	−102.50	25.00	0.50	positive
25.00	25.00	180.00	−12.50	25.00	0.50	positive
25.00	25.00	180.00	77.50	25.00	0.50	positive
25.00	25.00	180.00	167.50	25.00	0.50	positive

2.3.2.1 Known Corrections

In order to check the goniometer alignment, instrument manufacturers often supply standard crystals with well-documented unit cells. With the XIPHOS system, Bruker supplied two types of test crystal: a trigonal corrundum crystal with space group $R\bar{3}c$, and an 'ylid' (2-dimethylsulfuranylidene-1,3-indanedione), which forms orthorhombic crystals in the space group $P2_12_12_1$ (Guzei *et al.*, 2008).

Each time the generator and mirrors are realigned either the ruby or ylid test crystal is mounted and carefully centred optically. Both crystals are spherical, allowing this to be done to a high degree of accuracy. A comprehensive data collection is then performed with χ at 90°, 180° and 270°, and optionally values in between. This provides a highly redundant coverage of reciprocal space. The unit cell is determined and the cell parameters are refined with no constraints on the unit cell. If there are problems with the alignment or if the mirrors have been focussed so as to allow K_β through and the double beam has

not already been noticed, the unit cell angles will not refine to the known values within the expected precision (~ 0.02˚).

When the unit cell angles are constrained to their known values and the crystal centre is constrained to 0, the instrument corrections are then refined. These offsets are the detector pitch, roll, yaw and distance, and the position of the centre of the primary beam. Although these values may change slightly after the machine has been aligned no significant changes are expected, especially not for the detector corrections unless the detector has been removed and remounted. Therefore comparing these values against the previous corrections acts as a useful check of the success of the alignment process.

Table 2.2: The known corrections used after three recent machine alignments.

	Beam centre		Detector corrections			
Alignment date	x (mm)	y (mm)	distance (mm)	pitch (˚)	roll (˚)	yaw (˚)
August 2010	−0.29	+0.11	+0.54	−0.06	−0.40	−0.29
November 2010	−0.28	+0.11	+0.43	−0.02	−0.40	−0.28
April 2011	−0.27	+0.03	+0.63	−0.05	−0.40	−0.30

2.3.2.2 Moving the Crystal

When data from the centring runs described above have been collected and the unit cell has been determined, the appropriate Bravais lattice is chosen so as to reduce some of the degrees of freedom when the unit cell parameters are refined. The machine corrections are constrained to the values which were determined after the most recent machine alignment and the crystal centre is allowed to refine freely. This gives offsets for the crystal position in mm for x, y and z, which correspond to the Bruker coordinate system described in Chapter 1.

The Displex is mounted in a holder manufactured by Huber with three mutually perpendicular degrees of freedom corresponding to the same Bruker coordinate system. This allows the crystal to be centred by effectively moving the entire Displex. Typically only one axis is adjusted after each centring run to reduce the risk of overcompensating and moving the crystal significantly off centre and out of the bright part of the primary beam. This significantly reduces the observed diffraction from the crystal and makes correcting the mistake more difficult.

The height of the crystal is usually adjusted first as this tends to affect the alignment of the other two axes. This process is repeated iteratively, moving one axis at a time, until the refined values for each axis are less than 0.02 mm, which was found during testing without

the shrouds to produce results which are comparable or better to those from an optically centred crystal.

Two hundred frames are collected each time the crystal centring is adjusted meaning that the centring process can take a significant amount of time, especially if the crystal diffracts weakly. For strongly diffracting crystals where an exposure time of 1–5 seconds per frame is sufficient each centring run may take 10–15 minutes and the crystal can usually be centred within a few hours. For weakly diffracting crystals with exposure times of 20 seconds or more per frame the centring runs may take an hour to complete and it may take several days to centre the crystal after cooling from room temperature.

The initial cooling of the crystal from room temperature causes much greater contraction of the crystal mount than subsequent changes in temperature. If data is collected at several different temperatures before warming back up to room temperature, the centring process should be much faster after the crystal is centred for the first time.

2.3.3 Data Collection

Once the crystal has been centred the full data collection can begin. Due to the design of the Huber circles, data are normally collected by rotating φ and keeping χ and ω fixed, rather than rotating ω, as is more common on the Bruker SMART instruments. This is because the position of the detector limits the range of movement available in ω to a maximum of ±20˚ from the detector 2θ position, while φ can be freely rotated by the full 360˚ and is only limited by the stress on the cabling and the helium and vacuum lines at the top of the Displex.

Another limitation due to the size and weight of the Displex is the range in χ which is available. It has been found that the crystal remains centred when χ is moved to ±23˚ from 180˚. Any greater movement causes a significant shift in the crystal position so that it is no longer well centred within the X-ray beam. Data collections are therefore limited to movements of χ of ±20˚ from 180˚ in normal operation.

In a standard data collection, most of the reflection data are collected when φ is rotated by 270˚, in steps of 0.5˚, while χ is fixed at 180˚. If the crystal symmetry requires more data, χ can be moved to 160˚ and 200˚, and φ is rotated by 200˚ in steps of 0.5˚ at each χ position. In crystals with triclinic and sometimes monoclinic symmetry, depending on the orientation of the crystal on the mount, this still may not provide the required coverage of reciprocal space.

If this is the case the crystal can be warmed up to room temperature, remounted on a new

graphite fibre in a different orientation, and then cooled back down to collect more data at the required temperature. To ensure that the crystal orientation will change significantly, the crystal is affixed to another fibre while the first is still attached, and the original fibre is then carefully removed once the epoxy has dried on the second mount.

Due to the large X-ray flux available with the TXS, many crystals only require exposures of 1–5 seconds per step. The longer the exposure required, the higher the non-uniform background will be from the beryllium shrouds. For this reason, the data collection is usually repeated with one or more different detector distances. This is to allow for the possibility that the final structure can be improved through the use of *Masquerade* (Chapter 3).

The third stage of the Displex requires a constant flow of helium gas. This is supplied from commercial cylinders, and piped through a regulator to allow the pressure to be adjusted. The standard pressure used is ~ 7 bar. To maintain the low temperatures needed, the helium must be as free from impurities as possible and so it is passed through a cold trap containing liquid nitrogen. Although this is too warm to condense helium, it will restrict the flow of nitrogen, carbon dioxide and oxygen. This trap must be replenished at least once a day, often twice when running at below 10 K. The trap is in the hutch with the diffractometer so data collections may have to be interrupted briefly to accomplish this.

Apex2 offers a 'resume' function, so that a data collection may continue from the last frame collected if it is interrupted. This function appears to run through the user-specified data collection strategy, ignoring any data collection runs which have been completed, until it finds an incomplete data collection run and starts collecting data at the first missing image. The resume function does not ignore any movement commands which may have been specified, so these should be disabled before resuming the data collection.

2.4 A Study of *m*-Nitroaniline

In order to demonstrate the quality of the data which can be obtained with the Xiphos, a crystal of *m*-nitroaniline (**1**) was cooled to 2 K and data were collected. This material has been studied as part of an analysis into non-linear optical materials, including a recent charge-density study at 100 K (Pozzi *et al.*, 2009). Crystals were grown by slow evaporation of ethanol, from which a single crystal of 0.27 × 0.1 × 0.08 mm was chosen and mounted on a graphite fibre.

The crystal was cooled within two beryllium shrouds to 2 K at a rate of 1 K min^{-1}, and centred by diffraction, as described in Section 2.3.2. Data were collected using 200° φ scans of 0.5° per frame, with the detector at 80 mm from the sample. Because of the orientation of

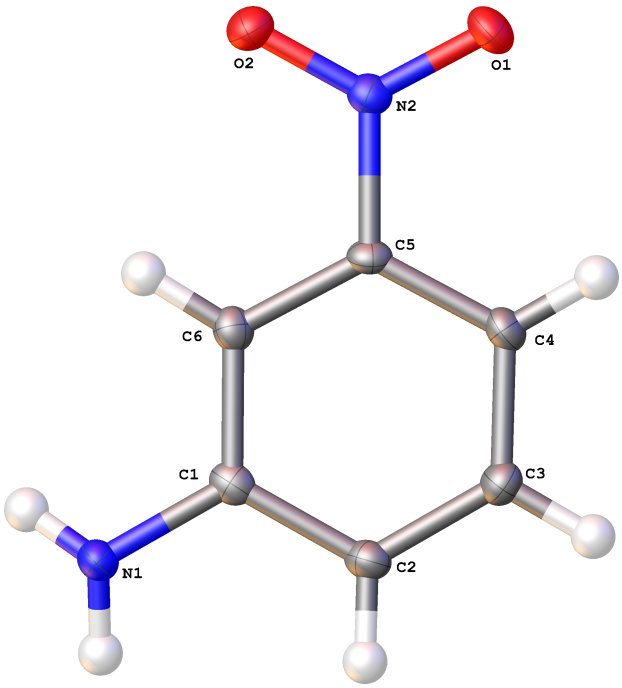

Figure 2.9: The molecular structure of **1** at 2 K, showing atom labels. Anisotropic displacement parameters are drawn at the 75% probability level.

Table 2.3: Crystal data and structure refinement of **1** at 2 K.

Empirical formula	$C_6H_6N_2O_2$
Formula weight (g mol^{-1})	138.13
Temperature (K)	2.0(1)
Crystal system, space group, Z	orthorhombic, $Pca2_1$, 4
a (Å)	18.7169(4)
b (Å)	6.5215(2)
c (Å)	5.0014(1)
Volume (Å^3)	610.48(3)
Calculated density (mg mm^{-3})	1.503
F(000)	288
Crystal size (mm^3)	0.27 × 0.1 × 0.08
Crystal shape, colour	block, clear yellow
Wavelength λ, Mo K_α (Å)	0.71073
Absorption coefficient μ (mm^{-1})	0.116
Absorption correction type	multi-scan
Ratio min/max transmission	0.8186
Maximum 2θ (°)	60.82
No. of measured reflections	9614
No. of unique reflections	993
R_{int}	0.0339
R_1, wR_2	0.0327, 0.0863
Data/restraints/parameters	993/1/115
Goodness-of-fit on F^2	1.074
Largest diff. peak/hole (e Å^{-3})	0.329/−0.220

this crystal close to 100% completeness could not be achieved given the limits in movement of χ. As a result, after collecting one set of φ scans, the crystal was removed from the graphite fibre and re-glued in a different orientation. The φ scans were then repeated, which gave a satisfactory coverage of reciprocal space: 97% complete to 60° in 2θ.

The structural refinement shows a significant reduction in the anisotropic displacement parameters compared to the study by Pozzi *et al.* (2009) at 100 K. The average value of U_{eq} for non-hydrogen atoms was 45.9% smaller at 2 K than the average at 100 K.

2.5 Conclusions

Single crystal X-ray diffraction is now routinely performed at low temperatures using open-flow nitrogen cryostats, which make temperatures down to ~ 80 K accessible. Lower temperatures, down to 30 K can be reached with a HeliX open-flow helium cryostat. To reach the ultra-low temperature regime however, closed-cycle refrigerators are required. These are most commonly installed in central facilities, rather than individual laboratories.

There is a demand for structural information on materials that show interesting phenomena at ultra-low temperatures. The relative rarity of diffractometers available to collect these data has inspired the development of the Xiphos, a new diffractometer which can be used for high-quality X-ray diffraction at temperatures as low as 2.0 K.

The Xiphos is now operational and has been used in the study of a variety of materials which display interesting behaviour at low temperatures. This is demonstrated by the range of materials studied in this work, covering organic superconductors, single molecular magnets, spin crossover systems and more.

Chapter 3

Masquerade: Generating Masks for Beryllium Rings

Of the techniques available to cool single crystals below liquid nitrogen temperatures described in Chapter 1, closed-cycle refrigerators (CCRs) are currently the only option for reaching the very lowest temperatures, such as the 2 K which is accessible with the Xiphos. In all cooling systems it is important to keep air away from the crystal as water vapour and other component gases may condense or freeze around the sample, interfering with the diffraction experiment. In gas-flow systems, the gas which provides the cooling also serves to exclude the air, allowing the sample to stay visible at all times. CCRs, however, cool by conduction so in order to exclude the air and prevent icing problems the sample must be kept under vacuum.

In the Xiphos system two cylindrical shrouds made from beryllium are used, as the beryllium is transparent to X-rays. However, the metal forming these shrouds is crystalline and hence scatters X-rays, giving rise to characteristic Debye rings in the resulting diffraction pattern (Debye & Scherrer, 1916). If the crystalline regions in the shrouds were perfectly randomly orientated, as in a powder diffraction sample with no preferred orientation effects, these diffraction rings would be uniform. It would therefore be simple to subtract the beryllium scattering from the single-crystal diffraction pattern of the sample being measured, thus allowing the extraction of accurate reflection intensities from regions contaminated by this scattering.

However, because the shrouds contain larger crystallites which are not uniformly distributed, the resulting beryllium diffraction rings do not yield a uniform intensity. This makes it impossible to accurately calculate the frame background in these regions and therefore the associated σ for the reflection, which may negatively affect the accuracy of

the sample reflection intensities that are subsequently extracted.

For strongly diffracting crystals the sample reflections are much stronger than those of the beryllium crystallites within the shrouds and there is little resulting effect on the extracted intensities. However, for weakly diffracting crystals the sample reflections are of the same order of magnitude as the beryllium scattering from the shrouds and the extracted intensities may not be measured accurately.

To reduce the impact of the contamination of the measured sample reflection intensities, overlays can be generated for each frame to describe the position of the beryllium diffraction rings. These overlays are referred to as 'masks'. These masks are used during the process of extracting the sample reflection intensities, known as integration, by the Bruker software designed for this purpose, *SAINT* (Bruker, 2009). If, in the process of integrating a reflection, any part of that reflection overlaps with one of the diffraction rings from the mask, the whole reflection is ignored and will not be part of the program output. If the mask accurately describes the beryllium diffraction pattern, only sample reflections that are unaffected by the beryllium contamination will be in the program output after processing.

The diffraction pattern of beryllium is well characterised (Gordon, 1949). With knowledge of the X-ray radiation wavelength, beryllium unit cell, and space group, the 2θ reflection angles can be calculated. However, as the beryllium shrouds scatter from a different origin to the sample position, these calculated angles will not correspond directly to the 2θ angles measured by the X-ray detector, which assumes that all scattering originates at the position of the crystal. Further calculation is required to determine the corrected beryllium diffraction positions for use as the masks, based on the distance of the shroud walls to the sample position along the path of the incident X-ray beam, which is described herein.

A further consequence of the distance between the sample position and the beryllium shroud walls is that the scattering vectors of the sample reflections and the beryllium have different origins, as shown in Figure 3.1. This means that if a beryllium diffraction ring and a sample reflection coincide on the detector at one detector distance (position a), they may be separated by changing the distance of the detector from the sample (position b). Hence if the data collection is repeated with the detector at multiple distances from the sample, reflections which are discarded due to contamination at one detector distance may be measured without contamination at a different detector distance. The results of this approach are described below.

A new computer program called *Masquerade* has been written to perform the calculations described in this chapter and create masks for the beryllium scattering. The program is

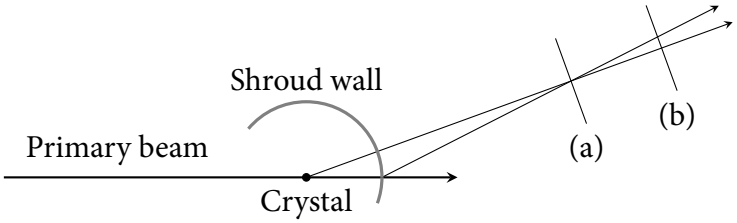

Figure 3.1: Schematic diagram showing scattered beam vectors of reflections from the sample and one of the vacuum shrouds. These are coincident on the detector at distance (a), but have separated at position (b).

written in C++, and it has been found to improve data quality in studies of crystals with weak diffraction such as cytidine (described in this chapter) as well as two other compounds described in later chapters. This work has also been published in the *Journal of Applied Crystallography* (Coome *et al.*, 2012).

3.1 The Distance Between the Crystal and the Shroud Wall

The pattern of rings produced by the scattering from the beryllium shrouds depends on the position of the shroud at the point where it is intersected by the primary X-ray beam. As the crystal position is at the centre of rotation of all the goniometer circles, it is convenient to measure the shroud position as the distance between the crystal and the shroud wall along the vector of the primary beam. Several approaches to this calculation were attempted until a satisfactory result was achieved, and these are detailed here.

3.1.1 Initial Approach

An initial model was proposed in which the beryllium shrouds were centred around the crystal position. In this model, the distance between the shroud walls and the crystal position, r', is simply the radius of each shroud, r, as long as either ω and χ are 0 or 180°. If both of these angles have other values, the shroud will move in such a way as to change the distance from the walls to the sample in the direction of the primary beam. The calculations to determine this distance are outlined below.

The intersection of a plane and a cylinder gives an ellipse, as long as the plane does not pass through the end of the cylinder. The shrouds in use on the Xiphos have steel ends which would absorb the direct beam, and the movements required for this position would cause the Displex to be in collision with the generator, so this condition may be ignored.

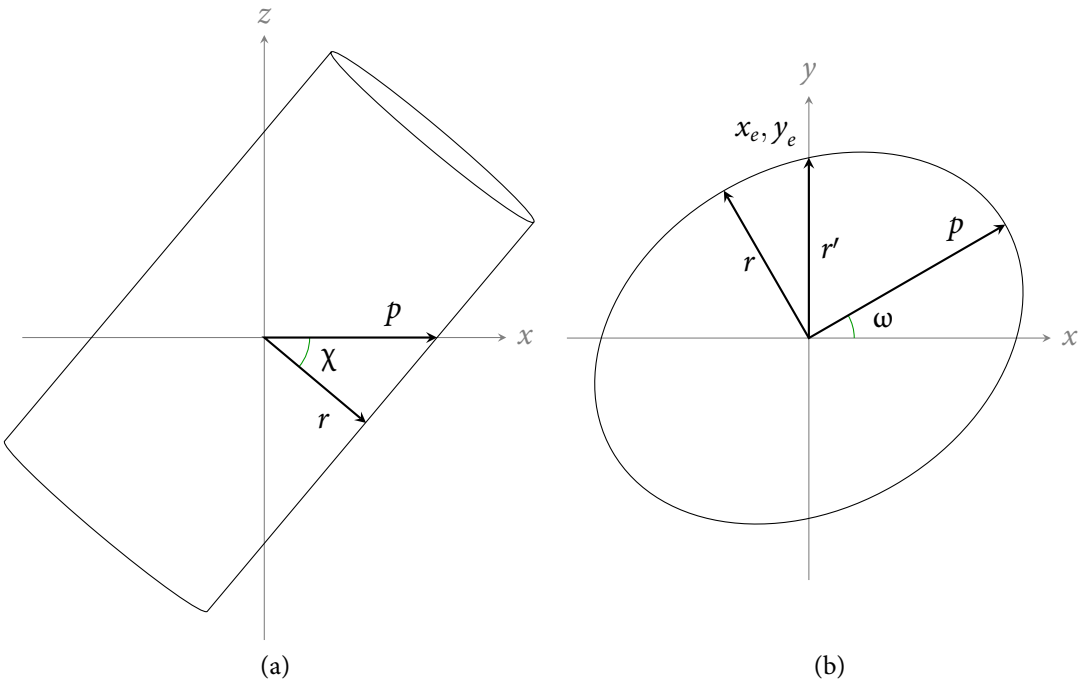

Figure 3.2: The distance between the crystal and the shroud walls as a function of ω and χ, showing (a) the view from the side of the shroud, perpendicular to χ, and (b) the view from above, down the z axis.

When χ is moved, the ellipse created by the intersection of the x, y plane with the shroud with minor axis r (the shroud radius) and major axis p, shown in Figure 3.2a. The length of the major axis can be calculated with simple trigonometry, as follows:

$$p = \frac{r}{\cos \chi} \tag{3.1}$$

When the shroud is also rotated by ω, the path length travelled by the direct beam between the crystal and the shroud wall is given by r', shown in Figure 3.2b. The coordinates x_e and y_e represent the intersection point of the primary beam with the shroud wall, and are most easily calculated in a modified coordinate system in which the x axis is parallel to p, and the y axis is parallel to r.

The equation of this ellipse is then given by the following equations, using the expression for p in Equation 3.1.

$$\frac{x_e^2}{p^2} + \frac{y_e^2}{r^2} = 1 \tag{3.2}$$

$$\frac{x_e^2 \cos^2 \chi}{r^2} + \frac{y_e^2}{r^2} = 1 \tag{3.3}$$

$$x_e^2 \cos^2 \chi + y_e^2 = r^2 \tag{3.4}$$

The coordinates x_e and y_e can be parametrised in terms of r' and ω,

$$x_e = r' \sin \omega \tag{3.5}$$

$$y_e = r' \cos \omega \tag{3.6}$$

which can then be substituted into Equation 3.4:

$$\begin{aligned} r^2 &= r'^2 \sin^2 \omega \cos^2 \chi + r'^2 \cos^2 \omega \\ &= r'^2 (\sin^2 \omega \cos^2 \chi + \cos^2 \omega) \end{aligned} \tag{3.7}$$

The distance between the crystal and the shroud wall, r', can therefore be calculated with Equation 3.8 below. It can be seen that if either ω or χ is 0 or 180°, the denominator becomes 1, and hence r' becomes equal to r.

$$r' = \frac{r}{\sqrt{\sin^2 \omega \cos^2 \chi + \cos^2 \omega}} \tag{3.8}$$

After this was implemented it was observed that even when ω and χ are fixed, the beryllium rings change position on the detector when φ is changed. It was then observed that the process used to centre the crystal, in which the whole Displex must be moved, dictates that the centre of the shrouds is not coincident with the crystal position. In order to model this, an offset between the centre of the shroud and the centre of the goniometer is required. It was also observed that the beryllium rings from each of the shrouds moved relative to each other during data collection, requiring a separate offset for each shroud.

3.1.2 Ray-Casting

There are two perpendicular offsets for each shroud, x_t and y_t. No offsets are required for z, as the shroud is modelled as an infinite cylinder which extends parallel to z. Incorporating

these offsets into the equation to calculate the shroud-to-detector distance required a different approach. A technique in computer graphics which deals with similar problems is that of ray-tracing, which is already used to good effect in the *EVAL15* integration program (Schreurs *et al.*, 2010).

Ray-tracing (or the more simplified version known as ray-casting used here) creates an image by directing 'beams' of light from a common centre, sometimes referred to as an 'eye-point'. These follow a specified trajectory until they hit an object in the scene being modelled. How the beam is reflected and what it subsequently hits are used to generate the image. The distance from the eye-point to the object is calculated as part of this process.

The ray is defined by an eye-point, $\mathbf{E}$, and a unit direction vector, $\mathbf{D}$:

$$\mathbf{E} = (x_E, y_E, z_E) \tag{3.9}$$

$$\mathbf{D} = (x_D, y_D, z_D) \tag{3.10}$$

At the point where the ray intersects with an object, it will have a length, l, and hence the full equation for the ray is as follows.

$$\mathbf{P}(l) = \mathbf{E} + l\mathbf{D} \qquad (l \geq 0) \tag{3.11}$$

The equation for an infinite cylinder of radius, r, aligned along the z axis is $x^2 + y^2 = r^2$, hence the point where the ray and the cylinder intersect is

$$(x_E + lx_D)^2 + (y_E + ly_D)^2 = r^2 \tag{3.12}$$

The distance between the crystal position and the walls of the shroud can therefore be calculated by solving the following equation:

$$l^2(x_D^2 + y_D^2) + l(2x_E x_D + 2y_E y_D) + (x_E^2 + y_E^2 - r^2) = 0 \tag{3.13}$$

To move the shroud in 3D space it is first translated by the offsets (which are determined in Section 3.2), then it is rotated by φ, χ and ω. If the ideal shroud position, attached to the φ axis and centred about the crystal, is represented by $\mathbf{C}'$, the real position in space, $\mathbf{C}$, can be found from $\mathbf{C} = \mathbf{RTC}'$ where $\mathbf{T}$ is a matrix representing the translation by the offsets and $\mathbf{R}$ is a matrix describing the rotations.

In these calculations, however, the cylinder is not moved, but the eye-point and offset vectors are moved instead. The eye-point is rotated and translated; the offset vector is only rotated.

$$\mathbf{E}' = \mathbf{T}^{-1}\mathbf{R}^{-1}\mathbf{E} \tag{3.14}$$

$$\mathbf{D}' = \mathbf{R}^{-1}\mathbf{D} \tag{3.15}$$

In order to measure the distance between the crystal and the shroud wall the eye-point is placed at the crystal position, which is initially set to $(0, 0, 0)$. A pure rotation will move a point around the origin but if the point is at the origin this will have no effect. Therefore the only transformation that will apply is the translation, hence $\mathbf{E}' = (-x_t, -y_t, -z_t)$. As the shroud is modelled as an infinite cylinder any offset about z will have no effect and hence z_t does not feature in the following equations.

The direction vector on the other hand initially points along y, so initially $\mathbf{D} = (0, 1, 0)$. The rotation matrix, **R**, describes the rotation of the shroud by the goniometer angles φ, χ and ω, hence $\mathbf{R} = \mathbf{\Omega X \Phi}$.

The rotation matrices for each of these angles is as follows:

$$\mathbf{\Omega} = \begin{pmatrix} \cos\omega & \sin\omega & 0 \\ -\sin\omega & \cos\omega & 0 \\ 0 & 0 & 1 \end{pmatrix} \tag{3.16}$$

$$\mathbf{X} = \begin{pmatrix} \cos\chi & 0 & -\sin\chi \\ 0 & 1 & 0 \\ \sin\chi & 0 & \cos\chi \end{pmatrix} \tag{3.17}$$

$$\mathbf{\Phi} = \begin{pmatrix} \cos\varphi & \sin\varphi & 0 \\ -\sin\varphi & \cos\varphi & 0 \\ 0 & 0 & 1 \end{pmatrix} \tag{3.18}$$

The matrix $\mathbf{R} = \mathbf{\Omega X \Phi}$, once inverted, is multiplied by **D** to give:

$$\mathbf{D}' = \begin{pmatrix} -\sin\omega\cos\chi\cos\varphi - \cos\omega\sin\varphi \\ -\sin\omega\cos\chi\sin\varphi + \cos\omega\cos\varphi \\ \sin\omega\sin\chi \end{pmatrix} \tag{3.19}$$

The expressions for $\mathbf{D}'$ and $\mathbf{E}'$ can be used in Equation 3.13 to find the distance between the crystal and the shroud wall parallel to the X-ray beam, as follows:

$$l = \frac{-b \pm \sqrt{b^2 - 4ac}}{2a} \tag{3.20}$$

where

$$a = \cos^2\chi + \cos^2\omega - \cos^2\chi\cos^2\omega$$

$$b = 2x_t(\sin\omega\cos\chi\cos\varphi + \cos\omega\sin\varphi) + 2y_t(\sin\omega\cos\chi\sin\varphi - \cos\omega\cos\varphi)$$

$$c = x_t^2 + y_t^2 - r^2$$

When the shrouds are centred at exactly the same point as the crystal, x_t and y_t are both 0. When this is substituted into the above equation, $b = 0$, and $c = -r^2$. Equation 3.20 can therefore be simplified as follows:

$$l = \frac{-0 \pm \sqrt{0^2 + 4r^2(\cos^2\chi + \cos^2\omega - \cos^2\chi\cos^2\omega)}}{2(\cos^2\chi + \cos^2\omega - \cos^2\chi\cos^2\omega)} \tag{3.21}$$

$$= \frac{r\sqrt{\cos^2\chi + \cos^2\omega - \cos^2\chi\cos^2\omega}}{2(\cos^2\chi + \cos^2\omega - \cos^2\chi\cos^2\omega)} \tag{3.22}$$

Using the identities $\frac{\sqrt{n}}{n} \equiv \frac{1}{\sqrt{n}}$ and $\sin^2 x \equiv 1 - \cos^2 x$, it can be seen that this equation is identical to Equation 3.8, as expected. The equation now has no dependence on φ and, as expected, the result is simply the radius of the shroud, r, when either χ or ω (or both) are equal to 0° or 180°.

3.2 Calculating the Offsets

While the shroud offsets could theoretically be measured, they can also be calculated from the diffraction pattern. Since the scattering angles of beryllium are known, the origin of the reflected beam can be calculated from the detector positions.

From any point on the detector, a vector can be calculated from that position to the centre of the crystal, known as the $\mathbf{S}_1$ vector, shown in Figure 3.3. The distance from the detector to the crystal in the direction of the primary beam is simply the y component of the $\mathbf{S}_1$ vector,

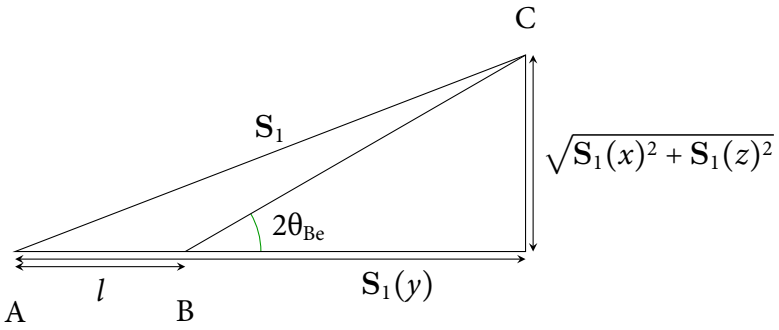

Figure 3.3: Calculating the distance between the shroud wall and the crystal, l. The crystal position is at point A, the shroud wall is at point B, and the detector impact point is at C.

represented by $\mathbf{S}_1(y)$. The distance perpendicular to the beam is $\sqrt{\mathbf{S}_1(x)^2 + \mathbf{S}_1(z)^2}$. From this $\mathbf{S}_1$ vector, if the scattering angle of the ring is known, the distance between the centre of the crystal and the shroud wall can be calculated with Equation 3.23.

$$l = \mathbf{S}_1(y) - \frac{\sqrt{\mathbf{S}_1(x)^2 + \mathbf{S}_1(z)^2}}{\tan 2\theta_{\mathrm{Be}}} \tag{3.23}$$

Since the shrouds are cylindrical, the distance l depends on both x_t and y_t for all orientations of the shroud. This is shown in the following equation, where for a shroud of radius r, a point on the shroud wall described by (x, y) satisfies:

$$(x + x_t)^2 + (y + y_t)^2 = r^2 \tag{3.24}$$

When the shroud is rotated so that its y axis is perpendicular to the X-ray beam, the y component of the measured distance becomes 0 and the same is true for the x component when the x axis is perpendicular to the beam. This leads to two expressions for the offsets when the shroud is rotated around z to two positions, 90° apart from each other.

$$y_t^2 + (x + x_t)^2 = r^2 \tag{3.25}$$

$$x_t^2 + (y + y_t)^2 = r^2 \tag{3.26}$$

By using Equation 3.23 to measure the distance between the shroud walls and the crystal when the shroud y axis is parallel to the goniometer y axis, y_1, and again when the shroud is rotated by 180°, y_2, a pair of these equations can be equated, eliminating the term for x_t and allowing y_t to be determined from Equation 3.27. These two distances y_1 and y_2 are shown in Figure 3.4.

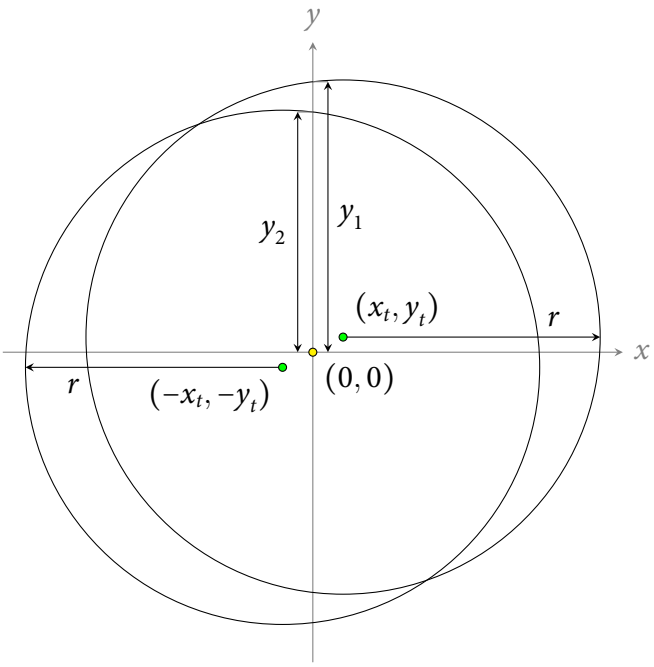

Figure 3.4: Calculating the shroud offsets from the measured crystal-to-shroud distances.

$$\begin{aligned} x_t^2 + (y_1 + y_t)^2 &= x_t^2 + (y_2 - y_t)^2 \\ (y_1 + y_t)^2 &= (y_2 - y_t)^2 \\ y_t &= \frac{y_2 - y_1}{2} \end{aligned} \tag{3.27}$$

Once y_t is known, this and one of the measured y values could be substituted into Equation 3.26 to determine x_t. However, only the absolute value can be determined this way, not the sign, so the distance between the shroud and the crystal must be measured a third time, this time with the shroud rotated around z by 90° to both of the previous measurements. This new value, x_1, can be used to determine the value and sign of x_t from Equation 3.25 using the known value of y_t:

$$\begin{aligned} (x_1 + x_t)^2 + y_t^2 &= r^2 \\ (x_1 + x_t)^2 &= r^2 - y_t^2 \\ x_t &= -x_1 \pm \sqrt{r^2 - y_t^2} \end{aligned} \tag{3.28}$$

The only solution that gives a physically reasonable result for x_t (*i.e.* less than the shroud radius) is the positive solution to the square root, so the negative root can be ignored.

3.3 Generating the Masks

Once the calculations have been performed to determine the shroud offsets, these values can be used to generate masks to describe the beryllium reflections. For this process a program called *Masquerade* has been written in C++, which uses the frames generated as part of the diffraction experiment and generates a corresponding mask for each frame. The offsets are calculated separately and are then used with Equation 3.20 and the goniometer angles contained in the frame header to calculate the distance between the shroud wall and the sample position for each frame.

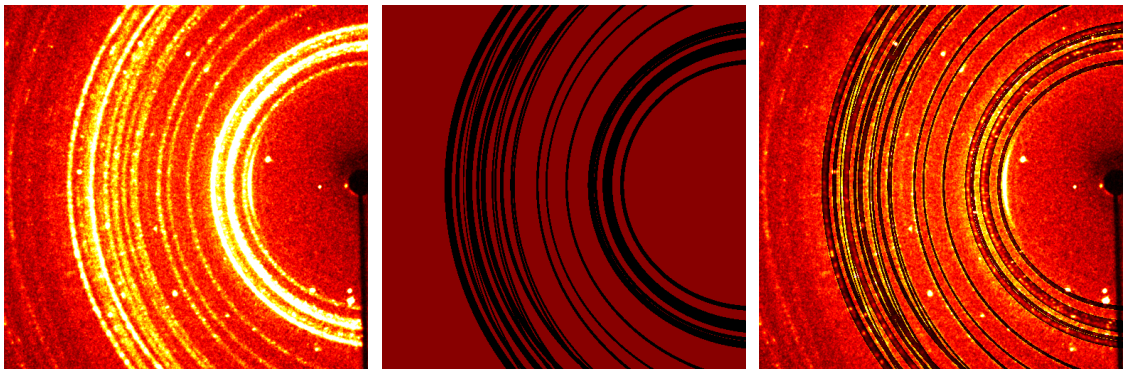

(a) (b) (c)

Figure 3.5: An example from the diffraction pattern of **6** at 2 K. This shows: (a) the frame as collected by the detector, (b) the mask generated by *Masquerade* using the 7 lowest-angle beryllium reflections and (c) the overlay of the frame and the mask (made translucent), showing the good agreement between them.

An example of the produced mask file is shown in Figure 3.5. This shows the original frame file as collected by the CCD detector (a) and the mask image that is produced by *Masquerade* for this input (b). Finally, the mask is overlaid on the image to show the excellent agreement between the observed and the calculated beryllium diffraction rings (c).

Each mask image is generated pixel by pixel in *Masquerade*. To determine whether a pixel will be affected by the beryllium scattering, the $\mathbf{S}_1$ vector is calculated for that pixel (see Section 1.1.4.1). The origin of this vector is moved from the crystal to each shroud wall in turn, using the distances from the crystal to the shroud walls using the goniometer angles in the frame header as calculated using the equations above. The angle is then calculated between this modified $\mathbf{S}_1$ vector and the primary beam. If it matches one of the known beryllium scattering angles including a small angle to account for the thickness of the beryllium rings, the pixel is considered contaminated by beryllium scattering and value of 0 is written to the mask file for that pixel, otherwise the pixel is considered unaffected and a value of 64 is written to the mask image for that pixel.

The calculations for each pixel are completely independent, making the mask generation process easy to run in parallel. Most modern computers have more than one independent calculation unit, or 'core', but code is generally written so that instructions follow each other sequentially, thus making use of only one core. Therefore, parallelism must be explicitly added by the programmer in order to speed up the program and make use of all the available cores.

Not all parts of the *Masquerade* process can be split up easily, such as the code which reads frame files. However, the mask generation process uses a loop which calculates whether each pixel is contaminated and this can be made to run the calculations for multiple pixels in parallel with minimal effort using OpenMP, a specification providing a simple and flexible interface for developing parallel applications (a description of which can be found in Chapman *et al.*, 2007). The calculations to determine whether a pixel is obscured by the beryllium scattering account for a significant proportion of the time required to generate the mask files. Large amounts of time can therefore be saved by running the calculations in parallel on all the processing units of a multi-core processor.

3.3.1 Mask Format

Masks use the same format as the image files (frames). The first part of the frame is the header section, made up of items of 80 characters, encoded in ASCII format, in which one character uses one byte. Each item has a 7 character name or keyword, followed by the values which are formatted differently depending on the item. The header consists of a number of 512 byte blocks, of which there are usually 15 present. There may be padding at the end if there are not enough items present to fill the last block.

The detector image is made up of binary intensity values, one for each pixel of the detector. Each intensity is added to a base value which is specified in the header. The intensity values are represented by 1, 2 or 4 bytes per pixel, and this storage size is specified in the header. Any values which are too large for the storage size specified can be looked up in the overflow tables at the end of the file. If this is the case, the value stored will be the largest possible given the storage type, so `0xFF` for 1-byte values, or `0xFFFF` for 2-byte values. Pixel values of 0 may correspond to underflows for any intensity below the base value, and these underflows are also specified at the end of the file.

These overflow and underflow tables have different formats depending on the software used to generate them, which can be determined from the version specified in the header. The older frames use an ASCII lookup table, where each value is specified by a 7 byte key and a 9 byte value.

The more modern frames use a series of binary overflow tables. The overflows are specified in the order that the values appear in the image. If the image is made of 1-byte values, there will be two overflow tables, one for values which fit into 2 bytes, and one for values which fit into 4 bytes. If the image is made of 2-byte values, only the 4-byte overflow table is present. If a value is too large to fit into the 2-byte overflow table, `0xFFFF` is written into that table, and the true value must be looked up in the next position in the 4-byte overflow table.

3.4 Cytidine at 100 K

The well-known compound cytidine (Furberg, 1950; Furberg *et al.*, 1965) was used to examine the effects of using *Masquerade*. A crystal measuring 0.25 × 0.1 × 0.05 mm was crystallised from 9:1 EtOH:H_2O. This was initially cooled to 100 K at 1 K min^{-1}. Crystal centring and data collection were completed using the *Apex2* software suite (Bruker, 2010). A sequence of φ scans was collected with the detector at 70 mm from the crystal. These φ scans were repeated with the detector moved away from the crystal at 10 mm intervals to a final distance of 120 mm. These were collected to determine the optimal combination of detector distances for which the largest number of reflections can be processed when using *Masquerade*.

The reflections were integrated for each detector distance separately using *SAINT*, with and without the masks generated by *Masquerade*. The data from these runs were then combined using *XPREP* (Sheldrick, 2008b), to determine how many reflections could be recovered and what effect this had on the data quality and subsequent least-squares refinement of the data.

3.4.1 Generating the Masks

The shroud offsets were calculated from the first φ scan with the detector at 70 mm from the sample and with a detector 2θ angle of 20°. The positions on the detector of the (1 0 1) beryllium reflection, which has a true 2θ value of 23.667° for Mo K_α radiation, were measured for both shrouds.

Throughout the run, ω was set to 30° and χ was set to 180°. In the Bruker angle conventions, ω is a right-handed rotation and φ is left-handed, so with χ at 180°, φ is effectively upside-down and hence the circles rotate in the same direction. In order to calculate the offsets in the laboratory coordinate system, pixel positions of the (1 0 1) beryllium reflection on the

Table 3.1: Calculating the distance between the shroud wall and the crystal using the (1 0 1) beryllium reflection. The x pixel position of the strongest ring was located at the point where the y pixel was 256.

(a) Inner shroud

Rotation (°)	x_{pixel}	distance (mm)
0	299	24.8183
90	301	25.4151
180	206	26.9071

(b) Outer shroud

Rotation (°)	x_{pixel}	distance (mm)
0	314	30.8875
90	320	32.6779
180	332	36.2587

detector were measured with φ at −30°, 60°, and 150°, to correspond to shroud rotations of 0°, 90° and 180° about the z axis.

From the measured pixel positions on the detector of the (1 0 1) beryllium reflections the $\mathbf{S}_1$ vectors to the crystal were determined, and using Equation 3.23 the distances from the detector to the shroud were calculated, the results of which are shown in Table 3.1. Using Equation 3.27 to calculate y_t and Equation 3.28 to calculate x_t, the shroud offsets were found, and are shown in Table 3.2.

Table 3.2: The calculated shroud offsets using the distances in Table 3.1.

Shroud	x_t (mm)	y_t (mm)
Inner	0.0986	1.0444
Outer	0.4283	2.6856

The calculated offsets were then added to the configuration file for *Masquerade*, which also contains the shroud radii, and the beryllium reflections for which masks should be generated, shown in Listing 3.1. Only the three most intense beryllium reflections which are most problematic for *SAINT*'s background calculation were chosen. These reflections were (1 0 0), (0 0 2) and (1 0 1). With two shrouds and hence four reflection origins, this generates a complex pattern of 12 rings.

With this input, *Masquerade* was run, generating 8760 mask files in 6 minutes and 30 seconds, using an Intel Q9450 Core2 Quad processor.

Listing 3.1: *Masquerade* input file, used to generate the masks used with the cytidine data collected at 100 K.

```
shrouds = (
    {
        radius = 25.535;
        spread = 0.6;
        corrections = {
            x =   0.0986;
            y =   1.0444;
        };
        reflections = (
            {
                two_theta = 20.682;
                spread    = 0.5;
            },
            {
                two_theta = 22.873;
                spread    = 0.5;
            },
            {
                two_theta = 23.667;
                spread    = 1.0;
            });
    },
    {
        radius = 33.215;
        spread = 0.6;
        corrections = {
            x =  -0.4283;
            y =   2.6856;
        };
        reflections = (
            {
                two_theta = 20.682;
                spread    = 0.5;
            },
            {
                two_theta = 22.873;
                spread    = 0.5;
            },
            {
                two_theta = 23.667;
                spread    = 1.0;
            });
    });
```

3.4.2 Results

To determine whether higher quality data can be obtained by masking the beryllium rings during integration, the data collected with the detector at 70 mm, integrated with and without masks, were used to refine the structure of cytidine using *SHELXL* (Sheldrick, 2008a).

Table 3.3: A comparison of the data quality observed with and without masks generated by *Masquerade*.

	Masked	Unmasked
R_1 ($I > 4\sigma$)	0.0443	0.0545
R_1 (all)	0.0554	0.0609
wR_2	0.0986	0.1150
R_{int}	0.0739	0.1024
R_σ	0.0634	0.0727
C–C bond precision (Å)	0.0038	0.0042

The results of these refinements can be seen in Table 3.3. The structures are visually highly similar, as shown in Figure 3.6, but the data statistics show an improvement in the R_1 factors calculated with all reflections, and with only those for which $I > 4\sigma(I)$. There is also a reduction in the value of wR_2 for the data integrated with masks. It can also be seen that the integrated intensities are more internally consistent when masks are used, as the R_{int} and R_σ values are both lower for the masked intensities. Finally, the C–C bond length precision calculated by the IUCr's checkCIF service (`http://checkcif.iucr.org`) is also improved when *Masquerade* is used.

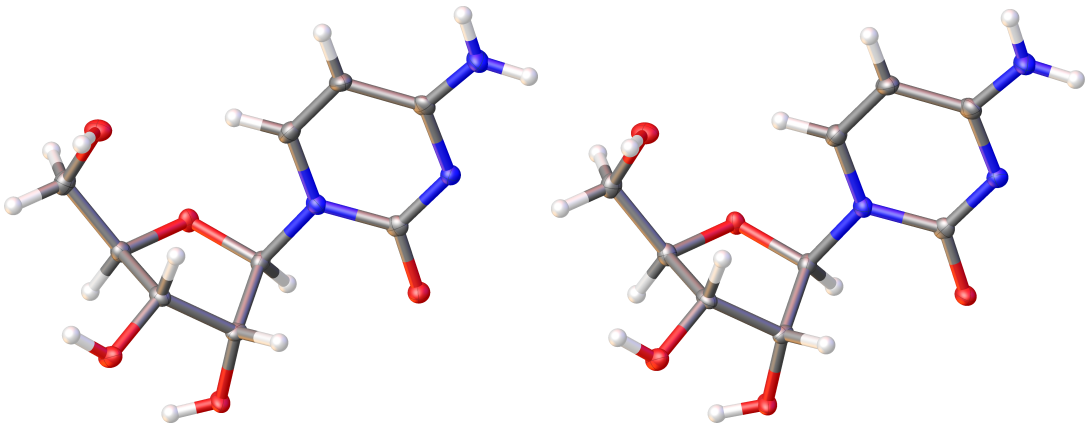

(a) Data collected with the detector at 70 and 120 mm and integrated with masks

(b) Data collected with the detector at 70 mm only and integrated without masks

Figure 3.6: A comparision of the refined structures at 100 K with and without masks, showing the visual similarity between (a) the masked structure and (b) the unmasked structure.

Table 3.4: The number of reflections that could be integrated with and without masking.

	Unique		Total	
Detector Distance (mm)	Masked	Unmasked	Masked	Unmasked
70	1739	2017	6228	8217
80	1688	1964	5289	7016
90	1619	1906	4475	6007
100	1475	1757	3744	5078
110	1328	1594	3168	4277
120	1219	1467	2714	3676

The only area in which the unmasked data have an advantage is in data completeness, as shown in Table 3.4. From the data collected at 70 mm alone, 278 unique reflections are not integrated due to the masks, representing 13.8% of the observable reflections given the experimental design.

Table 3.5: The number of reflections regained with two detector distances. Completeness shows the number of unique reflections compared to the number which were measured without masks.

Detector Distances (mm)	Unique	Total	Completeness (%)
70 + 120	1918	8942	95.09
70 + 110	1901	9396	94.25
70 + 100	1875	9972	92.96
70 + 90	1864	10703	92.41
70 + 80	1847	11517	91.57
80 + 120	1820	8003	90.23
80 + 110	1803	8457	89.39
80 + 100	1785	9033	88.50
80 + 90	1761	9764	87.31
90 + 120	1719	7189	85.23
90 + 110	1712	7643	84.88
90 + 100	1682	8219	83.39
100 + 120	1542	6458	76.45
100 + 110	1527	6912	75.71
110 + 120	1366	5882	67.72

These missing reflections can be recovered by collecting data at different detector distances. The number of reflections for which intensities were integrated when data from two different detector distances are combined using *XPREP* is shown in Table 3.5. The greatest number of unique reflections when masks are used is available with the detector at 70 mm and 120 mm. From 1739 unique reflections measured when the detector is at 70 mm alone, the data collected at 120 mm add a further 179 reflections, bringing the completeness to

95.1% of the reflections which can be integrated when masks are not used.

The intensities from these combined detector distances were then used to refine the cytidine structure again. When compared with the unmasked data alone, it can be seen in Table 3.6 that the statistics are improved by the addition of data collected at a second detector distance, suggesting that the addition of intensities from reflections which were not affected by the beryllium scattering has brought the average intensity closer to the true value.

Table 3.6: A comparison of the data quality observed with and without masks generated by *Masquerade*, and how this is further improved by combining data from two detector distances.

	Masked		Unmasked	
	70 + 120 mm	70 mm	70 + 120 mm	70 mm
R_1 ($I > 4\sigma$)	0.0413	0.0443	0.0481	0.0545
R_1 (all)	0.0505	0.0554	0.0548	0.0609
wR_2	0.0985	0.0986	0.1091	0.1150
R_{int}	0.0941	0.0739	0.1239	0.1024
R_σ	0.0642	0.0634	0.0664	0.0727
C–C bond precision (Å)	0.0035	0.0038	0.0040	0.0042

The greatest improvement in data quality can be seen when masks are used during integration, shown in Table 3.6, which demonstrates the value of using *Masquerade* and collecting at two detector distances to recover missing reflections. The combination of data from two detector distances shows improvement in R_1, wR_2, R_{int} and R_σ over the same data integrated without masks, and an even more pronounced improvement over the data collected at only one detector distance.

Table 3.7: The number of reflections integrated as the number of detector distances increases. Completeness shows the number of unique reflections compared to the number which were measured without masks.

Detector Distances (mm)	Unique	Total	Completeness (%)
70 + 80 + 90 + 100 + 110 + 120	1978	25618	98.07
70 + 80 + 90 + 110 + 120	1977	21874	98.02
70 + 80 + 90 + 120	1974	18706	97.87
70 + 80 + 120	1958	14231	97.07
70 + 120	1918	8942	95.09
70	1739	6228	86.22

Combining data collected at three or more detector distances was also investigated. This provides more unique reflections, as can be seen in Table 3.7, but the minor improvements

resulting were not considered to be justified by the much longer experimental time required.

Table 3.8: Comparison of unit cell parameters between the masked data collected at two detector distances at 100 K and the previously reported structure at 123 K.

Cell Parameters	100 K	123 K[a]
a (Å)	5.0850(3)	5.076(1)
b (Å)	13.9065(9)	13.925(1)
c (Å)	14.7043(10)	14.715(1)
Volume (Å^3)	1039.81(12)	1040.10(22)

[a] Data taken from Chen & Craven (1995).

The final structure, integrated with masks generated by *Masquerade* and using reflection intensities collected with the detector at 70 mm and 120 mm was compared to a previously published structure, collected at 123 K (Chen & Craven, 1995). The unit cell parameters from both studies are shown in Table 3.8. The differences are minimal, with the unit cell volume remaining the same within error. No major changes in bond lengths were observed between the two structures.

3.5 Cytidine at 2 K

The data collected at 100 K were used primarily to determine the best data collection routines to use with *Masquerade*, but these do not provide any structural data that could not have been more easily collected with a standard nitrogen cryostat.

The Xiphos system was designed to reach much lower temperatures which are generally not achievable in a laboratory setting. The cytidine crystal with which data were collected at 100 K was thus cooled to the lowest available temperature: 2 K. The crystal was cooled at a rate of 1 K min^{-1}, and when it had stabilised after approximately four hours it was re-centred to account for the contraction of the mount. Data were then collected with the detector at both 70 mm and 120 mm.

Due to the contraction of the copper crystal mount on cooling described in Section 2.3.2, the crystal had to be re-centred. This caused a small shift in the position of the beryllium shrouds, and hence new masks had to be generated by *Masquerade*. The frame files were integrated separately for each detector distance with these masks using *SAINT*, and the data from each detector distance were separately corrected for absorption using *SADABS* (Sheldrick, 2009). These data sets were then combined using *XPREP* (Sheldrick, 2008b).

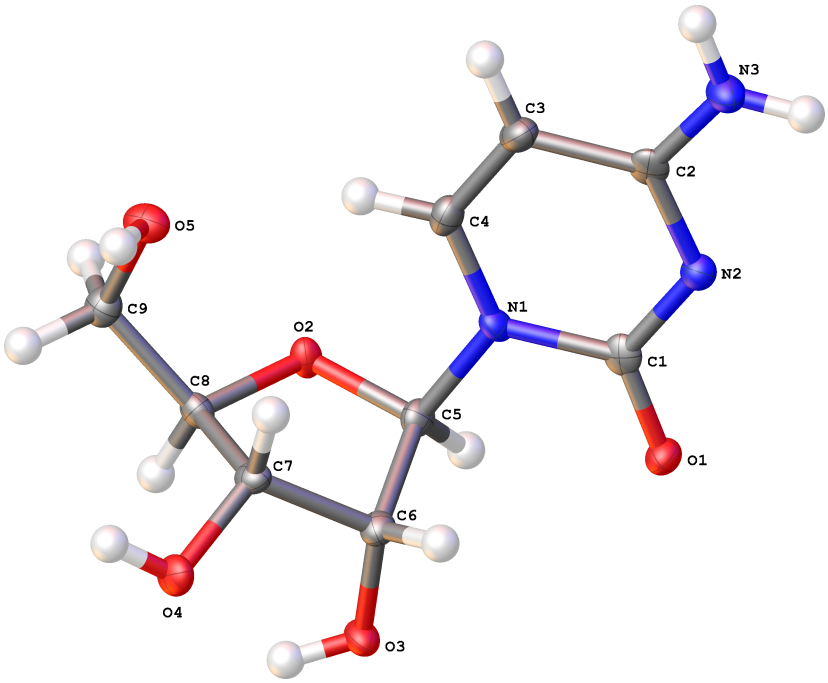

Figure 3.7: The molecular structure of **2** at 2 K, showing atom labels for non-hydrogen atoms. Anisotropic displacement parameters are drawn at the 75% probability level.

Table 3.9: Crystal data and structure refinement for **2** at 2 K

Empirical formula	$C_9H_{13}N_3O_5$
Formula weight (g mol^{-1})	243.22
Temperature (K)	2.0(1)
Crystal system, space group, Z	orthorhombic, $P2_12_12_1$, 4
a (Å)	5.0784(3)
b (Å)	13.9046(10)
c (Å)	14.6992(10)
Volume (Å^3)	1037.96(12)
Calculated density (mg mm^{-3})	1.556
F(000)	512.0
Crystal size (mm^3)	0.26 × 0.1 × 0.05
Crystal shape, colour	needle, clear colourless
Wavelength λ, Mo K_α (Å)	0.71073
Absorption coefficient μ (mm^{-1})	0.128
Absorption correction type	multi-scan
Ratio min/max transmission	0.8445
Maximum 2θ (°)	59.08
No. of measured reflections	9630
No. of unique reflections	2456
R_{int}	0.0523
R_1, wR_2	0.0457, 0.0822
Data/restraints/parameters	2456/0/157
Goodness-of-fit on F^2	1.029
Largest diff. peak/hole (e Å^{-3})	0.290/−0.244

The structure solution was performed with *SHELXS* and the least-squares refinement was performed with *SHELXL* (Sheldrick, 2008a), running within *Olex2* (Dolomanov *et al.*, 2009). Crystal parameters, refinement statistics and data collection details are given in Table 3.9, and the molecular diagram of the refined structure is shown in Figure 3.7. All hydrogen atoms were located from a difference electron-density Fourier map after four cycles of least-squares refinement. The hydrogen atoms were refined as riding atoms using a value of U_{iso} for the hydrogen that is 1.5 times larger than U_{eq} for a host oxygen, and 1.2 times larger than U_{eq} for all other host atom types.

The structure shows no significant changes from the structure measured at 100 K. The unit cell shows a very small decrease of 0.2%, and all bond lengths remain the same within error except for N1–C1 which is observed to increase by a barely significant 0.014(4) Å. The most significant change is in the change in the anisotropic displacement parameters, with the U_{eq} decreasing by 31% on average between 100 K and 2 K.

3.6 Conclusions

Collecting X-ray data at ultra low temperatures presents some challenges over and above those experienced at the more routine low temperatures. In particular, the requirement for the sample to be kept under vacuum and shielded from ambient radiation necessitates shrouds made from a material such as beryllium. These shrouds contribute to the recorded diffraction pattern and interfere with the ability of the integration program to extract some reflection intensities accurately.

A new method has been demonstrated to improve this situation by collecting data at multiple detector distances, thus allowing otherwise-affected reflections to be measured without interference from non-sample scattering. This method is further improved by the use of masks during the integration program, to ensure that the intensities from those reflections which are most affected by scattering from the shrouds, are discarded.

In order to generate these masks, a program, *Masquerade*, has been written, and the process by which masks are created from the known scattering pattern of the shroud material and the position of the shroud has been described, including the means to measure the offsets of the shrouds from the centre of the crystal. This technique could conceivably have other uses, for instance in absorption correction calculations (*e.g.* Albertsson *et al.*, 1979; Coppens *et al.*, 1974), since the path of each diffracted beam from the sample through the shroud material could be calculated using similar methodology.

While the technique has been applied to Bruker reflection images, the calculations are universal. With knowledge of the image format and geometry conventions used by other manufacturers, they could be easily applied to any other diffractometer.

The combination of collecting data at multiple detector distances and integrating the resulting frames with masks has been shown to give a clear improvement in the quality of data that can be measured from samples cooled to very low temperatures using CCRs with beryllium vacuum shrouds.

Chapter 4

Superconducting Charge-Transfer Salts

4.1 Introduction

The idea that a material with metallic properties could be constructed from non-metallic elements was first proposed over a century ago by McCoy & Moore (1911). This idea was expanded upon in the mid 1960s when the then recent Bardeen-Cooper-Schrieffer (BCS) theory of superconductivity (Bardeen *et al.*, 1957) was applied to organic materials and it was proposed that suitably constructed systems might show superconductivity even far above room temperature (Little, 1964; Little, 1965). This theory gained a great deal of interest as these materials were made up of molecular units, providing the possibility that the conductive properties could be adjusted by synthetic modifications to the molecules involved.

One highly active area of research is that of charge-transfer (CT) materials, featuring donor and acceptor molecules. Two of the more successful donors and acceptors were discovered in the 1960s: the acceptor TCNQ (tetracyanoquinodimethane; Acker *et al.*, 1960) was discovered first, followed by the donor TTF (tetrathiafulvalene; Coffen & Garrett, 1969). Separately these molecules were used in a range of relatively highly-conducting complexes before being combined in 1973 to form the first stable organic metal, TTF · TCNQ (Ferraris *et al.*, 1973).

Research continued into these materials and their properties, and in 1979, the first organic crystalline superconductor was found: $(TMTSF)_2PF_6$, where TMTSF is tetramethyltetraselenafulvalene, a similar molecule to TTF (Jérome *et al.*, 1980). When under a pressure of 12 kbar the complex becomes superconducting at 0.9 K. Materials of this type, known as the Bechgaard salts, were investigated with a variety of other inorganic ions, including

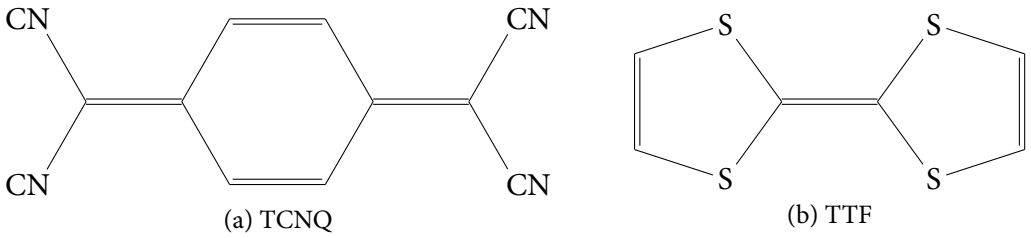

(a) TCNQ (b) TTF

Figure 4.1: The molecular structures of TCNQ and TTF.

the tetrahedral ClO_4^- ion. When cooled slowly, the $(TMTSF)_2ClO_4$ complex undergoes an order-disorder transition at 24 K below which the ClO_4^- ion is ordered and subsequently becomes superconducting at ambient pressure at 1.4 K, making it the first ambient pressure organic superconductor to be discovered (Bechgaard *et al.*, 1981).

An alternative modification of the TTF donor molecule led to the development of BEDT-TTF (bis(ethylenedithio)-tetrathiafulvalene), which when combined with the TCNQ acceptor was found to exhibit higher conductivity than the original TTF · TCNQ salt (Mizuno *et al.*, 1978). Interest in this molecule, due to the larger intermolecular interactions resulting from the increased number of chalcogenide atoms compared to TMTSF, resulted in the discovery of superconductivity in $(BEDT{-}TTF)_4(ReO_4)_2$ at 2 K under a pressure of 4 kbar (Parkin *et al.*, 1983).

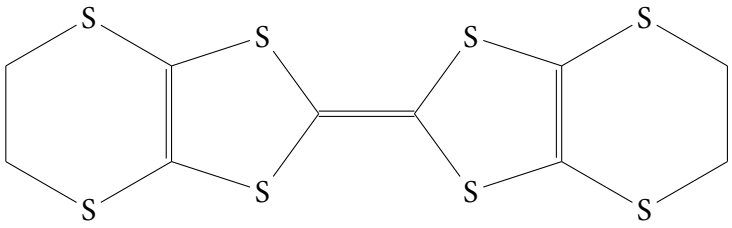

Figure 4.2: The molecular structure of BEDT-TTF.

Since this discovery a huge range of BEDT-TTF salts have been shown to exhibit superconductivity at a range of temperatures and pressures, with one of the highest reported superconducting transition temperatures, T_c, exhibited by β'-$(BEDT{-}TTF)_2ICl_2$ at 14.2 K under a pressure of 86 kbar (Taniguchi *et al.*, 2003). Many more examples can be found in a review by Mori (2006).

4.1.1 BEDT-TTF Salts Containing Tris(oxalato)metallate(III) Anions

A family of BEDT-TTF salts, all containing tris(oxalato)metallate(III), have been found to show a range of conducting properties including superconductivity at low temperatures. The first to be discovered, β''–$(BEDT{-}TTF)_4[(H_3O)Fe(C_2O_4)_3]PhCN$, was also the first

molecular superconductor containing paramagnetic metal ions (Graham *et al.*, 1995). The superconducting T_c was 8.5 K, above which the material displayed metallic conductivity.

The crystal packing of this material shows layers of BEDT-TTF cations separated by an anion layer containing $Ga(Ox)_3$ in a hexagonal honeycomb pattern linked by H_3O^+, with PhCN as a guest molecule in the cavities (Kurmoo *et al.*, 1995). Since this discovery many similar compounds have been synthesised by changing the transition metal and also the guest molecule. Reports of salts containing Cr, Al and Co have been published, with the Cr complex containing H_3O^+ also showing superconductivity at 5.5 K (Martin *et al.*, 1997). Complexes with the other metals or with NH_4^+ in place of H_3O^+ showed different packing behaviour and were found to be semiconductors (Martin *et al.*, 2001).

Complexes in which the guest molecule was exchanged for nitrobenzene, $PhNO_2$, have also been found to show superconductivity. β''–$(BEDT–TTF)_4[(H_3O)Fe(C_2O_4)_3]PhNO_2$ was first reported to show semiconducting behaviour from 20 K to 300 K by Sun *et al.* (1998). This complex was subsequently reported to undergo a superconducting transition at 6.2 K, with an isostructural complex containing Cr also showing superconductivity at 5.8 K (Rashid *et al.*, 2001).

The main complex studied in this chapter, β''–$(BEDT–TTF)_4[(H_3O)Ga(C_2O_4)_3]PhNO_2$ (**3a**), displays metallic conductivity at room temperature, with the resistance decreasing with temperature as is expected for metallic materials. At 160 K the complex undergoes a metal-semiconductor transition and the resistance then increases as the temperature is reduced, with a shoulder at 20 K, below which the resistance increases sharply until 7.5 K, at which point the material abruptly undergoes a transition to a superconducting state (Akutsu *et al.*, 2002; Akutsu *et al.*, 2003).

This is an unusual behaviour for molecular superconductors as many undergo a transition to a superconducting state from a metallic state rather than a semiconducting state. For this reason, it was decided to study the structure above and below the superconducting transition by SXRD in the hope of better understanding the structure-property relationship for this material, and the ultra low temperatures required for this study were one of the original driving forces behind the development of the Xiphos. Two related iron(III) complexes that also show superconductivity, β''–$(BEDT–TTF)_4[(H_3O)Fe(C_2O_4)_3]PhNO_2$ (**3b**) and β''–$(BEDT–TTF)_4[(H_3O)Fe(C_2O_4)_3]PhCN$ (**3c**), were also studied.

4.2 $\beta''-(BEDT-TTF)_4[(H_3O)Ga(C_2O_4)_3]PhNO_2$

4.2.1 Experimental

Diffraction experiments were performed with two different crystals, at temperatures between 160 K and 2 K. The first crystal to be selected was crystallised in 2001 at the University of Hyogo, Japan by Dr Hiroki Akutsu. The crystals form very dark red needles which are opaque when viewed through an optical microscope, so several were screened at room temperature on a three circle Bruker SMART 1K diffractometer before one was selected for diffraction on the Xiphos.

Once the crystal was mounted, following the procedure described in Chapter 2, it was cooled from room temperature to 2 K at 1 K min^{-1}. Full data collections were performed at 2 K, 3 K, 4 K, 5 K, 10 K, 20 K, 40 K, 60 K, 80 K, 120 K and 160 K. The rate of warming between each temperature was 1 K min^{-1}, with the exception of the temperature range 5 K to 10 K where the crystal was warmed at 0.5 K min^{-1} through the superconducting phase transition.

A full hemisphere of data could not be collected given the orientation of the crystal, so it was carefully removed from the graphite fibre and re-mounted at approximately 90° from the previous mounting point. Data were collected at the same eleven temperatures, with the same rate of temperature change as in the first crystal orientation. When the data were combined the coverage of reciprocal space was 98% complete to 53° in 2θ for space group $P\bar{1}$.

A second batch of crystals were synthesised by Dr Akutsu in 2011 and from this batch one crystal was selected for diffraction experiments on the Xiphos. Data were collected at 2 K, 10 K and 160 K, before the crystal was removed from the mount and reattached in a different orientation as before, at which point the data collections were repeated to give a completeness of 94% to 53° in 2θ for space group $P\bar{1}$.

The first crystal was sent to Dr Akutsu in Japan to test the superconducting properties directly. The crystal was found to exhibit superconductivity below 7 K, as expected. The second crystal had already been tested before it arrived in Durham and it too was shown to exhibit superconductivity below 7 K.

4.2.2 Results and Discussion

At 160 K this crystal has space group symmetry $C2/c$ with a structure comprised of alternating layers, one containing the BEDT-TTF molecules and the other consisting of a honeycomb structure of gallium oxalate linked by H_3O^+, with $PhNO_2$ molecules in the cavities within the honeycomb structure. The layers stack along the crystal *c* axis, with the oxalate layer lying in the *ab* plane, shown in Figure 4.3.

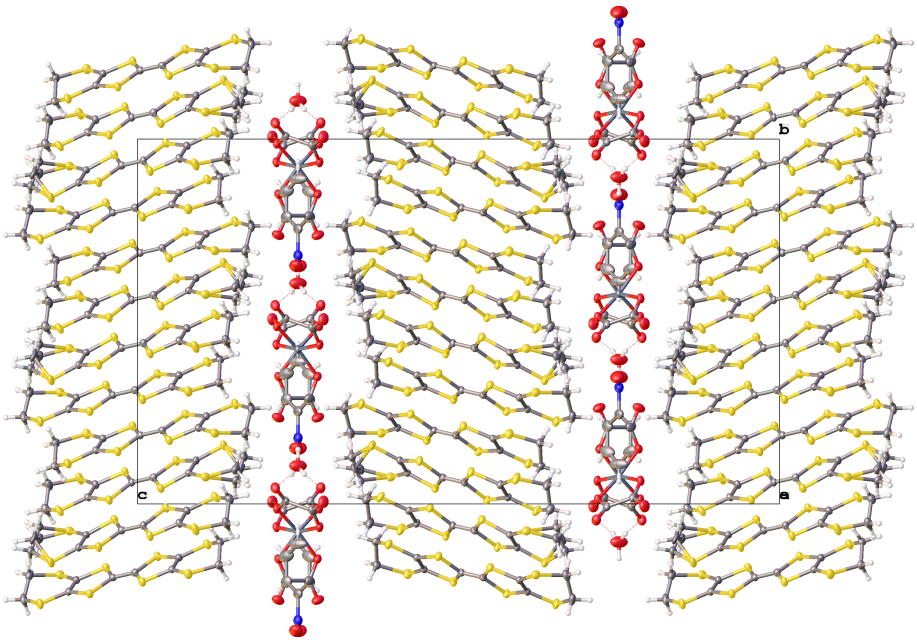

Figure 4.3: The crystal packing of **3a** at 160 K, perpendicular to the *a* axis. Anisotropic displacement parameters are shown at a probability of 50%.

There are two crystallographically independent BEDT-TTF molecules in the asymmetric unit that pack parallel to each other at an angle of approximately 30° from the *c*-axis. The terminal ethylene group is disordered on one of these BEDT-TTF molecules, as is commonly seen in structures of these materials. The asymmetric unit also contains half of each of a gallium oxalate, H_3O^+, and $PhNO_2$ molecule, shown below in Figure 4.4.

As the temperature is lowered, uncertainty about the space group assignment grows as is described below. As a result the data were processed in two space groups: $C2/c$ and $P\bar{1}$. Structures were solved and refined in both space groups at all temperatures and the tables of structure refinement data can be found in Appendix 2.

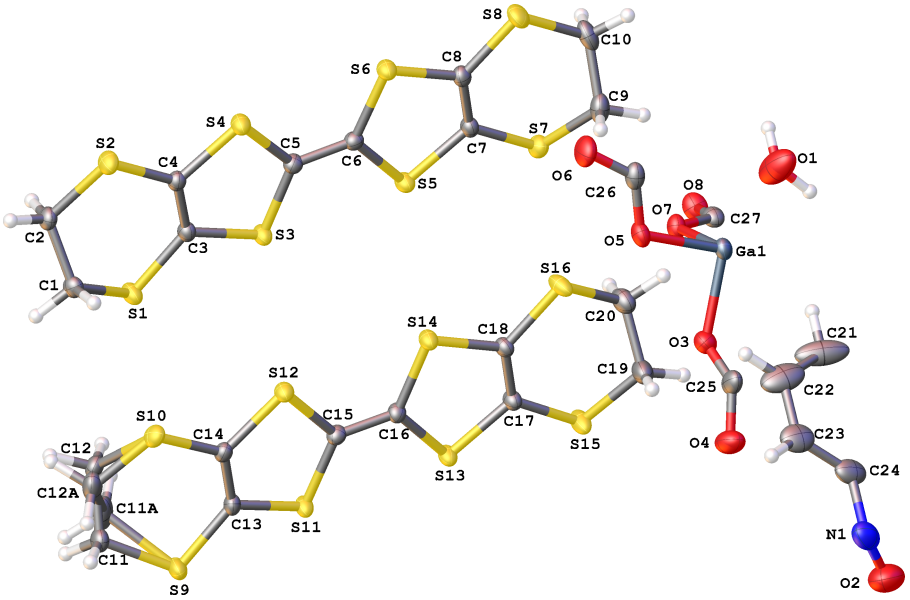

Figure 4.4: The asymmetric unit of **3a** at 160 K. Anisotropic displacement parameters are shown at a probability of 50%.

4.2.2.1 Space Group Setting

The space group adopted by β″–(BEDT–TTF)$_4$[(H$_3$O)Ga(C$_2$O$_4$)$_3$]PhNO$_2$ at room temperature is $C2/c$. However, as the temperature is lowered, this space group assignment becomes less certain. Increasingly violations of the *c*-glide systematic absence conditions ($h0l$, where l is odd) are observed, as shown in Table 4.1. At 160 K there are a small number of these violations but the mean intensity of these reflections is very low. By 60 K more than a quarter of the reflections which should be absent are observed at a level of $I > 4\sigma(I)$ and this increases to nearly 50% at 4 K.

With the removal of the *c*-glide symmetry the space group would drop to $C2$, but since a centre of inversion is still observed, the space group drops further to $P\bar{1}$. However, based on the evidence of the systematic absence violations there does not appear to be a single point at which the space group changes. This suggests a gradual change, such as a freezing of disorder which gives rise to a change in the average structure at lower temperatures. The structure may be solved and refined without particular difficulty in either space group at all temperatures and the majority of the structure appears to retain the higher symmetry except for some disorder in the PhNO$_2$ group and an oxalate ligand, which is discussed below.

Table 4.1: The number of *c*-glide systematic absence violations as a function of temperature. The mean I and $I/\sigma(I)$ values are measured for the total number of reflections which should be systematically absent given a *c*-glide symmetry operation.

(a) Crystal 1

Temperature (K)	Total	$I > 2\sigma(I)$	$I > 3\sigma(I)$	$I > 4\sigma(I)$	$\langle I \rangle$	$\langle I/\sigma(I) \rangle$
2	762	532	428	346	7.93	4.31
3	765	516	425	363	8.00	4.35
4	765	514	427	346	8.10	4.25
5	765	514	401	332	7.79	4.14
10	764	509	421	337	7.73	4.11
20	763	476	379	303	6.98	3.65
40	759	412	312	231	4.66	2.69
60	754	324	228	159	2.91	1.90
80	761	271	135	65	1.89	1.26
120	758	179	73	21	1.28	0.78
160	770	95	33	9	0.91	0.43

(b) Crystal 2

Temperature (K)	Total	$I > 2\sigma(I)$	$I > 3\sigma(I)$	$I > 4\sigma(I)$	$\langle I \rangle$	$\langle I/\sigma(I) \rangle$
2	1144	544	383	260	0.97	2.42
10	1078	547	405	282	0.91	2.71
160	997	102	31	3	0.09	0.25

4.2.2.2 Unit Cell Parameters

The unit cell only shrinks by ~ 0.1% from 160 K to 2 K, with the biggest contraction in the longest axis, *c*. This is the axis perpendicular to the BEDT-TTF and oxalate layers. As shown in Table 4.2, the contraction observed is very similar in both crystals and in both of the space groups considered.

Table 4.2: Changes in the unit cell parameters **3a** in both space group settings between 160 K and 2 K.

	Monoclinic		Triclinic	
	Crystal 1	Crystal 2	Crystal 1	Crystal 2
Δa (Å)	0.0192(4)	0.0314(8)	0.0197(4)	0.0310(8)
Δb (Å)	0.0904(7)	0.1003(14)	0.0420(4)	0.0523(8)
Δc (Å)	0.1968(13)	0.1980(20)	0.1950(12)	0.1980(20)

The change in unit cell volume is not linear with temperature, as shown in Figure 4.5. The change is linear from 160 K to 80 K, at which point the rate of volume change becomes

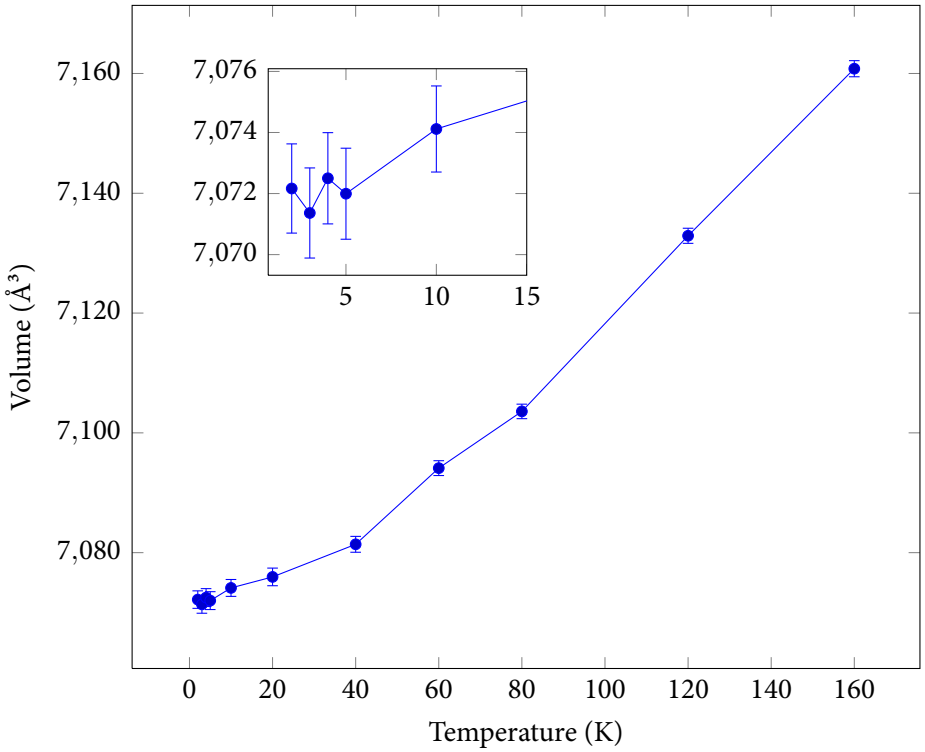

Figure 4.5: The variation of unit cell volume in **3a** (crystal 1) with temperature.

smaller as the temperature is reduced. There is a small reduction in volume through the superconducting transition between 10 K and 5 K, although it is not significant within 3σ, and below 5 K there is no significant change.

4.2.2.3 Charge Separation

The central C–C and C–S bonds of the BEDT-TTF molecule have been shown to be sensitive to the partial charge supported by the molecule and a method has been proposed to calculate this charge from experimentally determined bond lengths (Guionneau *et al.*, 1997). An initial method used only the central C=C double bond but the revised approach uses the average values of four central bond lengths, as shown in Figure 4.6. The charge on a molecule, Q, is given by Equation 4.1.

$$Q = 6.374 - 7.463\delta \quad \text{where} \quad \delta = (b + c) - (a + d) \tag{4.1}$$

This calculation has been applied to the structural data measured using the Xiphos. As the disorder leading to the change in symmetry at low temperatures is primarily observed in the oxalate layer while the BEDT-TTF molecules are unchanged, the calculations are

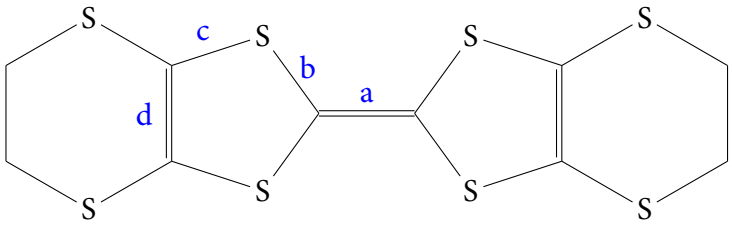

Figure 4.6: A diagram of the BEDT-TTF molecule, showing the four bonds used in Equation 4.1 with their chemical equivalents in the analysis of the partial charge of the system.

presented for the molecular structures of crystal 1 which were refined in $C2/c$ at all temperatures. The graphs obtained from the refinements in $P\bar{1}$ and those from crystal 2 are all similar however. The data points are each normalised so that the total charge for the two BEDT-TTF molecules is 1.0 at all the temperatures measured. To show the changes at the lowest temperatures more clearly, the data are presented on a logarithmic scale in Figure 4.7.

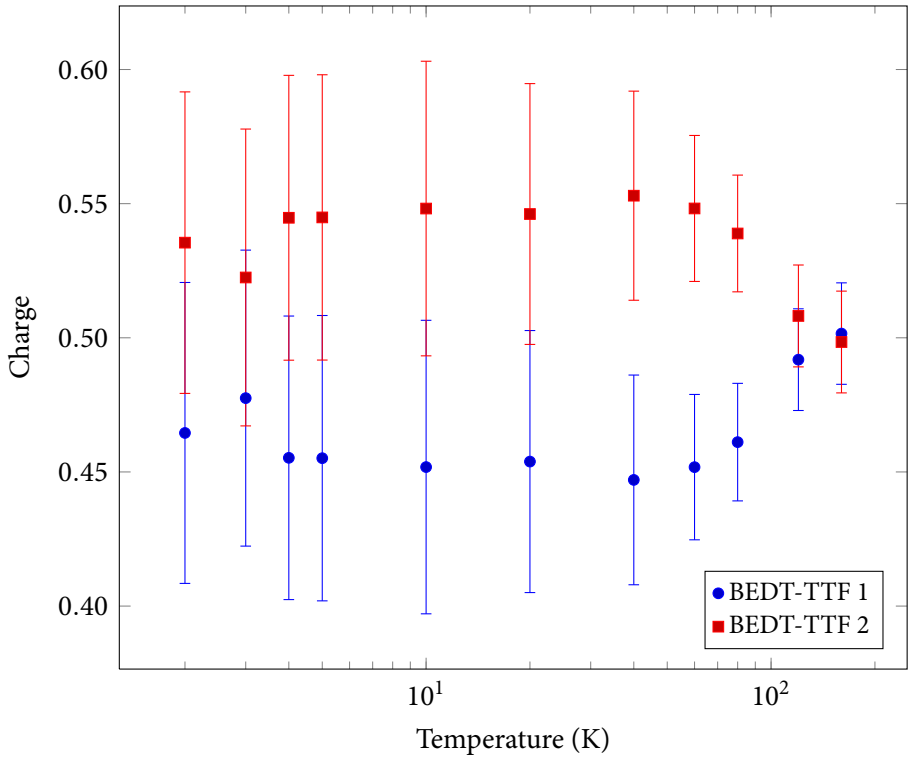

Figure 4.7: Partial charges for each of the independent BEDT-TTF molecules in the asymmetric unit of **3a** when data are refined with space group $C2/c$. The data points at each temperature have been normalised so that the total charge for the two BEDT-TTF molecules is 1.0.

The error bars are calculated from the standard uncertainties of the bond lengths used in the calculation of Q. At low temperatures the disorder in the structure leads to a higher R_1 factor (see the refinement data in Appendix 2), and consequently the bond length uncertainties increase. As a result, the errors in the charges also increase.

The charges are approximately equal at 160 K, at which temperature the material is in the metallic phase. Below this temperature there is a transition to a semiconducting phase, and the charges on the BEDT-TTF molecules differ and separate. This trend appears to continue down to 2 K with the charges remaining unequal but due to the size of the errors involved this can not be stated with certainty.

4.2.2.4 Structure Disorder

The terminal ethylene group of one of the BEDT-TTF groups is disordered in $C2/c$ at the site closest to nitro group of the $PhNO_2$ molecule. At 160 K the minority occupancy is ~ 26% when modelled in $C2/c$, with a very similar average value for the two disordered BEDT-TTF molecules in $P\bar{1}$. As the temperature is lowered the disordered fraction gradually reduces. By 60 K it is ~ 9% and it reduces to ~ 7% by 10 K, giving the carbon atoms smaller electron densities than the largest Fourier ripples around the Ga atom, again regardless of which space group is used.

The thermal ellipsoids of the nitrobenzene molecule, which sits on a two-fold rotation axis in the space group $C2/c$, become more elongated as the temperature lowers and the thermal motion is reduced. By 40 K this effect is significant enough to model the $PhNO_2$ molecule as disordered over two positions, with a percentage occupancy split of approximately 60:40. This occupancy ratio changes slightly to 58:42 at 10 K and 57:43 at 2 K. Diagrams of the anion layer are shown in Figure 4.8.

As the split is not equal across the two-fold axis in $C2/c$, this may explain the systematic absence violations described above. If the molecule is disordered at all temperatures but the thermal motion is enough to cover both sites, the average structure may be symmetric about that position. At lower temperatures the thermal motion is reduced and the static disorder becomes clear, breaking the symmetry of the average structure. This may also explain why the symmetry is not broken suddenly, but gradually over a wide range of temperatures as seen in Table 4.1.

The thermal ellipsoids are also elongated in the H_3O^+ molecules and the oxalate groups adjacent to the disordered benzene ring along the b axis, but not to a large enough extent to successfully model over two positions. This suggests that the change in position of the guest molecule also affects the oxalate honeycomb.

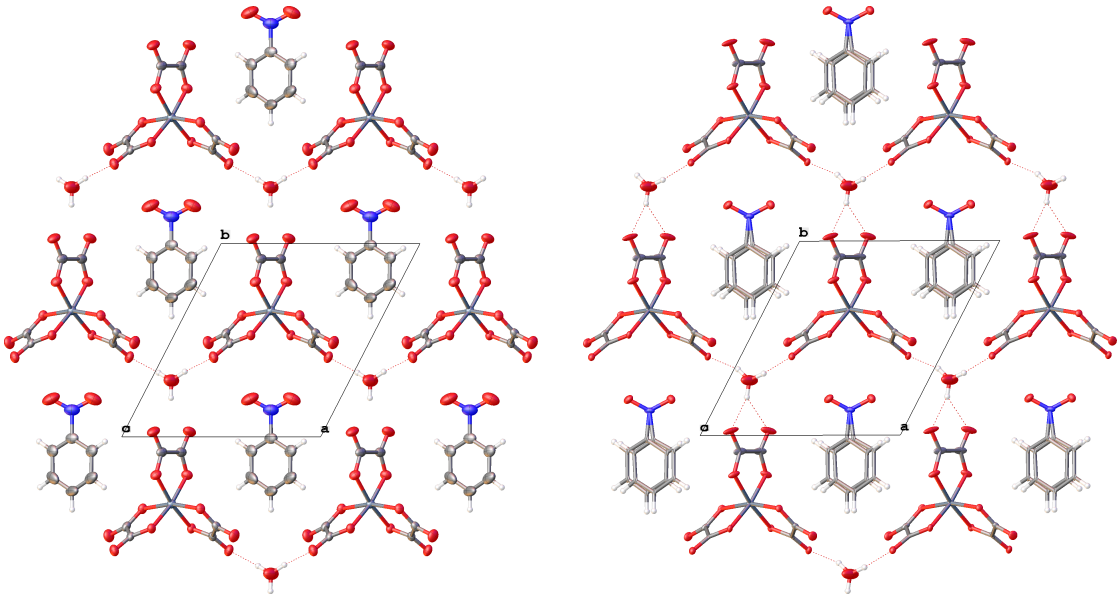

(a) 160 K (b) 2 K

Figure 4.8: The oxalate anion layer in **3a**, showing the honeycomb packing arrangement, and the disorder in the $PhNO_2$ guest molecule at low temperatures (2 K) compared to 160 K.

4.2.2.5 Rotation of the Nitro Group in Nitrobenzene

The nitrobenzene guest molecule is not entirely planar within the oxalate cavity. The nitro group is rotated from the benzene ring by 36.67˚ at 160 K, and this rises to 40.0(5)˚ at 2 K. This value is the same within error for both the disordered benzene rings at 2 K. The plane of the benzene ring is rotated with respect to the plane formed by the Ga atoms in the anion layer by 31.39(8)˚ at 160 K and 31.4(3)˚ at 2 K, meaning that the rotation of the benzene ring is fixed while the nitro group rotates.

A previous study found that the rotation of the nitro group relative to the benzene ring was near linear with respect to temperature from 300 K to 100 K, with deviations from this trend at 30 K and 12 K (Probert, 2005). Using the new data from the XIPHOS, this rotation in the low temperature regime can be described more clearly. The relationship is linear down to 60 K but by 40 K the rotation of the nitro group stops and the torsion angle between it and the benzene ring remains the same within error to 2 K. The relationship between the rotation angles and temperature is shown in Figure 4.9.

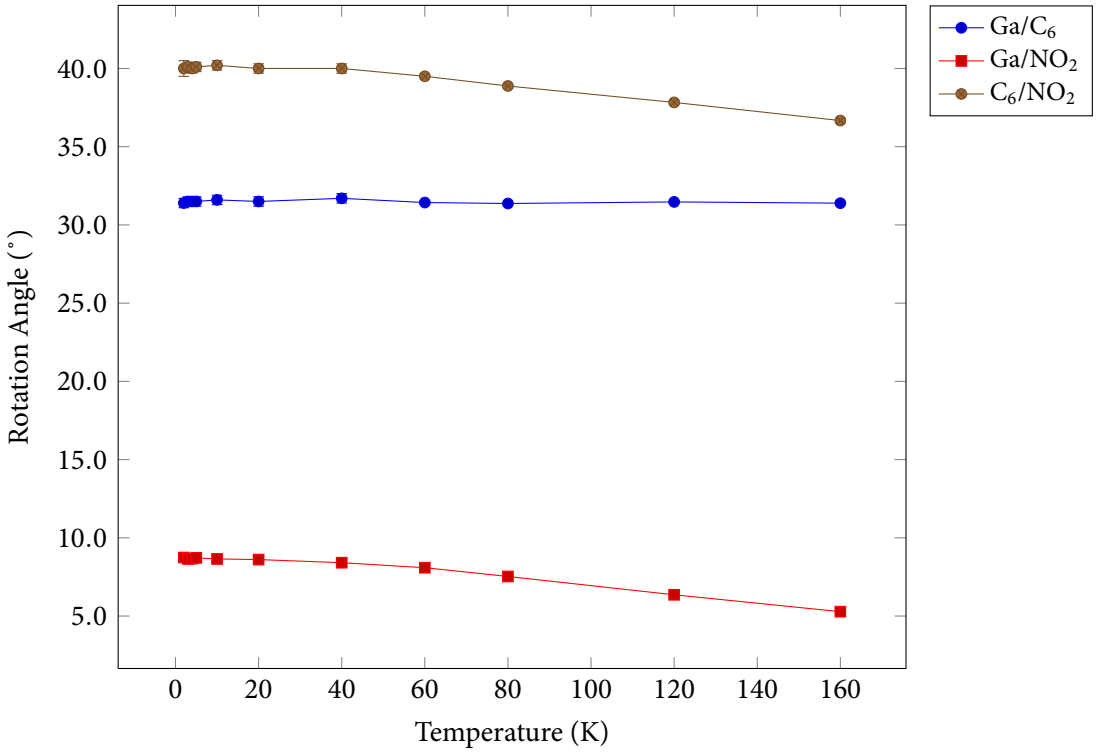

Figure 4.9: The rotation of the nitrobenzene molecule with temperature. In the key, C_6 refers to the benzene ring of the nitrobenzene, NO_2 refers to the nitro group of the same molecule and Ga refers to the plane formed by the three Ga atoms surrounding the nitrobenzene molecule.

4.2.2.6 Summary

Complex **3a** demonstrates complex structural behaviour at low temperatures. No major changes are observed in the unit cell parameters, but violations of the space group symmetry that is assigned at room temperature are increasingly observed as the temperature is reduced. The nitro group of the nitrobenzene guest molecule is also observed to rotate as the temperature is reduced, although this rate of change in the rotation angle slows and eventually reaches a plateau at the lowest temperatures measured.

What effect these structural changes have, if any, on the superconducting properties of the material are not clearly understood. Further analysis of the structural data are ongoing, but pass beyond the scope of this thesis.

4.3 β″–(BEDT–TTF)$_4$[(H$_3$O)Fe(C$_2$O$_4$)$_3$]PhNO$_2$

A single crystal of the related iron β″–(BEDT–TTF)$_4$[(H$_3$O)Fe(C$_2$O$_4$)$_3$]PhNO$_2$ (**3b**), synthesised by Dr Akutsu, was selected and mounted on a graphite fibre as described in Chapter 2 and cooled directly to 2 K at 1 K min^{-1}. Due to time constraints, the data were collected at 2 K only and the crystal was not re-mounted on the fibre to collect more data. As a result the data were ~ 80% complete to 53° in 2θ when refined in space group $P\bar{1}$ and so in this structure only the Fe and S atoms were modelled with anisotropic displacement parameters. An image of the asymmetric unit of **3b** in space group $P\bar{1}$ is shown in Figure 4.10 and the refinement details are given in Table 4.3.

The crystal structure of **3b** is very similar to that of **3a**, including the disorder in the position of the PhNO$_2$ molecule and subsequent breaking of the *c*-glide symmetry. Of a total of 824 reflections with indices *h*0*l* where l is odd, 333 are observed with an intensity I larger than $4\sigma(I)$. The average $I/\sigma(I)$ of the 824 reflections is 3.95, which strongly suggests that the violations are not artefacts of the data collection process but are due to structural features of the crystal.

The extension of the thermal displacement parameters in one direction in the oxalate closest to the NO$_2$ group was also more pronounced in this structure compared to **3a** at 2 K and as a result the group was modelled over two positions. The disorder in the terminal ethylene group of half the BEDT-TTF molecules in the asymmetric unit was also slightly more pronounced, with occupancy values for the minor component refining to ~ 9.5%.

The rotation of the nitro group with respect to the benzene ring in the PhNO$_2$ guest molecule is very similar to that found in **3a** at 2 K, with a value of 39.9(4)° for the structure refined in $C2/c$ and values of 39.3(10)° and 42.0(15)° for the two disordered parts when refined in $P\bar{1}$.

Both this salt and **3a** are isostructural and undergo superconducting transitions at similar temperatures: 7.5 K for **3a** (Akutsu *et al.*, 2002) and 6.2 K for **3b** (Rashid *et al.*, 2001). No major differences are noticed between the structures of each at 2 K and the same disorder in the oxalate layer is observed in addition to the violations of the *c*-glide symmetry in both structures.

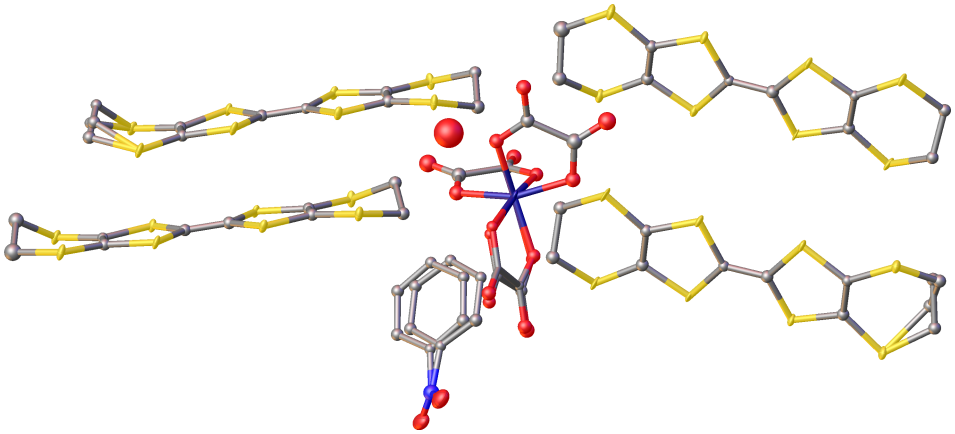

Figure 4.10: The asymmetric unit of **3b** at 2 K. Thermal displacement parameters are shown at a probability of 75%, and hydrogen atoms have been omitted for clarity.

Table 4.3: Crystal data and structure refinement of **3b** at 2 K.

Empirical formula	$C_{52}H_{40}FeNO_{15}S_{32}$
Formula weight (g mol^{-1})	2000.62
Temperature (K)	2.0(1)
Crystal system, space group, Z	triclinic, $P\bar{1}$, 2
a (Å)	10.2538(6)
b (Å)	11.1786(8)
c (Å)	34.859(2)
α (°)	88.447(3)
β (°)	86.826(2)
γ (°)	62.735(2)
Volume (Å^3)	3546.3(4)
Calculated density (mg mm^{-3})	1.874
F(000)	2034
Crystal size (mm^3)	0.6 × 0.15 × 0.13
Crystal shape, colour	needle, black
Wavelength λ, Mo K_α (Å)	0.71073
Absorption coefficient μ (mm^{-1})	1.221
Absorption correction type	multi-scan
Ratio min/max transmission	0.8717
Maximum 2θ (°)	52.78
No. of measured reflections	37897
No. of unique reflections	11747
R_{int}	0.0227
R_1, wR_2	0.0740, 0.1605
Data/restraints/parameters	11747/8/634
Goodness-of-fit on F^2	1.350
Largest diff. peak/hole (e Å^{-3})	1.068/−1.218

4.4 β″−(BEDT−TTF)$_4$[(H$_3$O)Fe(C$_2$O$_4$)$_3$]PhCN

A third material, β″−(BEDT−TTF)$_4$[(H$_3$O)Fe(C$_2$O$_4$)$_3$]PhCN (**3c**), was prepared by Dr Akutsu. The crystals of this material were tested by Dr Akutsu and were found not to show superconductivity, although this phenomenon has been observed in other crystals of the same material at 8.5 K (Martin *et al.*, 2001). Diffraction data were measured at 120 K on a Bruker SMART 6K diffractometer, utilising a standard nitrogen-gas cryostat. An image of the asymmetric unit is shown in Figure 4.11 and the refinement parameters are shown in Table 4.4.

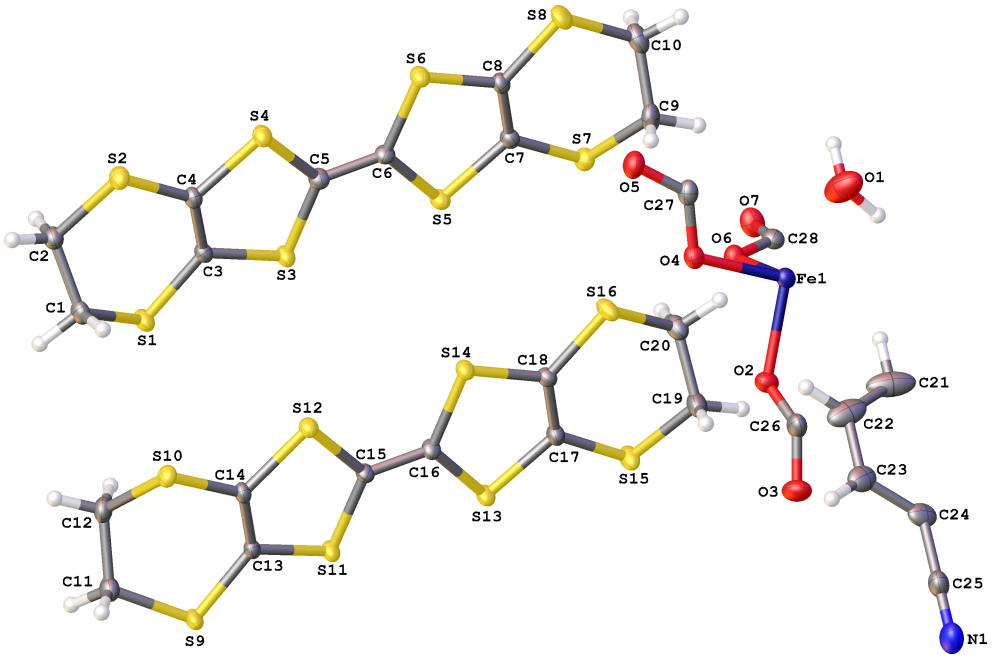

Figure 4.11: The asymmetric unit of **3c** at 120 K. Thermal displacement parameters are shown at a probability of 50%.

The structure is very similar to the structures of the other two complexes measured, although no disorder is seen in the terminal ethylene groups at 120 K. The PhCN molecule occupies the same position as the PhNO$_2$ molecule within the oxalate honeycomb and the thermal ellipsoids in the benzene ring are elongated, particularly for atom C21 in the position *para* to the cyano group, in the same fashion as those of the PhNO$_2$ molecule in the other crystals.

At 120 K the space group can be assigned to $C2/c$ as there are very few violations of the c-glide symmetry. Of a total of 625 reflections with indices $h0l$ where l is odd, only 3 are observed with an intensity I larger than $4\sigma(I)$. The average $I/\sigma(I)$ of these reflections is 0.34. However the similar elongations in the displacement parameters of the cyanobenzene atoms to those of the nitrobenzene in **3a** at 120 K suggest that this structure may also exhibit

the same disorder as the previous structures if cooled to lower temperatures. Further work is ongoing to determine the structure at lower temperatures with the XIPHOS.

Table 4.4: Crystal data and structure refinement of **3c** at 120 K.

Empirical formula	$C_{53}H_{40}FeNO_{14}S_{32}$
Formula weight (g mol^{-1})	1996.63
Temperature (K)	120(1)
Crystal system, space group, Z	monoclinic, $C2/c$, 4
a (Å)	10.2210(4)
b (Å)	19.9604(7)
c (Å)	34.8661(14)
β (°)	93.4000(10)
Volume (Å^3)	7100.7(5)
Calculated density (mg mm^{-3})	1.868
F(000)	4060
Crystal size (mm^3)	0.65 × 0.17 × 0.15
Crystal shape, colour	needle, black
Wavelength λ, Mo K_α (Å)	0.71073
Absorption coefficient μ (mm^{-1})	1.218
Absorption correction type	multi-scan
Ratio min/max transmission	0.7675
Maximum 2θ (°)	52.84
No. of measured reflections	36034
No. of unique reflections	7268
R_{int}	0.0337
R_1, wR_2	0.0336, 0.0786
Data/restraints/parameters	7268/3/458
Goodness-of-fit on F^2	1.048
Largest diff. peak/hole (e Å^{-3})	0.665/−0.467

4.5 Conclusions

Data have been collected on three related charge-transfer complexes at various temperatures. Two of the complexes show superconducting behaviour and crystal structures of these have been determined below their superconducting transition temperature. Both materials show very similar structural features, with disorder of the oxalate anion layer and of the guest $PhNO_2$ molecule at low temperatures. The structure of the third related complex, **3c**, the crystal of which was shown not to exhibit superconductivity, was also determined at 120 K. The structure of this material showed signs of similar strain in the anion layer with thermal displacement parameters elongated in one direction which manifests as disorder in the other complexes at low temperatures.

No abrupt changes were observed in these crystals as the temperature is lowered. A gradual

breaking of symmetry takes place which appears to be a result of static disorder in the anion layers of the materials, masked at higher temperatures by atomic motion. As such, the 'true' space group of these materials may be $P\bar{1}$ at all temperatures rather than the $C2/c$ as is more commonly assigned at higher temperatures.

No structural features have been found which might conclusively show evidence for the mechanism behind the onset of superconductivity, although the bond lengths of the BEDT-TTF molecules suggest that adjacent, non-crystallographically identical molecules may carry slightly different partial charges at low temperatures.

It has been suggested by Dr Probert (Durham University) and Dr Akutsu (University of Hyogo, Japan) that the crystals measured in this study may be composed of domains, some of which show superconductivity and some of which do not. If there is a difference in the three-dimensional structure of the complexes between the domains this theory may explain the disorder in the average structure which has been observed in **3a** and **3b**. One way to determine whether this domain structure is present would be through the use of electron microscopy, where by imaging a slice of a crystal any deviations from the expected pattern of the positions of adjacent molecules could be observed. Since superconductivity is a bulk property of materials (Schwenk *et al.*, 1986), any differences in adjacent unit cells and how these affect the superconducting properties of different crystals may be of use in elucidating the mechanism underlying the superconductivity.

If the uncertainty in the structural models could be resolved, a computational software package such as *CASTEP* (Segall *et al.*, 2002) could be used along with the determined atomic coordinates to calculate the electronic band structure of each of the materials presented here at a variety of temperatures, including above and below the superconducting transitions. Correlations between any changes in the three-dimensional atomic structure and the resulting band structure with the conducting properties could be invaluable in designing new charge-transfer salts which show superconducting properties at higher and more practically useful temperatures.

Chapter 5

Spin Crossover Complexes

5.1 Introduction

A spin crossover is an electronic phenomenon in which a change of spin-multiplicity occurs within a transition metal complex as a result of changes in the sample environment, such as temperature, pressure, or light irradiation. This was first described in an iron(III) complex 80 years ago, followed 30 years later with the the discovery of a spin transition in the iron(II) complex $[Fe(phen)_2(NCS)_2]$ in 1964 (Baker & Bobonich, 1964). This latter discovery provided the spark for a large and active area of research into this phenomenon, which has great potential for use in applications such as memory storage devices or display devices due to the changes in magnetic properties and sometimes colours accompanying the transition (Gütlich *et al.*, 1994; Gütlich *et al.*, 2000).

In an octahedral ligand field the *d* orbitals lose their five-fold degeneracy and split into two sets of orbitals: e_g and t_{2g}. In complexes where the transition metal cation has an electronic configuration of d^4–d^7, there are two possible configurations depending on the strength of the ligand field. Weak-field ligands cause a small octahedral splitting energy, Δ_{oct}, and where this energy gap is smaller than the spin-pairing energy, the e_g set will be filled before electrons are paired, forming a high-spin (HS) state where the spin multiplicity is at its maximum. Strong-field ligands, on the other hand, lead to a large splitting energy, and where this is greater than the spin pairing energy the electrons will pair up in the t_{2g} set before filling the e_g set, forming low-spin (LS) complexes. This is shown in Figure 5.1.

For certain field strengths the energy difference between these states is small and it becomes possible to switch between them. This is known as a spin transition or spin crossover (SCO). This can be triggered by changes in the ambient environment of the material, such

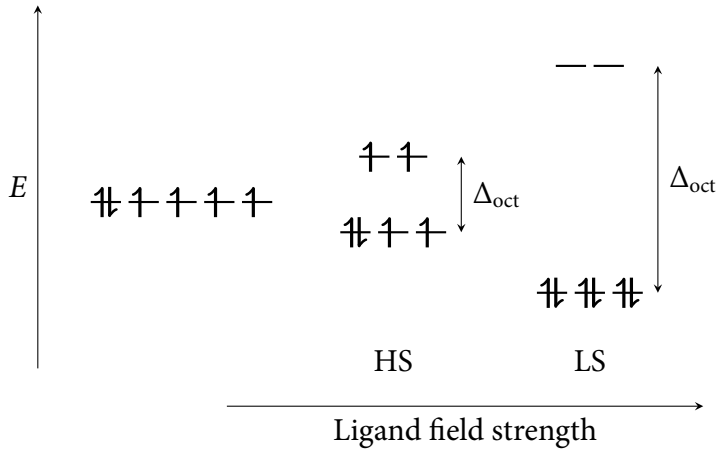

Figure 5.1: Schematic diagram showing the splitting of the *d*-orbitals as a function of the strength of the ligand field for a d^6 complex, with high- and low-spin electron configurations (HS and LS, respectively).

as a change in temperature or pressure. Transitions may also occur as a result of light irradiation at low temperatures, when a LS state may be converted to a meta-stable HS state. This last effect is known as Light Induced Excited Spin State Trapping or LIESST, and was first reported by Decurtins *et al.* (1985).

Any change in the spin-multiplicity of a material will affect its magnetic properties. For example, the common spin transition in iron(II) results in a change from a paramagnetic HS configuration to diamagnetic LS configuration. This can be followed through the use of a magnetometer such as a superconducting quantum interference device, or SQUID.

The e_g orbitals which are occupied in the HS state are anti-bonding in character as opposed to the non-bonding t_{2g} orbitals. The increased population of these orbitals in the HS state compared to the LS state therefore changes the bond strength between the metal and the ligand, which in turn affects the bond lengths between them. For example, in iron(II) complexes Fe–N bond lengths decrease by an average of ~ 0.2 Å as a complex switches from HS to LS. These changes in bond length can be observed with single-crystal diffraction, which together with the wide availability of low temperature cryostats and diamond anvil cells for high-pressure experiments, make this a highly useful tool to study these materials.

Another effect that can be studied by single-crystal diffraction is that of cooperativity, which affects the temperature range over which a spin transition takes place. In the liquid phase the relative populations of molecules in the HS and LS states follow a Boltzmann distribution and hence the transition occurs over a broad temperature range. However in the solid state transitions are often much sharper and occur over a small temperature range. This is thought to be due to intermolecular communication in which a change in spin-state in one molecule may provoke a change in adjacent molecules. Hysteresis, in which the spin

transition occurs at different temperatures on cooling and warming, may also be observed in the solid state, which gives some of these materials a bistability which could be useful in various applications (Gütlich *et al.*, 2000).

The most commonly studied examples of this phenomenon feature iron(II) cations but spin crossover behaviour has been found in complexes with a variety of other metal centres, such as iron(III), cobalt(II), cobalt(III), nickel(II), manganese(III) and chromium(II) (Gütlich *et al.*, 1994). Complexes of other metals which do not have the optimal electron configuration for a spin transition such as zinc(II) have also been studied in order to determine which changes in structure are due to the effect of the transition and which are a result of the change in the temperature or pressure (Sanner *et al.*, 1984).

5.1.1 Complexes with 2,6-di(pyrazol-1-yl)pyridine

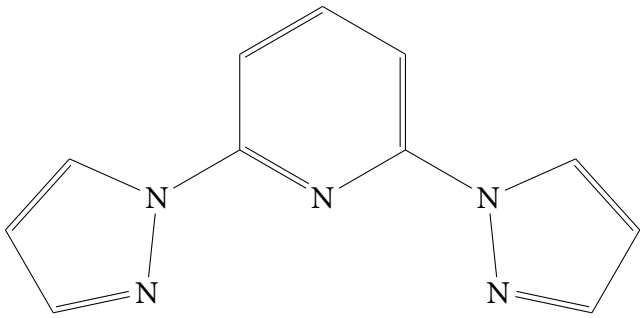

Figure 5.2: The 2,6-di(pyrazol-1-yl)pyridine ligand (L).

The complexes described in this chapter all contain the 2,6-di(pyrazol-1-yl)pyridine ligand (L) shown in Figure 5.2. This ligand is easy to modify systematically and so variants have been used to examine the effect of changing ligand field strength on the characteristics of spin transitions. The iron(II) complex $[FeL_2](BF_4)_2$ has been found to undergo a thermal spin transition centred at 259 K, with a hysteresis width of 3 K (Holland *et al.*, 2001b; Holland *et al.*, 2002).

This study followed an initial report of the copper(II) complex, $[CuL_2](BF_4)_2$, which undergoes an unusual phase transition at 41 K (Leech *et al.*, 1999). The complex is affected by Jahn-Teller distortion, where one axis of the octahedral coordination environment is elongated. Above 41 K the orientation of this elongated axis is not fixed within the crystal, which appears as dynamic disorder in the crystal structure. Below this temperature however, the orientation of the axes become statically ordered within the crystal, leading to a tripling of the monoclinic *b* axis and a corresponding increase in the number of symmetry independent molecules in the unit cell (Solanki *et al.*, 2002).

Further crystallographic studies into $[FeL_2](BF_4)_2$ using a HeliX cryostream found that the complex exhibits the LIESST effect, whereby the LS state can be converted to a new excited HS* state at 30 K by irradiation with red laser light (λ = 632.8 nm) (Money, 2004). As part of the same study the isostructural $[CoL_2](BF_4)_2$ complex (**4a**) was also studied at 120 K and 30 K. This cobalt(II) complex remains in the HS state down to 30 K and no crystallographic phase changes were observed.

Complexes with the same ligands and counter-ions, featuring nickel(II) and zinc(II), have also been studied structurally. $[NiL_2](BF_4)_2$ (**4b**) was studied at 150 K as part of an investigation into how steric effects resulting from modifications of the L ligand would affect the molecular structure of these compounds (Holland *et al.*, 2001a). $[ZnL_2](BF_4)_2$ (**4c**) was studied for comparative purposes as part of the study into $[CuL_2](BF_4)_2$ at intervals of 50 K between 300 K and 100 K (Solanki *et al.*, 2002). No major structural changes were reported within this temperature range.

At room temperature all these compounds, *i.e.* $[ML_2](BF_4)_2$ where M = Fe, Co, Ni, Cu and Zn, are isostructural and crystallise in the monoclinic space group $P2_1$ with similar unit cell parameters: $a \approx b \approx 8.5$ Å, $c \approx 18.5$ Å and $\beta \approx 95^\circ$. There is one metal cation and two BF_4^- counter-ions in the asymmetric unit and Z = 2. The similarity in *a* and *b* cell lengths means that many of the crystals which were examined in the process of this study were twinned by rotation of 90° about the *c* axis and the resulting diffraction pattern was very difficult to interpret. Fortunately untwinned crystals were eventually found for each of the compounds studied.

A variable temperature magnetic susceptibility study of **4a** has been performed by Prof. M. Halcrow (as shown in Figure 5.3) and this indicates a discontinuity below ~ 30 K. A crystallographic study was therefore performed at low temperatures to determine if this anomaly had any structural origin. In order to distinguish any changes which might cause the observed magnetic effects from changes resulting from differences in temperature, the zinc(II) complex **4c** was also studied at low temperatures. Finally, although it was not expected that the nickel(II) complex **4b** would show any changes at low temperatures, no studies had yet been performed and so a study was performed at 2 K to investigate whether any change would be seen.

5.2 Experimental

All compounds studied were synthesised following literature methods by Prof. Malcolm Halcrow at the University of Leeds (Holland *et al.*, 2001a; Solanki *et al.*, 2002).

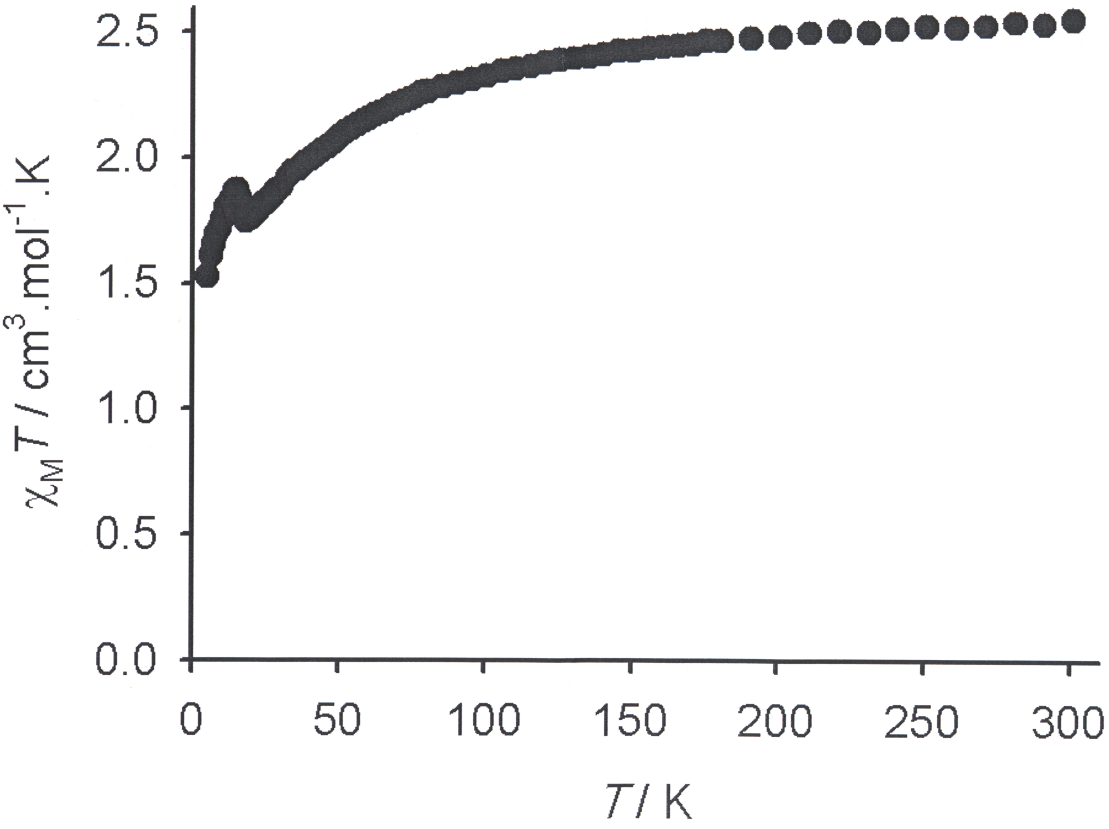

Figure 5.3: Variable temperature magnetic susceptibility curve of **4a**, $[CoL_2](BF_4)_2$, showing an anomaly below 30 K. Image courtesy of Prof. M. Halcrow, University of Leeds.

Suitable crystals of each of the compounds studied were first selected through the use of a polarising microscope. As a large number of the crystals present were twinned, each crystal was then mounted on a glass fibre and a short series of ω scans were collected on the SMART 6K at 120 K. If the diffraction pattern exhibited the expected unit cell and no twinning was observed, a full data collection was then performed at 120 K to determine the quality of diffraction data which could be obtained from the crystal. Once high quality untwinned crystals were found, data were collected with the Xiphos as described in Chapter 2. Two beryllium shrouds were used to create the vacuum required with all the crystals studied.

Diffraction data from $[CoL_2](BF_4)_2$ (**4a**) were measured at 50 K, 20 K, 10 K and 2 K. The crystal was initially cooled from room temperature to 50 K at 1 K min^{-1} and the same cooling rate was used between the other temperatures measured. At each temperature the crystal was centred by diffraction over several hours before data were collected. Single crystals of $[NiL_2](BF_4)_2$ (**4b**) and $[ZnL_2](BF_4)_2$ (**4c**) were similarly cooled from room temperature at a rate of 1 K min^{-1}. Diffraction data for **4b** were collected at 2 K only, while data for **4c** were collected at 50 K and subsequently 2 K.

5.3 Results and Discussion

5.3.1 $[CoL_2](BF_4)_2$

The cobalt atom in $[CoL_2](BF_4)_2$ (**4a**) is complexed to two ligands through three of the five nitrogen atoms on each ligand. The equatorial Co–N(pyridine) bonds are bound at approximately 180˚ through the Co atom and each is ~ 0.07 Å shorter than the Co–N(pyrazole) bonds. The shape of the ligand prevents a strict octahedral arrangement from being formed, with the N1–Co1–N5 angle being 149.39(6)˚ at 2 K. Each ligand is approximately planar except for one pyrazole ring (N6–N7–C14–C13–C12) which deviates from the planarity of the rest of the ligand by 11.82(9)˚. The complex is shown in Figure 5.4.

The unit cell parameters and refinement details for each of the temperatures at which data were collected are shown in Table 5.2. No crystallographic phase changes were observed between 50 K and 2 K and there were no major changes in the unit cell parameters over the temperature range studied. The BF_4^- counter-ions, which have found to be disordered at higher temperatures in previous studies (Holland *et al.*, 2001a), were fully ordered at all temperatures below 50 K.

Table 5.1: Differences in unit cell parameters on cooling from 50 K to 2 K.

Temperatures	a (Å)	b (Å)	c (Å)	β (˚)	Volume (Å^3)
50 K → 20 K	−0.0021(5)	−0.0081(5)	−0.0024(12)	+0.064(3)	−1.97(14)
20 K → 10 K	−0.0023(6)	−0.0031(6)	−0.0035(12)	+0.015(3)	−1.10(15)
10 K → 2 K	+0.0082(6)	+0.0035(6)	+0.0251(12)	−0.017(3)	+3.65(15)

The unit cell data show a small contraction in the cell volume from 50 K to 10 K, followed by a small but statistically significant increase in the cell volume below 10 K. The differences in cell parameters are shown in Table 5.1. To determine whether the changes in unit cell volume were caused by any change in the spin state of the molecule, the Co–N bond lengths were measured and these are shown in Table 5.3. The pyridyl N atoms are N3 and N8 while the pyrazolyl N atoms are N1, N5, N6 and N8, shown in Figure 5.4. Despite what appears to be a small elongation in all the Co–N bond lengths between 10 K and 2 K, all the bond lengths remain the same within error at all temperatures.

A visual overlay of the structures at 50 K and 2 K show no observable changes in the structure at all. This includes the orientation and position of the BF_4^- anions, which are completely ordered and stay fixed in position at all of the temperatures measured. The magnetic anomaly below 30 K therefore does not have a structural origin, suggesting it might be a purely electronic effect.

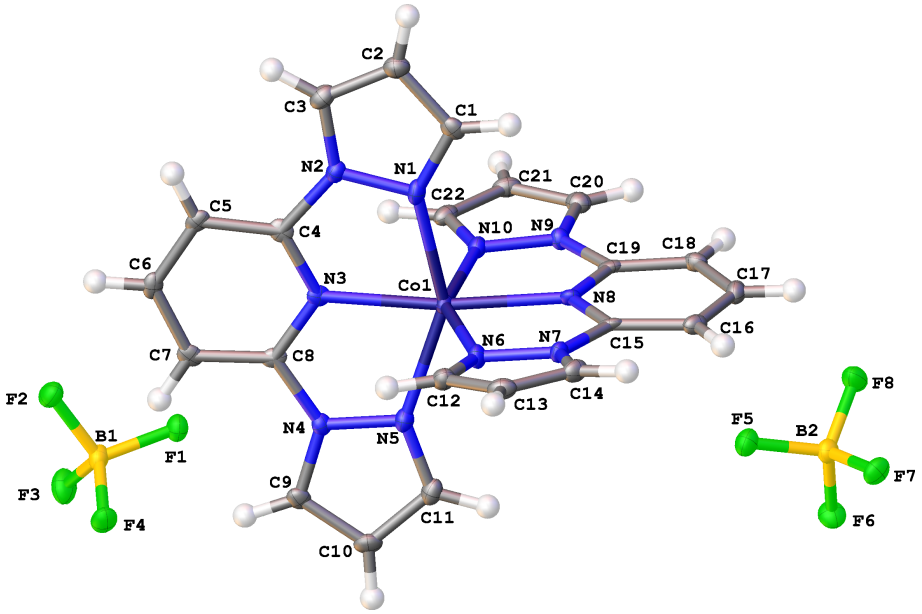

Figure 5.4: The molecular structure of **4a** at 2 K. Thermal elipsoids are drawn at the 75% probability level.

Table 5.2: Crystal data and structure refinement of **4a**

Empirical formula	$C_{22}H_{18}B_2F_8N_{10}Co$			
Formula weight (g mol^{-1})	655.01			
Crystal system, space group, Z	monoclinic, $P2_1$, 2			
Crystal size (mm^3)	0.5 × 0.33 × 0.065			
Crystal shape, colour	plate, clear red			
Temperature (K)	2.0(1)	10.0(1)	20.0(1)	50.0(1)
a (Å)	8.4639(4)	8.4557(4)	8.4580(4)	8.4601(3)
b (Å)	8.4328(4)	8.4293(4)	8.4324(4)	8.4405(3)
c (Å)	18.7252(9)	18.7001(8)	18.7031(9)	18.7055(8)
β (°)	98.003(2)	98.020(2)	98.005(2)	97.941(2)
Volume (Å^3)	1323.48(11)	1319.83(10)	1320.93(11)	1322.90(9)
Calculated density (mg mm^{-3})	1.644	1.648	1.647	1.644
F(000)	658	658	658	658
Wavelength λ, Mo K_α (Å)	0.71073	0.71073	0.71073	0.71073
Absorption coefficient μ (mm^{-1})	0.740	0.742	0.741	0.740
Absorption correction type	multi-scan	multi-scan	multi-scan	multi-scan
Ratio min/max transmission	0.8522	0.8779	0.8577	0.8662
Maximum 2θ (°)	52.84	52.76	52.74	52.76
No. of measured reflections	11605	11470	11602	11461
No. of unique reflections	3887	3926	3942	3934
R_{int}	0.0233	0.0222	0.0231	0.0240
R_1	0.0221	0.0211	0.0212	0.0223
wR_2	0.0524	0.0490	0.0499	0.0510
Data/restraints/parameters	3887/1/388	3926/1/388	3942/1/388	3934/1/388
Goodness-of-fit on F^2	1.037	1.034	1.052	1.043
Largest diff. peak (e Å^{-3})	0.664	0.338	0.325	0.340
Largest diff. peak (e Å^{-3})	−0.218	−0.199	−0.202	−0.235

Table 5.3: Co–N bond lengths at each of the temperatures measured.

	2 K	10 K	20 K	50 K	290 K[a]
Co1–N1	2.1413(20)	2.1396(19)	2.1406(19)	2.1409(19)	2.152(3)
Co1–N3	2.0790(15)	2.0762(14)	2.0758(14)	2.0774(15)	2.073(3)
Co1–N5	2.1607(19)	2.1573(18)	2.1594(18)	2.1590(19)	2.163(3)
Co1–N6	2.1373(20)	2.1355(20)	2.1382(21)	2.1381(21)	2.136(3)
Co1–N8	2.0720(14)	2.0706(13)	2.0704(13)	2.0715(14)	2.068(3)
Co1–N10	2.1607(20)	2.1595(20)	2.1613(20)	2.1630(21)	2.165(3)

[a] Data taken from Holland *et al.* (2001a).

5.3.2 $[NiL_2](BF_4)_2$

The nickel complex, **4b**, was studied as a comparison to the cobalt and zinc compounds. No significant changes were expected as a result of changing the temperature so the complex was studied at 2 K only. Refinement details are shown in Table 5.5 and the asymmetric unit with labels is shown in Figure 5.5. As in **4a**, the complex forms in the monoclinic space group $P2_1$ and has a very similar structure. The N3–Ni1–N8 bond angle was 176.47(10)˚ and the angle between the pyrazole nitrogen atoms and the nickel atom (N1–Ni1–N5) was 154.03(7)˚. No disorder was present in either of the BF_4^- anions.

Table 5.4: Ni–N bond lengths at 2 K and 150 K.

	2 K	150 K[a]
Ni1–N1	2.0958(23)	2.1006(16)
Ni1–N3	2.0120(18)	2.0143(14)
Ni1–N5	2.1253(22)	2.1229(16)
Ni1–N6	2.0854(23)	2.0944(16)
Ni1–N8	2.0120(17)	2.0122(13)
Ni1–N10	2.1159(22)	2.1187(16)

[a] Data taken from Holland *et al.* (2001a).

The bond lengths measured at 2 K, shown in Table 5.4, are identical within error to the values obtained at 150 K by Holland *et al.* (2001a) with the exception of of Ni1–N6 where the difference is only barely significant crystallographically. Aside from a small contraction in the unit cell parameters of 1.4% between 150 K and 2 K, no changes are observed in this structure between 150 K and 2 K.

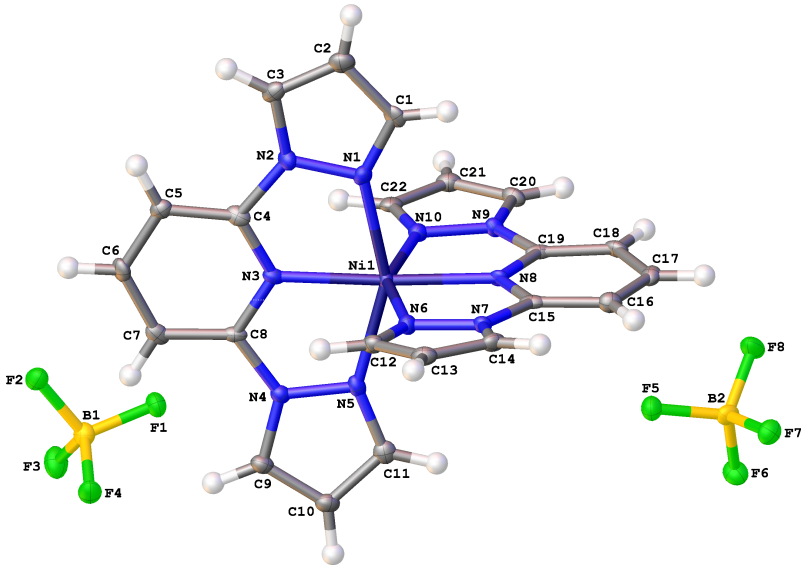

Figure 5.5: The molecular structure of **4b** at 2 K. Thermal elipsoids are drawn at the 75% probability level.

Table 5.5: Crystal data and structure refinement of **4b** at 2 K.

Empirical formula	$C_{22}H_{18}B_2F_8N_{10}Ni$
Formula weight (g mol^{-1})	654.79
Temperature (K)	2.0(1)
Crystal system, space group, Z	monoclinic, $P2_1$, 2
a (Å)	8.4365(3)
b (Å)	8.4812(3)
c (Å)	18.5354(7)
β (°)	97.644(2)
Volume (Å^3)	1314.45(8)
Calculated density (mg mm^{-3})	1.654
F(000)	660
Crystal size (mm^3)	0.35 × 0.2 × 0.18
Crystal shape, colour	block, clear blue
Wavelength λ, Mo K_α (Å)	0.71073
Absorption coefficient μ (mm^{-1})	0.830
Absorption correction type	multi-scan
Ratio min/max transmission	0.8171
Maximum 2θ (°)	52.76
No. of measured reflections	9786
No. of unique reflections	4254
R_{int}	0.0200
R_1, wR_2	0.0270, 0.0687
Data/restraints/parameters	4254/1/388
Goodness-of-fit on F^2	1.028
Largest diff. peak/hole (e Å^{-3})	1.379/−0.535

5.3.3 $[ZnL_2](BF_4)_2$

With a d^{10} electron configuration, the zinc complex **4c** has only one possible electron configuration. However, as the unit cell parameters are often very similar to those of analogous iron(II) complexes, zinc(II) has been used in several studies into the effects of metal dilution on the spin transition (*e.g.* Ganguli *et al.*, 1982; Sanner *et al.*, 1984; Baldé *et al.*, 2008). For this reason the structure was initially reported as a comparison to the analogous copper(II) complex described above (Solanki *et al.*, 2002).

With very similar, but not crystallographically identical, *a* and *b* axis lengths the majority of the crystals which were examined were found to be twinned by rotation of 90° about the *c* axis. Eventually a small untwinned crystal was found, of 0.20 × 0.15 × 0.05 mm, which was cooled to 50 K at 1 K min^{-1} and subsequently to 2 K at the same rate, with full data collections performed at both temperatures.

Due to the small size of the crystal long exposures were required for each diffraction image. This dramatically increased the background scattering from the beryllium shrouds compared to the intensity of the reflections from the crystal, which had an effect on the quality of the measured data. To mitigate this *Masquerade* (Chapter 3; Coome *et al.*, 2012) was employed to generate masks for the beryllium scattering.

5.3.3.1 Improving the Data with *Masquerade*

A set of φ scans were collected with the detector at a distance of 70 mm from the sample, with each diffraction image being exposed for 25 s and covering 0.5°. These scans were then repeated with the detector at 120 mm from the sample. Using the procedure described in Chapter 3 the shroud offsets were calculated for each of the temperatures measured. Due to the thermal contraction of the sample mount between the two temperatures the sample requires re-centring every time the temperature is changed, leading to different shroud offsets.

Table 5.6: Shroud offsets calculated for **4c** at 2 K and 50 K.

	Inner Shroud		Outer Shroud	
Temperature (K)	x_t (mm)	y_t (mm)	x_t (mm)	y_t (mm)
2	0.2931	0.7458	−0.4513	2.2369
50	0.3345	0.8948	−0.2105	2.0873

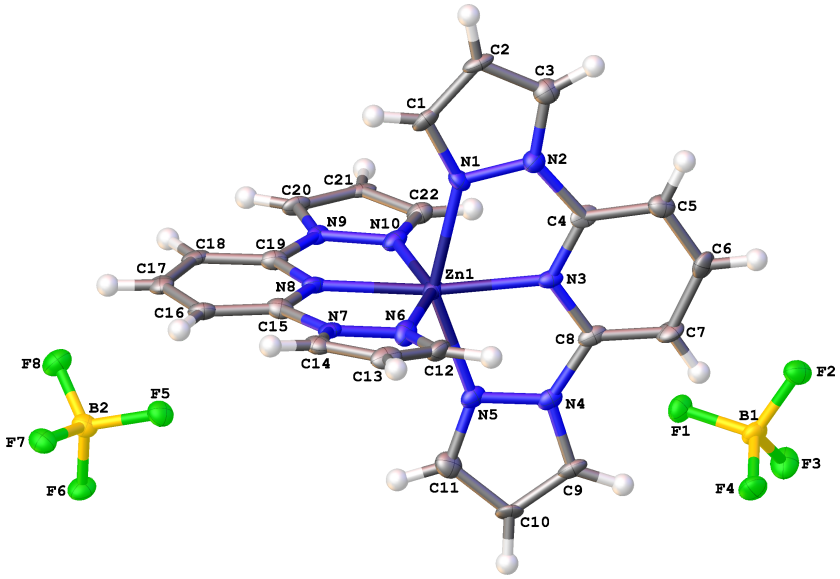

Figure 5.6: The molecular structure of **4c** at 2 K. Thermal elipsoids are drawn at the 75% probability level.

Table 5.7: Crystal data and structure refinement of **4c** at 2 K and 50 K.

Empirical formula	$C_{22}H_{18}B_2F_8N_{10}Zn$			
Formula weight (g mol^{-1})	661.45			
Crystal system, space group, Z	monoclinic, $P2_1$, 2			
Crystal size (mm^3)	0.20 × 0.15 × 0.05			
Crystal shape, colour	block, clear light yellow			
Temperature (K)	2.0(1)	2.0(1)	50.0(1)	50.0(1)
Masks used	Masked	Unmasked	Masked	Unmasked
a (Å)	8.4518(6)	8.4485(7)	8.4416(5)	8.4441(7)
b (Å)	8.4294(5)	8.4292(7)	8.4305(5)	8.4349(8)
c (Å)	18.7510(12)	18.7549(15)	18.7354(11)	18.7526(17)
β (°)	97.361(3)	97.342(3)	97.214(3)	97.202(3)
Volume (Å^3)	1324.88(15)	1324.66(19)	1322.79(14)	1325.1(2)
Calculated density (mg mm^{-3})	1.658	1.658	1.661	1.658
F(000)	664	664	664	664
Wavelength λ, Mo K_α (Å)	0.71073	0.71073	0.71073	0.71073
Absorption coefficient μ (mm^{-1})	1.018	1.018	1.020	1.018
Absorption correction type	multi-scan	multi-scan	multi-scan	multi-scan
Ratio min/max transmission	0.8051	0.8885	0.8214	0.8543
Maximum 2θ (°)	52.94	52.76	52.9	52.86
No. of measured reflections	10082	9587	9597	9524
No. of unique reflections	3374	3666	3342	3668
R_{int}	0.0454	0.0482	0.0458	0.0521
R_1	0.0368	0.0410	0.0406	0.0471
wR_2	0.0787	0.0882	0.0851	0.1118
Data/restraints/parameters	3374/1/388	3666/1/388	3342/1/388	3668/1/388
Goodness-of-fit on F^2	1.074	1.061	1.059	1.035
Largest diff. peak (e Å^{-3})	0.559	0.605	0.835	0.897
Largest diff. hole (e Å^{-3})	−0.427	−0.442	−0.416	−0.578

With these shroud offsets, masks were then calculated for the three lowest-angle beryllium reflections, at 20.682°, 22.873° and 23.667°, producing masks with twelve overlapping rings. The diffraction images were processed with *SAINT* (Bruker, 2009) to extract the reflection intensities, separately for each distance of the detector when the frames were exposed. As a comparison, the images were also processed without masks for the data collected at 70 mm only.

5.3.3.2 Results

The structure shows no major changes between 50 K and 2 K. As with **4a**, the unit cell appears to expand slightly at 2 K although this is a very small effect (0.16%). The M–N bond lengths (Table 5.8) remain the same within error at the two temperatures measured with the XIPHOS and the previous study at 100 K. It can also be seen that the use of *Masquerade* has reduced the uncertainties of all the bond lengths in Table 5.8.

Table 5.8: Zn–N bond lengths at 2 K, 50 K and 100 K in **4c**.

	2 K		50 K		100 K[a]
	Masked	Unmasked	Masked	Unmasked	
Zn1–N1	2.182(4)	2.185(5)	2.183(4)	2.192(6)	2.185(3)
Zn1–N3	2.096(3)	2.097(4)	2.099(3)	2.097(4)	2.097(3)
Zn1–N5	2.177(4)	2.176(5)	2.175(4)	2.171(6)	2.176(3)
Zn1–N6	2.159(4)	2.156(5)	2.154(5)	2.155(6)	2.164(3)
Zn1–N8	2.109(3)	2.115(4)	2.105(3)	2.103(4)	2.107(3)
Zn1–N10	2.186(4)	2.188(5)	2.175(5)	2.191(6)	2.193(3)

[a] Data taken from Solanki *et al.* (2002).

In addition to the improvement in bond length uncertainties, the various agreement factors R_1, wR_2, R_{int} and R_σ are all improved through the use of *Masquerade*, as can be seen in Table 5.7. This confirms the results from Chapter 3, and emphasises the improvements which can be obtained by removing the background from the beryllium rings with *Masquerade*.

5.3.4 Comparisons

Each of these metal complexes remain essentially unchanged from room temperature to 2 K except for a contraction in the anisotropic displacement parameters as the temperature is lowered. Bond lengths remain the same and unit cells change very little. In addition, no crystallographic phase changes were seen in any of the complexes.

The ligands in all of the structures described here are not strictly planar. One pyrazole ring in particular, containing N6 and N7, is tilted at an angle of ~ 11° from the other pyrazole ring in the same ligand in each of the structures. Another asymmetry is found in the angle between the pyrazole nitrogen of one ring and the pyridyl nitrogen of the other ligand. These features, among others, mean that the molecule is not symmetric by inversion.

As the space group ($P2_1$) in which all of the complexes crystallise is chiral and there is only one molecule in the asymmetric unit, this means that each crystal contains only one enantiomer of the material. The absolute configuration of a crystal, or which enantiomer is present, can be estimated with the Flack parameter in such a space group (Flack, 1983). This parameter is calculated as part of the crystal structure refinement process and values reported here are provided by *Olex2* (Dolomanov *et al.*, 2009).

Table 5.9: The calculated Flack parameters for the crystal structures of **4a**, **4b** and **4c** at 2 K.

	Co (**4a**)	Ni (**4b**)	Zn (**4c**)
Presented	0.014(9)	0.026(9)	0.024(13)
Inverted	0.688(17)	0.853(18)	0.66(2)

In order to conclude that the absolute configuration of a crystal has been determined satisfactorily, certain conditions have been laid out by Flack & Bernardinelli (2000). For a calculated Flack parameter $x(u)$, these conditions are met when the value of u is smaller than 0.04 and the value of x is within $3u$ of zero. It can be seen that the values calculated for the presented structures in Table 5.9 all meet these criteria, while those for the inverted structures clearly do not. Hence the absolute configuration of all these complexes may be said to be well determined.

An interesting result in light of this determination is that complexes **4a** and **4b** have the same handedness, while complex **4c** has the opposite hand. This difference appears to be confirmed by diagrams in the separate papers in which these structures were originally published. However, it is not clear if this is due to coincidence, in which case other crystals of the opposite handedness may be found, or if this is due to an intrinsic property of the material.

Table 5.10: Selected bond angles (°) for all three complexes at 2 K.

	Co (**4a**)	Ni (**4b**)	Zn (**4c**)
N3–M–N8	172.72(8)	176.47(10)	172.43(17)
N1–M–N5	149.39(6)	154.03(7)	148.38(12)
N6–M–N10	150.80(6)	153.96(7)	148.74(12)

Aside from the change in handedness, the structures of **4a** and **4c** are very similar. Bond

angles between the metal and the ligands are shown in Table 5.10. The structure of **4b** is slightly different, with the bond angles showing that the structure is slightly more octahedral about the metal centre.

5.4 Conclusions

A series of metal complexes of the form $[ML_2](BF_4)_2$, where L = 2,6-di(pyrazol-1-yl)-pyridine and M = Co (**4a**), Ni (**4b**) and Zn (**4c**), have been studied at ultra-low temperatures. These complexes share the same structure as a previously reported iron(II) complex which shows spin crossover behaviour centred at 259 K and also a copper(II) complex which exhibits Jahn-Teller ordering at 41 K.

A magnetic susceptibility study on **4a** showed an anomaly below 30 K, which prompted a low temperature crystallographic study to determine if there was a change in the crystal structure associated with the anomaly. A study on **4c**, which has only one possible spin configuration, was carried out to compare any changes in structure and to deconvolute changes due to temperature from those due to the magnetic transition. A further study on **4b** was carried out to investigate whether this complex shows any interesting behaviour at very low temperatures.

No crystallographic phase changes were observed in any of the materials. The atomic positions and the bond lengths remained the same in each of the crystals after cooling to 2 K compared with the higher temperature structures presented in this study and in previous reports. A marked reduction in the anisotropic thermal displacement parameters was observed in each of the structures as a result of cooling to 2 K; for instance, the average atomic U_{eq} decreases by 36.4% between 50 K and 2 K in **4a**.

The atomic coordinates and the vibrational information provided by the anisotropic thermal displacement parameters provide a useful starting point for computational studies of these materials. Software such as *CASTEP* (Segall *et al.*, 2002) may be used to calculate many properties of interest such as charge densities, band structure, vibrational spectra, phonon interactions and of particular interest in this case, magnetic response properties. The accurate atomic coordinates and unit cell information determined in the experiments described above are crucial to these calculations which would alternatively have to rely on highly computationally expensive geometry optimisation steps.

The unit cell and atomic coordinate information is also invaluable when combined with studies of the magnetic structure by neutron diffraction. Such studies may elucidate the magnetic behaviour of **4a** and how this differs from the highly similar structure of **4c**.

The data collected on **4c** were from a relatively small crystal and hence longer exposure times were required than for the other two crystals. The lengthening of the exposure time increased the background scattering from the beryllium shrouds but this has been mitigated by the use of *Masquerade*. The improvements in data quality obtained confirm the previous results and again demonstrate the usefulness of this technique in collecting high quality data at ultra low temperatures.

Chapter 6

Organic Radicals and Single Molecule Magnets

6.1 Spin Transitions in 3-cyanobenzo-1,3,2-dithiazolyl

The dithiazolyl radical complex, 3-cyanobenzo-1,3,2-dithiazolyl (**5**) has previously been shown to exhibit a thermally driven spin-transition at 250 K between a paramagnetic phase at high temperature and a diamagnetic phase at lower temperatures. This transition is a result of a packing change, rather than a change in spin state of individual molecules as in spin crossover materials (Alberola *et al.*, 2006).

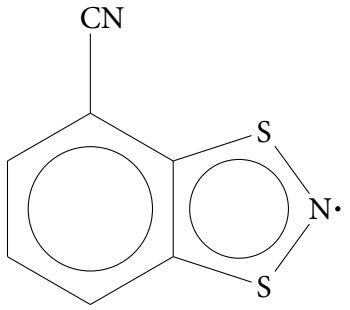

Figure 6.1: The formula of 3-cyanobenzo-1,3,2-dithiazolyl, **5**.

At room temperature the radicals pack in an evenly spaced π-stack with a layer separation of ~ 3.6 Å. Below the transition temperature, at 180 K, these layers separate and form a dimeric π-stack arrangement instead, with layer separations of ~ 3.2 Å and ~ 3.8 Å. The crystal structure remains in the same space group but the radical dimerisation corresponds to a doubling of the unit cell *a* axis.

There is also a second magnetic phase transition in this material, occurring below 50 K. Unlike the higher temperature phase transition this has an associated hysteresis with a transition temperature of 39 K on cooling and 26 K on warming. In order to investigate this second phase transition, low temperature X-ray diffraction experiments were performed with the Xiphos diffractometer.

6.1.1 Experimental

Crystals were synthesised following literature methods (Alberola *et al.*, 2006) by Prof. J. Rawson at the University of Windsor in Canada.

A small crystal, measuring $0.18 \times 0.10 \times 0.03$ mm^3, was found and initially mounted on the Displex with a beryllium outer shroud and a foil inner shroud. In this configuration the crystal was cooled at 1 K min^{-1} to 200 K, then centred and diffraction data were collected. After this the crystal was cooled at 1 K min^{-1} to 75 K and data were collected again after centring the sample within the primary beam.

After data collection at 75 K had finished, the Displex developed a fault and the crystal was warmed to room temperature. After the fault was rectified the crystal was again mounted on the Displex but this time with beryllium inner and outer shrouds. Following this, the crystal was cooled at 1 K min^{-1} directly to 2 K, centred and data were collected. The crystal was then warmed to 33.5 K, above the phase transition, at 0.5 K min^{-1} and data were again collected.

Table 6.1: Shroud offsets calculated for **5** at all the temperatures measured.

	Inner Shroud		Outer Shroud	
Temperature (K)	x_t (mm)	y_t (mm)	x_t (mm)	y_t (mm)
200	-	-	−0.2506	2.2378
75	-	-	0.0478	2.2378
33.5	0.4838	0.8951	0.0373	2.3870
2	0.4781	1.0443	0.0478	2.2378

Data were collected with φ scans with each image covering 0.5˚. Due to the small size of the crystal each image was exposed for 30 s, giving rise to a high background from the beryllium shrouds. For this reason *Masquerade* was used to generate masks for the beryllium scattering to be used during reflection integration with *SAINT*. The shroud offsets which were calculated for the data collection at each temperature are shown in Figure 6.1. At all temperatures, data were collected with the detector at 70 mm and 120 mm.

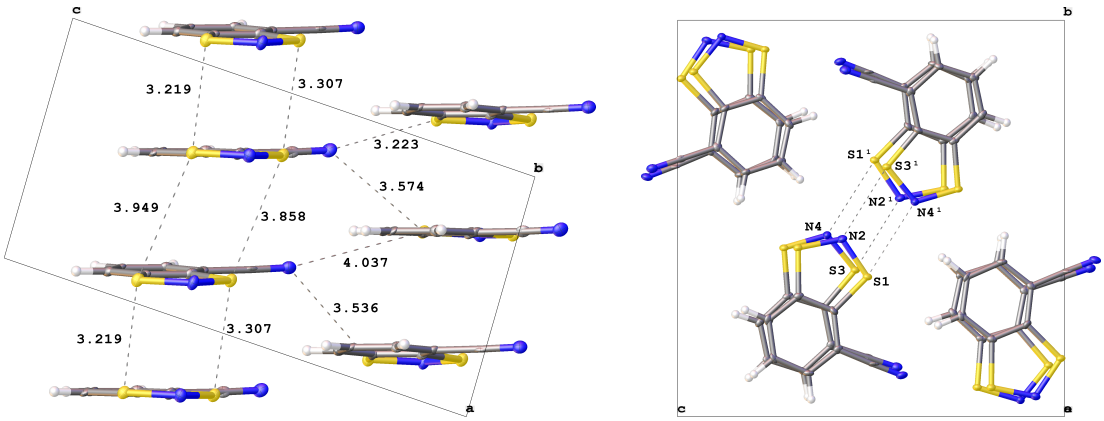

(a) Along the *b* axis (b) In the *bc* plane

Figure 6.2: Views of the packing in **5** at 2 K, showing the dimerisation of the radicals below the structural phase transition at 250 K.

Table 6.2: Selected atomic distances for **5** at the four temperatures measured.

(a) Intra-dimer S–S contacts.

Distance (Å)	2 K	33.5 K	75 K	200 K
S1–S3	3.3074(17)	3.3097(18)	3.3159(18)	3.3566(16)
S2–S4	3.2187(17)	3.2209(18)	3.2273(18)	3.2740(17)

(b) Inter-dimer S–S contacts.

Distance (Å)	2 K	33.5 K	75 K	200 K
S1–S3[a]	3.8580(16)	3.8623(17)	3.8664(17)	3.8963(15)
S2–S4[a]	3.9488(15)	3.9530(17)	3.9554(17)	3.9785(16)

[a] $1+x, y, z$

(c) N–S contacts in the *bc* plane.

Distance (Å)	2 K	33.5 K	75 K	200 K
S1–N4[b]	3.240(3)	3.247(3)	3.253(3)	3.298(3)
N2–S3[b]	3.087(3)	3.091(3)	3.107(3)	3.159(3)

[b] $2-x, -y, -z$

(d) CN–S contacts.

Distance (Å)	2 K	33.5 K	75 K	200 K
N1–S2[c]	3.574(4)	3.575(4)	3.586(4)	3.632(4)
N3–S4[c]	3.536(4)	3.543(4)	3.556(4)	3.607(4)
N1–S4[c]	3.223(3)	3.221(4)	3.229(3)	3.259(3)
N3–S2[d]	4.037(3)	4.043(3)	4.038(3)	4.029(3)

[c] $x, \frac{1}{2}-y, -\frac{1}{2}+z$ [d] $1+x, \frac{1}{2}-y, -\frac{1}{2}+z$

6.1.2 Results and Discussion

The molecular structure remains in the same space group between 200 K and 2 K with no significant changes except for a thermal contraction in the unit cell parameters, shown in Table 6.4. The data at 33.5 K were collected after warming from 2 K and hence the sample should be above the transition at 26 K on warming. Various intermolecular contacts are shown in Table 6.2, which demonstrate that no significant changes occur as a result of the low temperature phase transition between the lowest temperatures measured, 2 K and 33.5 K.

The small size of the crystal and the subsequent long exposure times which were required to collect data on this complex suggested that the data quality could be improved by use of *Masquerade*. Data were collected with the detector at 70 mm and 120 mm from the crystal and integrated with masks generated by *Masquerade*. Selected parameters are shown in Table 6.3 for data collected at 2 K and 75 K.

Table 6.3: Selected parameters from the structural refinements of **5** showing the improvements in data quality when masks are used for two beryllium shrouds (2 K) and only one beryllium shroud (75 K).

	2 K		75 K	
	Masked	Unmasked	Masked	Unmasked
R_{int}	0.0898	0.0887	0.0756	0.0722
R_1	0.0487	0.0641	0.0485	0.0607
wR_2	0.1033	0.1338	0.1066	0.1326
Distance S1–S3 (Å)	3.3074(17)	3.307(3)	3.3159(18)	3.317(3)
Distance S2–S4 (Å)	3.2187(17)	3.217(3)	3.2273(18)	3.227(2)

The data show that both R_1 and wR_2 are improved significantly and that the errors in bond distances are also reduced in the structure for which masks were used, compared to the structure using data collected at 70 mm only and integrated without masks. The data are improved both at 2 K, when two beryllium shrouds were used, and also at 75 K when only one beryllium shroud was used, as shown in Table 6.3.

6.1.3 Conclusions

The radical complex studied here, 3-cyanobenzo-1,3,2-dithiazolyl (**5**), exhibits two magnetic phase transitions. The high temperature transition at 250 K has been previously studied by Alberola *et al.* (2006), and was found to have an associated structural change in

Table 6.4: Crystal data and structure refinement of **5** at the temperatures measured.

Empirical formula	$C_7H_3N_2S_2$			
Formula weight (g mol^{-1})	179.23			
Crystal system, space group, Z	monoclinic, $P2_1/c$, 8			
Crystal size (mm^3)	$0.18 \times 0.10 \times 0.03$			
Crystal shape, colour	block, dark red			
Temperature (K)	2.0(1)	33.5(1)	75.0(1)	200.0(1)
a (Å)	7.0950(5)	7.1018(5)	7.1130(6)	7.1909(6)
b (Å)	14.2176(11)	14.2366(10)	14.2446(12)	14.2782(13)
c (Å)	13.9135(10)	13.9282(9)	13.9543(11)	14.0247(12)
β (°)	92.924(4)	92.978(4)	93.068(5)	93.522(4)
Volume (Å^3)	1401.68(18)	1406.32(17)	1411.8(2)	1437.2(2)
Calculated density (mg mm^{-3})	1.699	1.693	1.686	1.657
F(000)	728	728	728	728
Wavelength λ, Mo K_α (Å)	0.71073	0.71073	0.71073	0.71073
Absorption coefficient μ (mm^{-1})	0.677	0.674	0.672	0.660
Absorption correction type	multi-scan	multi-scan	multi-scan	multi-scan
Ratio min/max transmission	0.8291	0.8632	0.8461	0.8665
Maximum 2θ (°)	52.82	52.82	52.76	52.76
No. of measured reflections	10257	10207	11683	11652
No. of unique reflections	2236	2242	2444	2462
R_{int}	0.0898	0.0914	0.0756	0.0746
R_1	0.0487	0.0506	0.0485	0.0488
wR_2	0.1033	0.1049	0.1066	0.1055
Data/restraints/parameters	2236/0/199	2242/0/199	2444/0/199	2462/0/199
Goodness-of-fit on F^2	1.041	1.037	1.040	1.026
Largest diff. peak (e Å^{-3})	0.464	0.445	0.439	0.380
Largest diff. hole (e Å^{-3})	−0.360	−0.408	−0.389	−0.298

which the radical layers, evenly spaced above the transition temperature, separate and form a dimeric stack below the transition temperature.

The low temperature magnetic phase transition had been observed by magnetic measurements in the previous study, but had not been characterised structurally due to the low temperatures involved. These temperatures are readily accessible with the Xiphos and so a new low temperature study, described herein, was carried out to determine whether the magnetic transition was accompanied by a structural change. This study determined that the space group and unit cell parameters were unchanged except for the expected thermal contraction and the intermolecular contacts remained the same within error between 33.5 K (above the transition) and 2 K (below the transition).

The use of masks generated by *Masquerade* and the recovery of missing reflections by collecting data at multiple detector distances was again shown to improve the quality of the data which can be obtained from small crystals. The internal agreement factors R_1 and

wR_2 showed significant improvement when *Masquerade* was used and the errors in bond lengths was also shown to decrease.

6.2 A Study of *para*-Chloroanilinium Tetrachlorocuprate

A series of ammonium salts of the form $[RNH_3]_2CuCl_4$ have previously been studied which form layers of $CuCl_4^{2-}$ ions, interspersed with RNH_3^+ cations (Willett *et al.*, 1988). The $CuCl_4^{2-}$ ions exhibit Jahn-Teller distortion in the plane of the layer and this has been reported to lead to ferromagnetic interactions across the Cl–Cu–Cl bridge. One member of the series, $[ArNH_3]_2CuCl_4$ is reported to exhibit bulk ferromagnetism between 7.5 K and 11 K (Nelson *et al.*, 1996).

Another salt in the series, $[p\text{–}ClC_6H_4NH_3]_2CuCl_4$ (**6**), shows a wide range of structural and magnetic phase changes. The crystal structure has been reported previously at room temperature (~ 290 K) and was found to adopt the monoclinic space group $P2_1/c$ (Sekine *et al.*, 1996). Studies have also shown that the complex undergoes two structural phase transitions in a very small temperature range at 277 K and 275 K, as well as a magnetic phase transition at 9 K (Ishikawa *et al.*, 1983), but none of these had been structurally characterised.

Below the magnetic phase transition at 9 K an antiferromagnetic ground state is observed, shown in Figure 6.3, which is a result of weak antiferromagnetic interactions between layers. In order to determine whether these interactions have any structural origin, crystallographic studies were undertaken with the Xiphos at two temperatures above and below this transition temperature (3 K and 15 K). In addition, data were collected at room temperature to examine the high temperature structural phase transitions.

6.2.1 Experimental

Crystals were synthesised following literature methods by Dr R. I. Thomson at the University of Cambridge. A small crystal, measuring $0.20 \times 0.20 \times 0.03$ mm^3, was mounted on the Displex with a beryllium outer shroud and a foil inner shroud. The crystal was cooled to 15 K at 0.5 K min^{-1}, then centred and diffraction data were collected. When this was completed the crystal was cooled to 3 K at 0.5 K min^{-1}, centred and again data were collected. The Displex was then switched off and allowed to warm to room temperature, where the shrouds were removed, and data were collected after centring at room temperature (290 K).

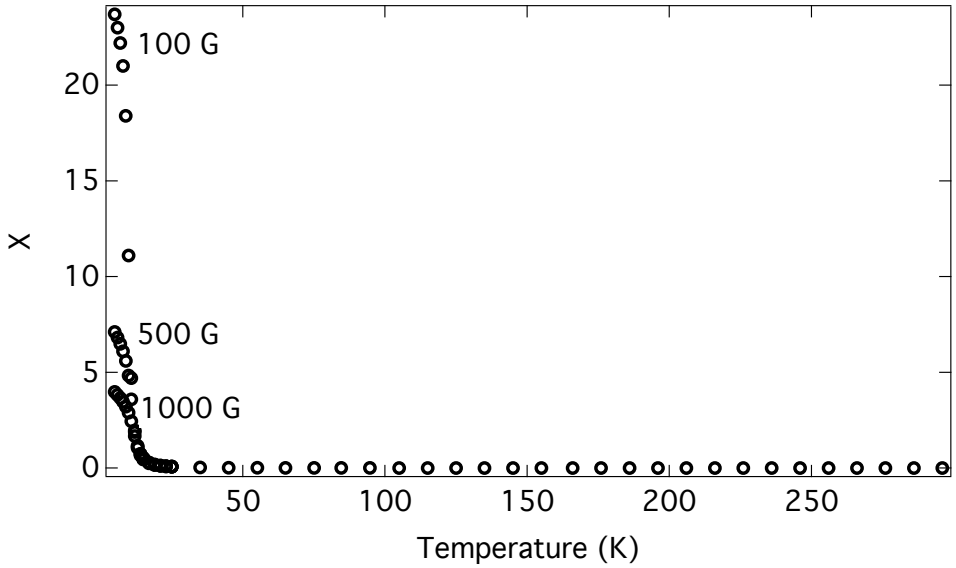

Figure 6.3: The magnetic susceptibility, χ, of **6** between 5 K and 300 K with different applied field strengths, showing the phase transition at 9 K. Image provided courtesy of Dr R. I. Thomson, University of Cambridge.

6.2.2 Results and Discussion

When studied previously the crystal was found to adopt the space group $P2_1/c$ at room temperature and this has been confirmed by the data collected in this study. A closer examination of the diffraction pattern, however, revealed that the crystal was twinned by rotation of 180° about the *c* axis. The occupancy of the minor component of the twin refines to approximately 20% in *SHELXL* (Sheldrick, 2008a).

When cooled below 275 K the crystal is found to undergo an abrupt structural phase transition from monoclinic $P2_1/c$ to orthorhombic, space group $Pccn$, with an associated doubling of the unit cell volume and a reorientation of the cell axes ($a' = b$, $b' = 2a$, $c' = c$). The change in the crystal packing can be seen in Figure 6.4, which also demonstrates the reorientation of the unit cell.

The twinning which was observed at higher temperatures is no longer evident below the phase transition. The *a* axis above the phase transition doubles in length to become *b* below the transition, but also changes orientation so that it is now perpendicular to the other two axes. As a result the two twin domains become parallel and the two-fold axis which is implied by space group $Pccn$ is now coincident with the rotation relating the domains and hence the twinning is no longer observed. When the crystal is warmed above the phase transition the twinning returns. No studies have yet examined whether the twin ratio stays the same when cycled through the transition.

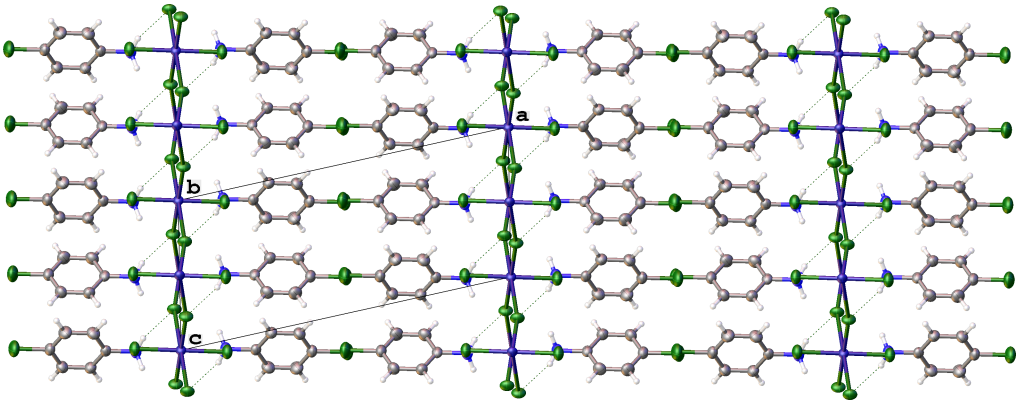

(a) View of the packing along the *b* axis at 290 K.

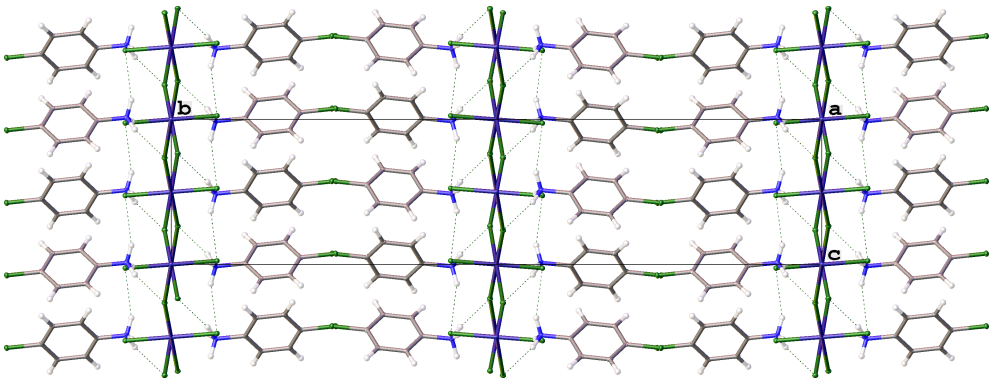

(b) View of the packing along the *a* axis at 3 K.

Figure 6.4: Comparison of the packing in **6** (a) above and (b) below the structural phase transition at 275 K.

6.2.2.1 Low Temperature Studies

The unit cell parameters do not show any large changes between 15 K and 3 K and no change in space group symmetry is observed. The unit cell volume changed by 0.59(13) Å through the transition, which is barely significant crystallographically. The measured bond lengths, a selection of which are shown in Table 6.5, show no changes within error between the two temperatures and only minor changes from the structure at room temperature. It is therefore clear that the magnetic phase transition at 9 K does not have an obvious structural origin.

Table 6.5: Selected bond lengths and atomic distances in **6** at all the temperatures measured.

Distance (Å)	3 K	15 K	290 K
Cu1–Cl3	2.2807(3)	2.2804(3)	2.2660(5)
Cu1–Cl2	2.3026(4)	2.3027(4)	2.3078(4)
Cu1–Cl2[a]	2.8659(4)	2.8654(4)	2.9060(4)

[a] $Pccn$: $\frac{1}{2}-x, y, -\frac{1}{2}+z$; $P2_1/c$: $-x, \frac{1}{2}+y, \frac{1}{2}-z$

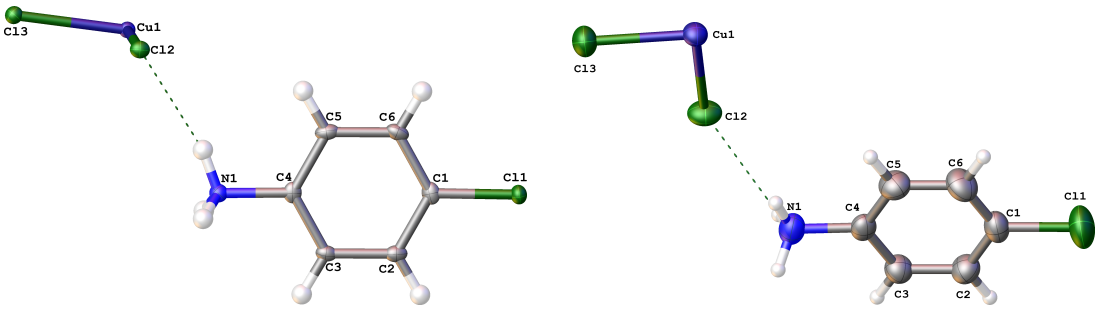

(a) 3 K (b) 290 K

Figure 6.5: The asymmetric unit of **6** at 3 K in space group $P\,c\,c\,n$ and at 290 K in space group $P\,2_1/c$. Thermal displacement parameters are displayed at a probability level of 50% for the structure at 290 K and 75% for the structure at 3 K.

Table 6.6: Crystal data and structure refinement of **6** at various temperatures.

Empirical formula	$C_{12}H_{14}Cl_6CuN_2$		
Formula weight (g mol^{-1})	462.49		
Crystal size (mm^3)	0.20 × 0.20 × 0.03		
Crystal shape, colour	plate, clear light yellow		
Crystal system, space group, Z	orthorhombic, $P\,c\,c\,n$, 4		monoclinic, $P\,2_1/c$, 2
Temperature (K)	3.0(1)	15.0(1)	290(2)
a (Å)	7.3560(3)	7.3563(2)	16.4216(5)
b (Å)	32.0322(11)	32.0281(10)	7.3981(2)
c (Å)	7.1282(2)	7.1263(2)	7.2606(2)
α (°)	90	90	90
β (°)	90	90	101.4920(10)
γ (°)	90	90	90
Volume (Å^3)	1679.61(10)	1679.02(8)	864.40(4)
Calculated density (mg mm^{-3})	1.829	1.830	1.777
F(000)	924	924	462
Wavelength λ, Mo K_α (Å)	0.71073	0.71073	0.71073
Absorption coefficient μ (mm^{-1})	2.247	2.247	2.183
Absorption correction type	multi-scan	multi-scan	multi-scan
Ratio min/max transmission	0.8577	0.8669	0.8703
Maximum 2θ (°)	52.7	52.7	52.74
No. of measured reflections	16809	16794	2972
No. of unique reflections	1705	1705	2972
R_{int}	0.0288	0.0275	0.0175, 0.0279
R_1, wR_2	0.0180, 0.0453	0.0181, 0.0456	0.0274, 0.0712
Data/restraints/parameters	1705/0/98	1705/0/98	2972/0/99
Goodness-of-fit on F^2	1.074	1.091	1.048
Largest diff. peak/hole (e Å^{-3})	0.397/−0.290	0.394/−0.271	0.462/−0.247

6.2.3 Conclusions

The $[p\text{–}ClC_6H_4NH_3]_2CuCl_4$ salt (**6**) has been shown to undergo a high temperature structural phase transition at ~ 275 K, as well as a low temperature magnetic transition at ~ 9 K. Both have been studied by X-ray diffraction with the Xiphos. The high temperature structural transition has been characterised, but studies above and below the low temperature magnetic transition have demonstrated that no structural change takes place at 9 K. This work will appear as part of a larger study in a paper to be published later this year (Thomson *et al.*, 2012).

6.3 Single Molecule Magnets

The compounds studied in this section were provided by Mr Andrew Farrell from the University of Glasgow.

Single molecule magnets (SMMs) are molecules which exhibit slow magnetic relaxation with an associated hysteresis below a characteristic blocking temperature, T_b (Aromí *et al.*, 1998; Gatteschi & Sessoli, 2003). Although the highest blocking temperature is only 8.3 K at present (Rinehart *et al.*, 2011), work is ongoing to raise this temperature to make the materials useful for various applications.

Although the SMM properties are primarily attributable to the molecule itself, they are also affected by intermolecular interactions. Changes in the molecular environment lead to changes in the hysteresis width and the relaxation rate of the magnetism, leading to changes in T_b. The intermolecular interactions are affected by changes to the solid-state structure of the materials and hence understanding how these are affected by the temperature could lead to structures with a higher T_b.

At present, most studies correlating solid-state structure and magnetic properties attempt to use magnetic data from below the T_b with the solid state structure obtained at much higher temperatures, generally in the range of open-flow nitrogen cryostats (> 80 K). This obviously does not take into account any structural changes which may occur at lower temperatures, so it is important to be able to measure the single crystal structure below T_b in order to better correlate the 3D structure and the magnetic properties. Due to the low temperatures involved, the Xiphos is one of very few X-ray diffractometers able to measure these structures below T_b.

In addition to the X-ray structures presented here, ultra-low temperature neutron diffraction experiments are being undertaken using the VIVALDI[1] instrument (Wilkinson *et al.*, 2002) at the Institute Laue-Langevin, Grenoble (Farrell, 2012). These neutron data will allow the accurate determination of the hydrogen atom positions to complement the heavy atom positions already determined from the X-ray data. It is also important to note that unit cell parameters cannot be determined accurately with VIVALDI, a multi-wavelength Laue diffractometer, so X-ray data collected on the XIPHOS at the same temperature as the neutron studies are vital to the success of the neutron structure determination.

6.3.1 A Low Temperature Study of Mn_{12} Acetate

The archetypal SMM compound is $[Mn_{12}O_{12}(CH_3COO)_{16}(H_2O)_4] \cdot 4\,H_2O \cdot 2\,CH_3COOH$ (**7**), known as Mn_{12}-acetate (Sessoli *et al.*, 1993). The structure was first reported at room temperature by Lis (1980) but it took a further two decades for a low temperature structure to be reported: first a neutron structure at 20 K by Langan *et al.* (2001) and then an X-ray structure at 83 K to better study some of the disorder in the structure (Cornia *et al.*, 2002).

The cluster (**7**) crystallises in a tetragonal space group, $I\bar{4}$, with ¼ of a molecule in the asymmetric unit and 2 molecules in the unit cell. The structure shows no change in space group on cooling to 2 K and there are no major changes to the structure. Refinement data are shown in Table 6.7. The disorder reported at 83 K in the $MeCOO^-$ ligands was visible, as well as the disorder in the position of the MeCOOH solvent. One significant difference was in the refined occupancy of the disordered parts. In the previous study at 83 K the MeCOOH solvent disorder was modelled so that each molecule had an occupancy of ½ and the disordered $MeCOO^-$ ligand refined to a ratio of 46:54.

In the structure reported here at 2 K (shown in Figure 6.6), however, the solvent occupancy refines to ~ 35%, as does the occupancy of the disordered part of the $MeCOO^-$. It was previously reported that the disorder in the position of the solvent affected that of the ligand through the hydrogen bonding, but in that study the solvent was present in the stoichiometric 1:2 ratio. This appears not to be the case for the present structure however, which has a ratio closer to 1:1.4.

This structure will be combined with a study performed by neutron diffraction at 2 K by Mr Andrew Farrell, the results of which are expected to be published this year.

[1] Very Intense Vertical Axis Laue DIffractometer

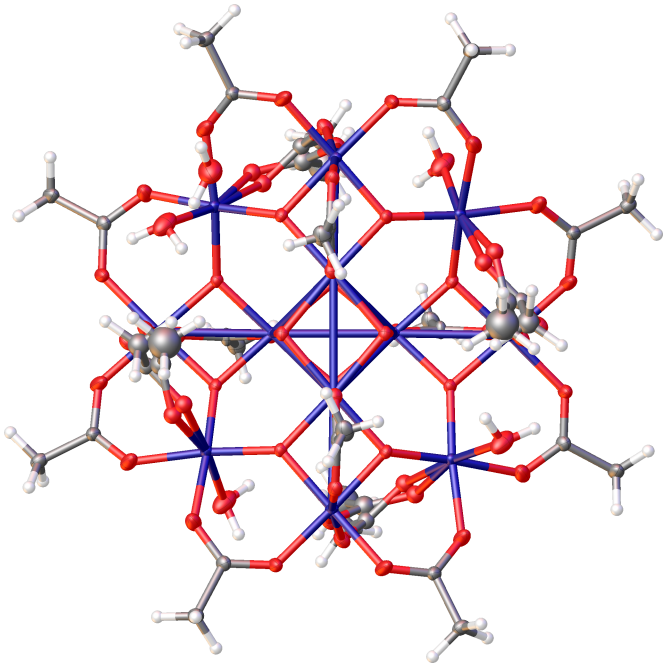

Figure 6.6: The molecular structure of **7** at 2 K, showing the whole cluster. Anisotropic displacement parameters are drawn at the 50% probability level.

Table 6.7: Crystal data and structure refinement of **7** at 2 K.

Empirical formula	$C_{34.84}H_{69.69}Mn_{12}O_{54.84}$
Formula weight (g mol^{-1})	2025.53
Temperature (K)	2.0(1)
Crystal system, space group, Z	tetragonal, $I\bar{4}$, 2
a (Å)	17.1874(6)
c (Å)	12.1721(4)
Volume (Å^3)	3595.7(2)
Calculated density (mg mm^{-3})	1.871
F(000)	2035
Crystal size (mm^3)	1.0 × 0.2 × 0.2
Crystal shape, colour	needle, black
Wavelength λ, Mo K_α (Å)	0.71073
Absorption coefficient μ (mm^{-1})	2.140
Absorption correction type	multi-scan
Ratio min/max transmission	0.8248
Maximum 2θ (°)	52.64
No. of measured reflections	20483
No. of unique reflections	3395
R_{int}	0.0272
R_1, wR_2	0.0282, 0.0747
Data/restraints/parameters	3395/8/261
Goodness-of-fit on F^2	1.047
Largest diff. peak/hole (e Å^{-3})	0.496/−0.347

6.3.2 A Low Temperature Study of a Mn_3 Cluster

The compound $[Mn_3O(Et{-}sao)_3(ClO_4)(MeOH)_3]$ (**8**), where the Et–sao^{2-} ligand is a salicylaldoxime as shown in Figure 6.7, is based on a triangular cluster of manganese(III) (Inglis *et al.*, 2008). The first triangular SMM was reported by Stamatatos *et al.* (2005), based around the same $[Mn_3^{III}O]^{7+}$ centre. This material was thought to show SMM behaviour due to a tridentate ligand forcing the central O atom out of the plane of the three Mn atoms compared to previously reported clusters with planar centres which did not show SMM behaviour.

The aim in synthesising **8** was to produce a family of complexes in which the Mn–O–N–Mn torsion angle could be controlled in the hope of producing more triangular SMMs (Inglis *et al.*, 2009). The substitution of Et in the R–sao^{2-} species reduces the planarity of the ligand compared to R = H and the addition of ClO_4^- further distorts the cluster. This led to a material which features SMM behaviour below ~ 5 K and an X-ray single crystal structure of this compound has been reported at 150 K.

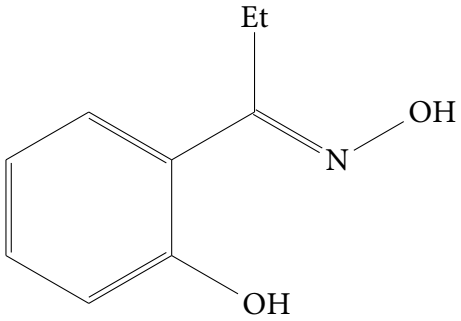

Figure 6.7: The structural formula of the salicylaldoxime ligand, Et–$saoH_2$ = 2-hydroxypropiophenone oxime.

This metal complex crystallises in a trigonal space group, $R\bar{3}$, with ⅓ of a molecule in the asymmetric unit and six molecules in the unit cell. A black cubic crystal was found, each side of which measured 0.25 mm. This was mounted on a graphite fibre as described in Chapter 2, and placed in the Displex with two beryllium vacuum shrouds. The crystal was cooled from room temperature to 2 K at a rate of 1 K min^{-1}.

After remaining at 2 K for several hours to allow the structure to equilibrate, the crystal was centred by diffraction and data were collected. No change in space group was observed upon cooling. The unit cell volume shows a small thermal contraction, decreasing by 164.6 $Å^3$ (3%) from the previously published structure at 150 K. The refinement data are shown in Table 6.8.

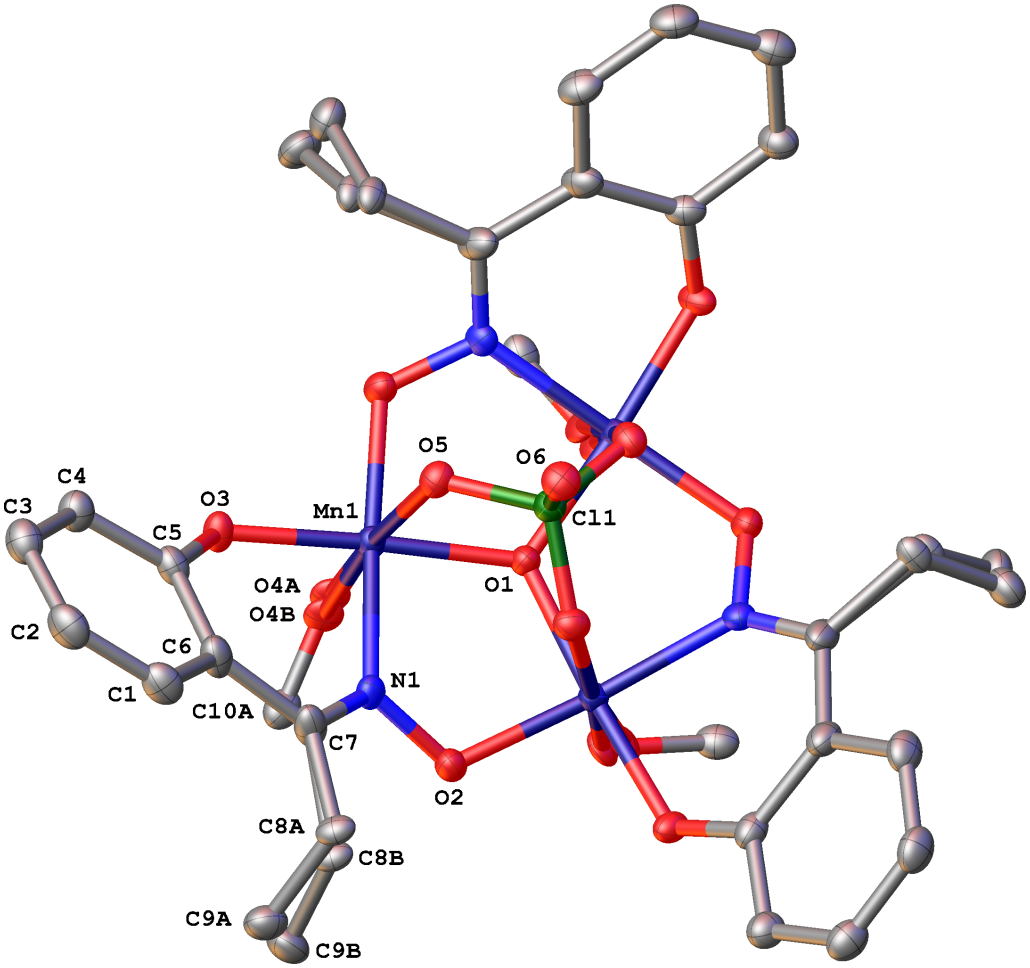

(a) Top-down view.

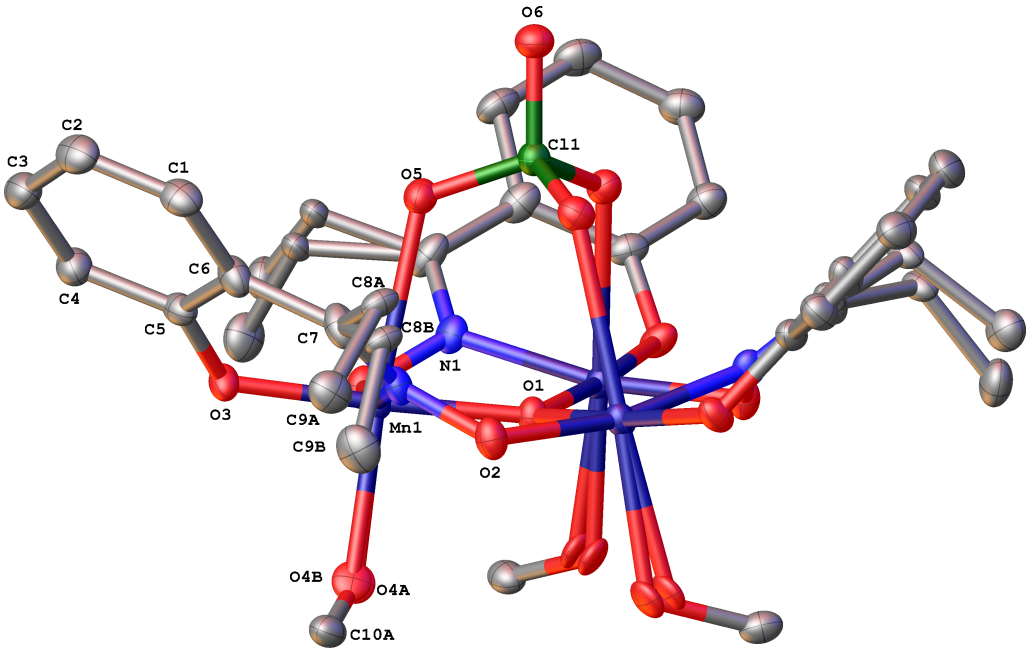

(b) Side view.

Figure 6.8: The molecular structure of **8** at 2 K, showing labels for atoms within the asymmetric unit. Anisotropic displacement parameters are drawn at the 50% probability level. Hydrogen atoms have been omitted for clarity.

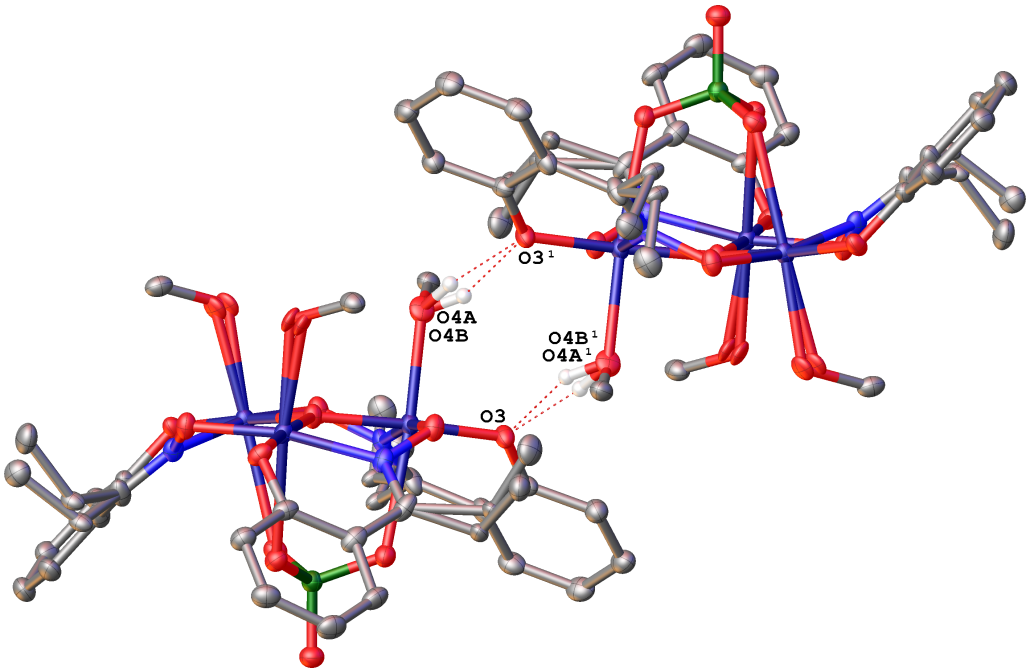

Figure 6.9: A diagram showing selected intermolecular hydrogen bonding in **8** at 2 K. All hydrogen atoms except those involved in the hydrogen bonding have been omitted for clarity. Anisotropic displacement parameters are drawn at the 50% probability level.

Table 6.8: Crystal data and structure refinement of **8**.

Empirical formula	$C_{28.93}H_{36.87}ClMn_3N_3O_{14}$
Formula weight (g mol^{-1})	850.95
Temperature (K)	2.0(1)
Crystal system, space group, Z	trigonal, $R\bar{3}$, 6
a (Å)	13.1815(5)
c (Å)	33.9935(12)
Volume (Å^3)	5115.1(3)
Calculated density (mg mm^{-3})	1.657
F(000)	2613
Crystal size (mm^3)	0.25 × 0.25 × 0.25
Crystal shape, colour	block, black
Wavelength λ, Mo K_α (Å)	0.71073
Absorption coefficient μ (mm^{-1})	1.244
Absorption correction type	multi-scan
Ratio min/max transmission	0.8524
Maximum 2θ (°)	52.78
No. of measured reflections	12696
No. of unique reflections	2256
R_{int}	0.0245
R_1, wR_2	0.0361, 0.0858
Data/restraints/parameters	2256/2/177
Goodness-of-fit on F^2	1.240
Largest diff. peak/hole (e Å^{-3})	0.541/−0.418

The structure was found to be disordered, which has not been previously reported. In the original structure the three methanol groups are each coordinated to a Mn atom. In the structure reported here, however, approximately ⅓ of the methanol groups in the asymmetric unit are replaced by water molecules. This causes a corresponding disorder in the position of the closest methyl group in the adjacent molecule. As there is a three-fold axis through the centre of the molecule, this disorder is present for each methanol group. A view of the entire molecule is shown in Figure 6.8.

The space group assignment does not show any indications of a super-cell or of the $R\bar{3}$ symmetry being broken so the disorder is not only in one position on every molecule. However, because of the nature of a diffraction experiment, the final structure is an average over all the unit cells in the crystal and it is impossible to say whether the disorder is present in only one methanol group in each molecule or if each molecule has anywhere between zero and three methanol moieties being replaced by water.

The intramolecular Mn–O bond lengths are within the range reported by Inglis *et al.* (2008) although the Mn–N–O–Mn torsion angle is slightly larger (42.7(2)˚ at 2 K vs ~ 42.1˚ at 150 K). However, as the unit cell contracts with temperature the intermolecular distances are smaller at 2 K than at 150 K. This is particularly noticeable in the hydrogen bonding between the methanol/water group and the phenolic O atoms, shown in Figure 6.9 and tabulated in Table 6.9. The intramolecular bond distances otherwise remain very similar except for a small reduction in the Mn1–O2 distance.

Table 6.9: Selected bond lengths and atomic distances in **8** at 2 K and 150 K

Bond Distance (Å)	2 K	150 K[a]
Mn1–O1	1.8792(5)	1.8777(3)
Mn1–O2	1.9054(19)	1.8823(10)
Mn1–O5	2.526(2)	2.5497(11)
Mn1–O8	1.8804(19)	1.8823(10)
Mn1–N3	1.991(2)	1.9904(12)
O3–O4A′	2.663(17)	2.734
O3–O4B′	2.81(3)	2.734

[a] Data taken from Inglis *et al.* (2008).

6.3.3 Low Temperature Studies of a Co_4 Citrate Cluster

While there are many known SMMs based on manganese, there are currently relatively few based on cobalt(II). One recent example, $[C(NH_2)_3]_8\{Co_4(citrate)\}.4\,H_2O$ (**9**), was first determined to show SMM behaviour by Galloway *et al.* (2008). A structural study with the Xiphos was undertaken at four temperatures from 100 K to 2 K to determine whether any significant structural changes were observed at low temperatures.

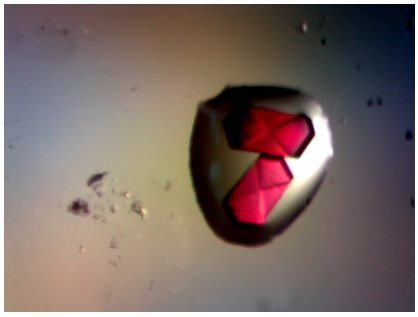

Figure 6.10: Crystals of **9** under polarised light. Image courtesy of Andrew Farrell, University of Glasgow.

The crystals were bright pink in colour and crossed lines were visible on the largest face of all the crystals under polarised light, shown in Figure 6.10. They were generally all of high quality so selecting a crystal for data collection was not difficult. Several were screened first with the Bruker SMART 6K at 120 K, and a full data set was collected using the crystal which was later mounted on the Xiphos.

The molecules crystallise in a tetragonal space group, $P4_2/n$, with ¼ of a molecule in the asymmetric unit and two molecules per unit cell. The crystal used in the following experiments had a lozenge shape and measured $0.35 \times 0.20 \times 0.10\,mm^3$. It was mounted on a graphite fibre as described in Chapter 2, then mounted on the Displex and two beryllium vacuum shrouds attached. The crystal was cooled to 100 K at 1 K/min.

Data were collected at four different temperatures as the crystal was cooled; 100 K, 50 K, 20 K and finally 2 K. No significant changes were observed between these temperatures, as can be seen from the unit cell parameters and volumes in Table 6.10. The largest parameter changes within the molecular structure are the anisotropic displacement parameters.

The diffraction images were also analysed for any changes. It had been thought that some changes might occur, for instance the Bragg peaks becoming broader. Precession images were simulated with *Apex2* at each measured temperature but, as can be seen in Figure 6.12, the diffraction pattern was very similar across the whole range of temperatures, suggesting that there are no changes in the crystal packing over the temperature range studied.

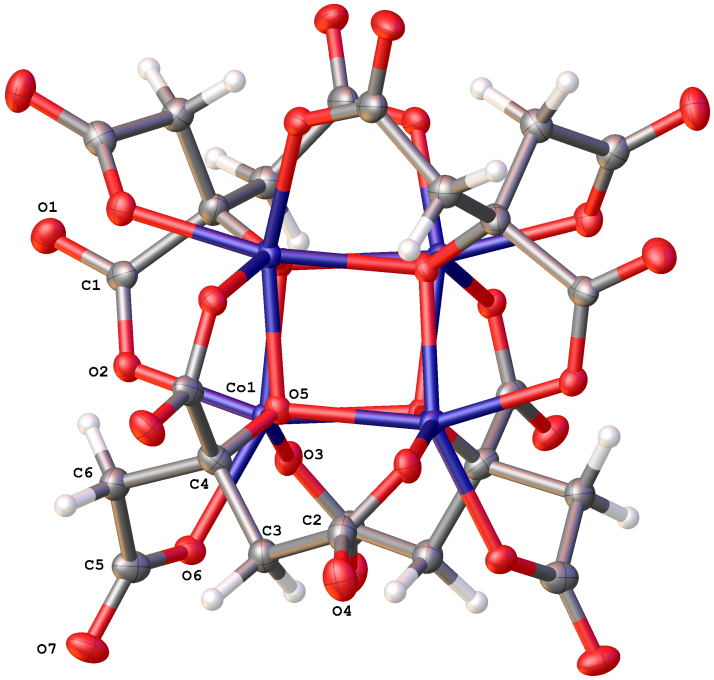

Figure 6.11: The molecular structure of **9** at 2 K, showing labels for atoms within the asymmetric unit. Anisotropic displacement parameters are drawn at the 50% probability level.

Table 6.10: Crystal data and structure refinement of **9** for the four temperatures measured.

Empirical formula	$C_{32}H_{72}Co_4N_{24}O_{32}$			
Formula weight (g mol^{-1})	1540.86			
Crystal system, space group, Z	tetragonal, $P4_2/n$, 2			
Crystal size (mm^3)	0.35 × 0.20 × 0.10			
Crystal shape, colour	block, clear pink			
Wavelength λ, Mo K$_\alpha$ (Å)	0.71073			
Temperature (K)	2.0(1)	20.0(1)	50.0(1)	100.0(1)
a (Å)	16.1149(6)	16.1115(7)	16.1107(6)	16.1128(5)
c (Å)	11.5251(4)	11.5229(5)	11.5238(4)	11.5299(4)
Volume (Å^3)	2992.95(19)	2991.1(2)	2991.06(19)	2993.42(17)
Calculated density (mg mm^{-3})	1.710	1.711	1.711	1.710
F(000)	1592	1592	1592	1592
Absorption coefficient μ (mm^{-1})	1.200	1.201	1.201	1.200
Absorption correction type	multi-scan	multi-scan	multi-scan	multi-scan
Ratio min/max transmission	0.8954	0.8532	0.8967	0.8983
Maximum 2θ (°)	52.68	52.7	52.7	52.72
No. of measured reflections	19380	19325	19381	17838
No. of unique reflections	3052	3052	3051	3053
R_{int}	0.0310	0.0350	0.0305	0.0368
R_1	0.0388	0.0394	0.0388	0.0397
wR_2	0.0883	0.0917	0.0887	0.0955
Data/restraints/parameters	3052/0/211	3052/0/211	3051/0/211	3053/0/211
Goodness-of-fit on F^2	1.052	1.047	1.036	1.040
Largest diff. peak (e Å^{-3})	0.835	0.798	0.800	0.751
Largest diff. hole (e Å^{-3})	−0.361	−0.404	−0.354	−0.324

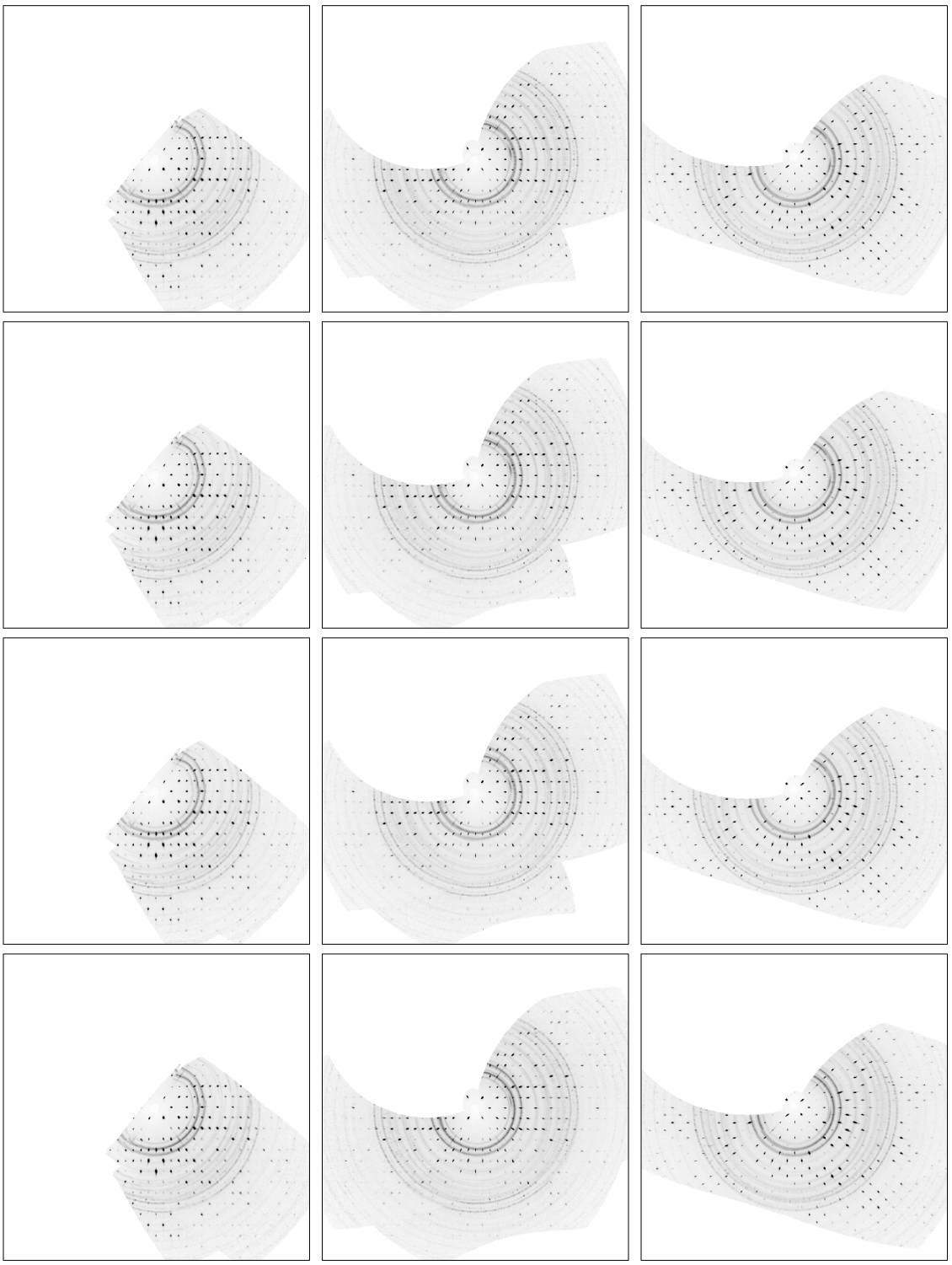

(a) 0*kl* (b) *h*0*l* (c) *hk*0

Figure 6.12: Simulated precession images generated by *Apex2* showing three zones over the four temperatures measured, from 2 K at the top to 100 K in the bottom row.

6.3.4 Conclusions

Structural studies of **7** and **8** have been performed at 2 K with the XIPHOS to complement neutron studies at the same temperatures performed by Mr Andrew Farrell. Accurate unit cell parameters from X-ray data were required for use with the data from VIVALDI, a multi-wavelength Laue diffractometer, as well as to provide high-quality structural data.

The structures of both **7** and **8** have been found to be very similar to previously published structures at higher temperatures although some differences were found, chiefly regarding structure disorder. A MeCOOH solvent in **7** is found to occupy two positions over a centre of symmetry and previous studies have refined each with an average occupancy of 0.5. In the current study, the occupancy of each position was found to refine to a lower value of 0.35, which also matched the occupancy of the minority component of an adjacent disordered $MeCOO^-$ ligand within the cluster.

The Mn_3 cluster, **8**, shows small differences in intermolecular bond distances at 2 K from the previously published study at 150 K and also shows disorder in one of the groups involved in hydrogen bonding between adjacent clusters that has not previously been reported. Small changes in bond lengths, particularly out of the plane of the Mn_3 centre, have also been found, although it is not clear if these are due to changes connected with the onset of SMM behaviour or are due to thermal contraction below 150 K.

Finally, structural studies of **9** were performed at 100 K, 50 K, 20 K and 2 K. No changes in the space group were observed over the temperature range and the unit cell parameters change remarkably little between 100 K and 2 K. In addition, no broadening of the Bragg peaks was seen over the temperature range. The SMM behaviour at very low temperatures can therefore not be explained by any changes to the solid state structure of the material.

Chapter 7

Ancillary Programs

7.1 Xiphos Tools

The Xiphos diffractometer uses software written by Bruker AXS to collect and process reflection data. This includes *BIS* and *Apex2*, which can be used to centre a crystal, index the unit cell, collect and integrate data and even to solve and refine the structure using *SHELXS* and *SHELXL*(Sheldrick, 2008a).

There are however experimental requirements that are not covered by this collection of software. This includes interfacing with additional hardware such as the Displex cryo-refrigerator or viewing machine status remotely. Fortunately *BIS* has been designed so that additional software can be written to interact with the Bruker software, provided that this software uses the correct communication protocols.

7.1.1 BIS

Modern Bruker diffractometers use the *Apex2* software suite to control data collection and processing. However, *Apex2* does not directly connect to the hardware but connects to the intermediate program called *BIS* (Bruker Information Service). *BIS* connects to the hardware using serial connections, and accepts connections over TCP/IP connections. This allows *Apex2* or other programmes to interact with the hardware from a remote computer as well as the one on which *BIS* is running.

BIS uses text strings for communication, both for sending and receiving messages. These messages use ASCII text encoding and consist of a command with optional arguments, surrounded by square brackets.

```
[CommandName /Argument=Value]
```

The command name is a single word without spaces, as is the argument name, but the argument value can have spaces and continues until either another argument is found or a closing square bracket ‘]’ is seen, to signal the end of the message.

There are three sockets to connect to in order to communicate with *BIS*: a command socket on port 49153 (where requests are sent from clients and acknowledgements received), a file socket on port 49154 which is not normally used and a status socket on port 49155 (from which updates about the machine status are continually sent). It should be noted that these ports are used by the operating system in Microsoft® Windows® 7 so these port numbers may change in the future.

All messages sent to the command socket must be terminated by a line-feed character (‘\n’). There are four possible responses which *BIS* may send back through this command socket, which begin with the command name that was sent, followed by an underscore and YES, NO, DONE or SKIPPED. The first two are immediate responses to a command, and whether it was recognised or not. The other two may be sent later when a command is processed but are not often seen.

The status socket does not accept incoming communication but continually sends messages regarding the current instrument status. These cover all aspects of the instrument, such as the generator power, diffractometer angle positions, goniometer movements, shutter status, sample temperature and more. Many of these messages are sent with no interaction required but items which are not sent automatically may be requested by sending an appropriate message to the command socket.

7.1.2 libbis

The use of network sockets increases the flexibility of the Bruker software suite by allowing programs to connect to *BIS* from computers that are not connected to the instrument hardware. This does, however, come at a cost as there are pitfalls associated with network programming. The code must be able to cope with slow or broken connections without affecting the user interface. This means that all network code must be running in a separate thread or using asynchronous methods if these are available. Another possibility that must be considered is the loss of messages, either wholly or in part, or the potential effects of unintentionally connecting to a malicious server.

As the programs detailed below all connect to *BIS*, they share a library of code that has been written for communication with *BIS*. This includes a `BisString` class, which parses

a message sent from *BIS* into a command name and a list of arguments, each containing the argument name and the supplied value. It also constructs valid messages given a command name and arguments to be associated with it.

The library also includes the `BisThread` class, which is responsible for opening and maintaining the network connections to *BIS*. This creates a new thread, allowing it to operate continuously while the program in which it is running can run other operations simultaneously. As all the programs detailed here run over long periods of time (especially *Bis2Shore* and *XiSpy* which are designed to run for months at a time without human input) this thread constantly monitors whether the sockets are still connected and attempts to reconnect if they are not. This allows these programs to continue working in case of network interruptions or even if the *BIS* stops running and later restarts.

7.1.3 Bis2Shore

With X-ray diffraction experiments taking several hours or more to complete, it is desirable to know that the temperature of the sample has been stable over the whole experiment. In the Bruker frame headers there is an item for recording the sample temperature which is written by *BIS* during the experiment. There is a corresponding command that can be sent to *BIS* to report the sample temperature, originally used by the Kryoflex (another piece of Bruker equipment).

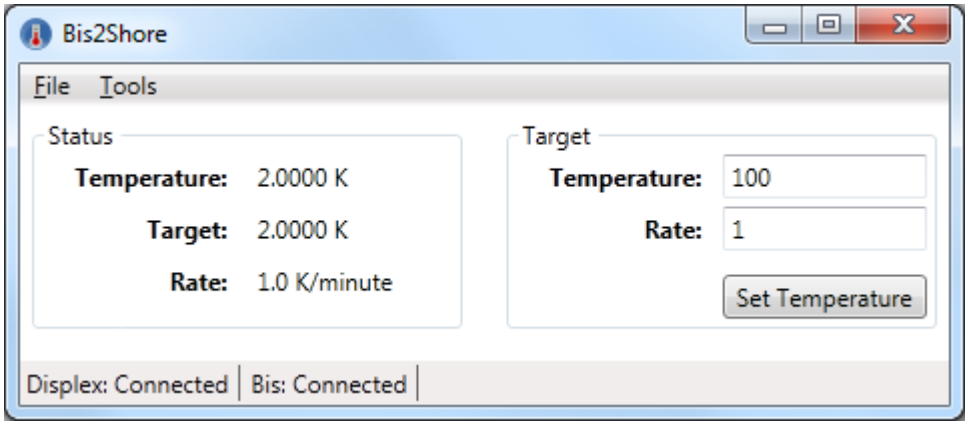

Figure 7.1: The main *Bis2Shore* interface.

7.1.3.1 LakeShore Controller

The Displex is attached by a LakeShore® Model 340 temperature controller, which can be connected to a computer *via* an RS232 serial port. As with *BIS*, various commands can be

sent and replies received about the status of the Displex. A program called *Bis2Shore* has therefore been written to bridge these components and report the sample temperature in every frame header.

The Displex uses a balance of heating and cooling to maintain a particular temperature once the set temperature has been reached. Due to the range of temperatures that can be reached there are several heater powers available, each designed to operate within a particular temperature range.

Bis2Shore sends queries to the LakeShore controller at regular and configurable intervals, requesting the actual sample temperature, the requested temperature, the rate at which the requested temperature changes (the ramp rate) and the heater power and output percentage. Although *BIS* can only record the sample temperature, the other items are useful as they can be displayed in the program GUI and also logged separately.

The LakeShore controller uses a simpler and more compact format for messages through the serial port. The message uses a short name, for example `KRDG?`, which requests the sample temperature in Kelvin, with any arguments separated by commas. The message is terminated by a character sequence which can be chosen from one of the following: `CR`, `LF`, `CR/LF` or `LF/CR`, where `CR` is a carriage return (\r) and LF is a line-feed (\n). All messages are encoded in ASCII. The messages used by *Bis2Shore* are shown in Table 7.1.

Table 7.1: The commands used by *Bis2Shore* to communicate with the LakeShore controller.

Command	Response	Notes
`KRDG? <input>`	`<temperature>`	Actual sample temperature (K)
`SETP? <loop>`	`<temperature>`	Requested sample temperature (K)
`RAMP? <loop>`	`0`	Ramping is disabled
	`1, <rate>`	Ramp rate (K/min)
`RANGE?`	`0`	Heater is off
	`<index>`	Index representing heater power
`HTR?`	`<output>`	Heater output (%)
`RAMP <loop>, 1, <rate>`	*none*	Set ramp rate
`SETP <loop>, <kelvin>`	*none*	Set temperature

The LakeShore controller requires that messages be sent no less than 50 ms apart. Multiple messages that do not request an answer may be combined in one message with a ';' character between them but any message to which the controller will send a reply must be the last in such a chain or sent separately.

Using this mechanism the LakeShore may also be controlled remotely. The primary task for *Bis2Shore* is to report the sample temperature but it may also be used to change the temperature without physically accessing the conntroller. *Bis2Shore* only uses a limited set of

commands to change the set-point and the ramp rate, but there are many more commands which can be sent to the LakeShore which are not used here.

7.1.3.2 Program Execution

Bis2Shore is a graphical program written in C# to run on the Windows® operating system. As *Bis2Shore* is designed to run for long periods of time without user input it has been designed to minimise to the system tray in Windows when the main window is minimised or closed.

There are several components: the main thread which runs the user interface, the *BIS* thread which is responsible for all communication with *BIS* and a third thread (the 'back-end' thread) which performs the program logic, including communicating with the LakeShore controller. This backend thread runs continuously and directs the program's actions depending on the time that has passed and the user specified intervals between updating the Displex status, sending the temperature to *BIS* and writing the log file.

All communication with the LakeShore is handled through a *Displex* class, which is responsible for setting up the serial connection and all communication, including the enforcement of the minimum time between sending commands to the controller. All communication occurs synchronously so if a reply is requested the thread will wait until the reply is received, unless there is a problem with the connection and a timeout is triggered. As this occurs in a separate thread from the user interface, the user will not notice any loss in responsiveness in the case of communication problems, yet the code is much simpler than attempting to use asynchronous connections.

At intervals specified by the user, *Bis2Shore* will send the current temperature to *BIS*. This is done through the use of the following command:

```
[SAMPLETEMPERATURESTATUS /DEGREESC=<temperature>]
```

Despite most interactions with the sample temperature using Kelvin, the temperature is sent to *BIS* in Celcius after it was found that the temperature was misinterpreted when attempting to use the `DEGREESK` argument.

Log files are also written containing all the information requested from the controller, using a simple comma-separated-value format. The log file is changed every day so that the log does not become too large to manage and also allows easy removal or archiving of old logs. Each line starts with the time at which the line was added to the file, the temperature, setpoint, heater output and heater range. This format can be easily read by other software, allowing the sample temperature to be viewed graphically using Excel, for example.

Another file is also written to the same directory called `current_temperature.log`, containing only the latest status. This is used by *XiSpy* (see Section 7.1.5).

7.1.4 Ramp

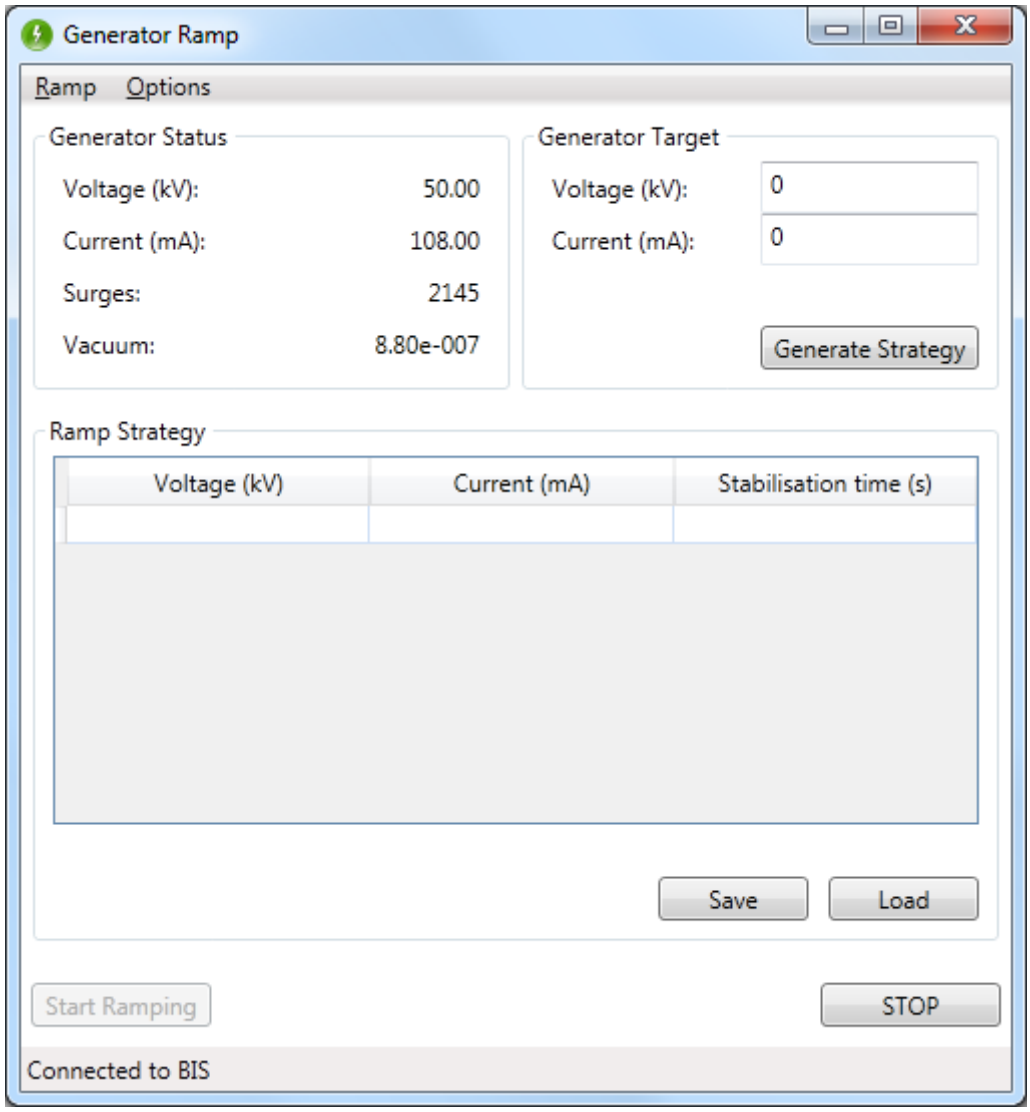

Figure 7.2: The main *Ramp* interface, before strategy generation.

The XIPHOS uses a rotating-anode X-ray generator that must be powered up slowly, in a series of steps. This is time consuming and error-prone to do manually and can be automated by sending commands to *BIS*.

The programme that was written for this purpose is called '*Ramp*' and is written in C#. It runs in two stages. The first is to generate a series of power settings between the current power setting and the target which *Ramp* will step through. This is known as the 'strategy'. The second is to run through this strategy and to respond to changes in the machine status.

7.1.4.1 Strategy Generation

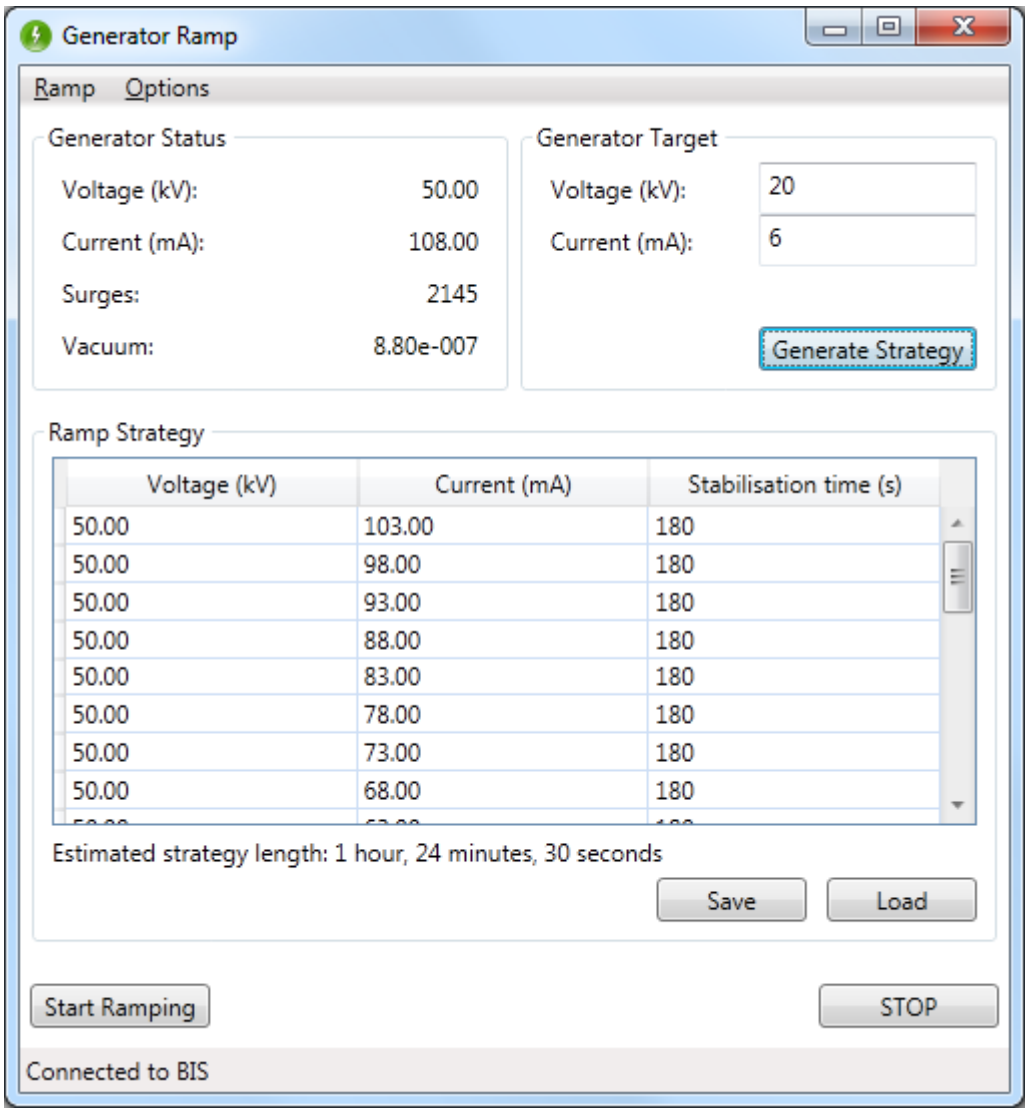

Figure 7.3: The main *Ramp* interface, after a strategy has been generated to power down the generator.

When powering up the generator the strategy generation is simple. The voltage and the current are increased in alternating steps, the default size of these steps being determined by the user. When one of these reaches the desired value, the other continues increasing in steps until it too reaches the target. The generator standby settings for the XIPHOS are 20 kV and 6 mA, so by increasing the current first and then the voltage in alternating steps, all the intermediate values on the way to the target are also safe for the generator. An example strategy to power the generator from standby to 40 kV and 30 mA with default step sizes of 5 kV and 5 mA, is shown in Table 7.2.

Table 7.2: Example strategy generated to power the generator from standby to 40 kV and 30 mA, with step sizes of 5 kV and 5 mA. The current and voltage shown are the targets, after the action specified has been taken.

Step number	Voltage (kV)	Current (mA)	Action taken
1	20	11	Increase current by 5 mA
2	25	11	Increase voltage by 5 kV
3	25	16	Increase current by 5 mA
4	30	16	Increase voltage by 5 kV
5	30	21	Increase current by 5 mA
6	35	21	Increase voltage by 5 kV
7	35	26	Increase current by 5 mA
8	40	26	Increase voltage by 5 kV
9	40	30	Increase current by 4 mA

A different algorithm must be used when powering down the generator, however. The maximum power setting is 5.4 kW, which corresponds to a setting of 50 kV and 108 mA. A strategy generated by reducing the current by 5 mA and the voltage by 5 kV per step until one reached the target would leave the generator at a setting of 20 kV and 73 mA at one intermediate step, which would put unnecessary stress on the filament.

Therefore when powering down the generator the current should be lowered in stages until the value in mA is lower than the voltage in kV and only then should both be decreased. An example of this can be seen in Figure 7.3, where the current is reduced but the voltage remains the same until the current drops below 50 mA. At that point the current and voltage will both be reduced in alternating steps.

Once the strategy has been generated it is presented to the user for approval. Each step can be modified or removed if desired, to increase the time spent stabilising at a particular step before moving to the next, or to remove steps if larger voltage or current increments are required.

7.1.4.2 Execution

If the strategy is accepted, *Ramp* can start sending the first power change request to *BIS*. The command is of the form shown below.

```
[SetGeneratorStatus /MA=<current> /KV=<voltage>]
```

BIS will then respond with status messages as the power is changed, of the following form:

```
[GENERATORSTATUS /MA=<current> /KV=<voltage>]
```

When the requested power is reached, *BIS* will respond with a different status message:

```
[SETGENERATORSTATUS /MA=<current> /KV=<voltage> /DONE=1]
```

When this message is received *Ramp* switches state to wait for the end of the stabilisation period associated with this step of the strategy. It will also listen for status messages from *BIS* containing the number of generator surges. When the stabilisation period has finished, the number of surges recorded during the time are calculated.

When the generator surges, the hardware automatically cuts the power and then attempts to bring the power back to the level at which it was before the surge. If the generator surges more than once in a short period of time (*e.g.* a few minutes) this indicates that the generator is unstable at this power setting and the power should not be increased further until the surges decrease in frequency or stop.

If the power to the generator is being increased by the ramp strategy, the number of surges is counted during the stabilisation period. If none are recorded, *Ramp* will move to the next step. If one or two surges are observed, the stabilisation period is repeated again until no surges are recorded during that stabilisation period. If this occurs five times consecutively or more than two surges are recorded during stabilisation, the generator power is reduced to that specified in the previous step. This continues until the last step is completed unless the generator is so unstable as to reach the first step again, at which point *Ramp* will abort the attempt.

7.1.5 XiSpy

It is often useful to be able to see how a data collection is progressing when away from the diffractometer, especially in the case of a new machine in development such as the Xiphos. This allows users to quickly determine when a data collection will finish and if there are any problems with the crystal or the equipment that might require the operator to return. This is made possible as *BIS* continually reports the machine status and additional status items can be requested by sending commands if required.

Periodically an HTML file is generated from the received status information and this is then copied to a remote web-server using the widely-used `SSH` protocol. This ensures the separation between the computer controlling the diffractometer and the wider internet and removes the need for more complex security which would be required if the controlling computer were directly connected to the internet. An example of the status page produced is shown in Figure 7.6.

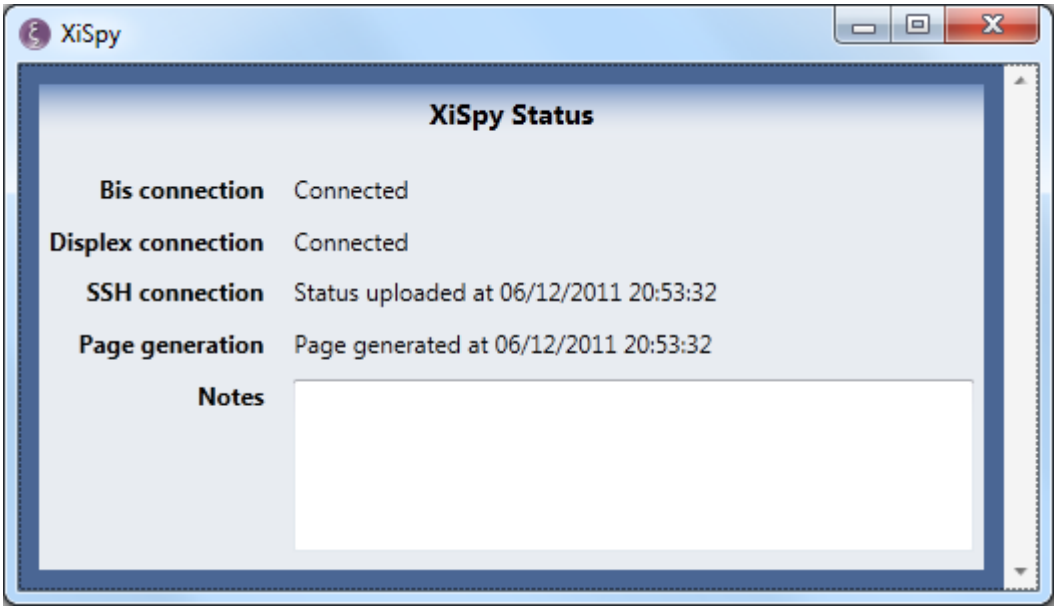

Figure 7.4: The main *XiSpy* interface.

The status messages which *XiSpy* responds to are listed in Table 7.3. Different versions of *BIS* may use different commands for relaying the same information, which is why several different status messages are used for the detector distance or CCD temperature, for example. Any of the messages that *BIS* sends out which are not recognised by *XiSpy* are ignored.

Table 7.3: The status messages sent by *BIS* which are used by *XiSpy* to display the machine status.

Information	Command name	Arguments
Generator power	`GENERATORSTATUS`	`/KV /MA /STANDBY` *(optional)*
Goniometer angles	`ANGLESTATUS`	`/ANGLES /DISTANCE` *(optional)*
Crystal temperature	`SAMPLETEMPERATURE`	`/DEGREESC` *or* `/TEMPC`
CCD temperature	`CCDTEMPERATURE`	`/DEGREESC`
CCD temperature	`DETECTORSTATUS`	`/CCDTEMP`
Detector distance	`DISTANCESTATUS`	`/DISTANCE`
Collection status	`ACQUISITIONSTATUS`	`/ACQUIREDFRAMES /REMAININGFRAMES /ELAPSEDSECONDS /REMAININGSECONDS`
Collection status	`SCAN_YES`	`/RUNNUMBER /FRAMENUMBER`
Machine status	`INSTRUMENTSTATUS`	`/BUSY /XRAYSON`
Instrument processing	`INSTRUMENTQUEUE`	`/PROCESSING` *(optional)*
Image file, warnings	`MESSAGE`	`/NOTE /LEVEL`

Once a status message is received it is passed to a particular function to extract the useful information and is then saved together with the time at which the message was received. This is useful for the user to determine whether the information is out of date but is also necessary to display the estimated time at which the data collection is finished. Only the

number of seconds remaining is reported as part of the `ACQUISITIONSTATUS` message so this must be added to the current time to obtain a more useful value.

BIS sends status messages constantly and when data are being collected this can result in many messages every second. In order to handle this volume of messages and to keep the GUI responsive in case of network errors, all communication with *BIS* is conducted in a separate thread to the rest of the program. This simplifies the network programming by allowing synchronous communication in which the thread can do nothing while waiting for a network communication to finish. In normal operation these calls should finish almost instantaneously but if a network error occurs the thread may end up waiting multiple seconds for a timeout to occur. The trade-off for this simplicity is that locking must be implemented such that the thread responsible for generating the HTML page and the *BIS* communication thread do not attempt to access the same information simultaneously.

7.1.5.1 Displex Temperature

Although the Displex temperature is reported to *BIS* with *Bis2Shore* and can therefore be accessed by *XiSpy*, there are other useful pieces of information which can be provided by the LakeShore controller which cannot be accessed through *BIS* in this way. However this information cannot be requested directly from the LakeShore either, as *Bis2Shore* will be running during data collections and a serial port connection can only be used by one program at once.

To solve this, *Bis2Shore* writes a file at a specified interval containing the current Displex status. The file uses a very simple comma-separated value (CSV) format containing the current temperature, the requested temperature, the heater output as a percentage and the current heater being used. Reporting the heater output may show any loss of cooling power in the Displex that may disrupt the experiment.

7.1.5.2 Recent Frame

It may be useful to know the status of the sample itself, to check that the crystal has not degraded, or fallen off the mount during the data collection. This has been implemented in *XiSpy* by including a recent diffraction image. There are several important considerations to this approach, however. If the machine status is publically visible, it may be possible for a malicious user to download these images and with the other information available from *XiSpy*, it may be possible to crudely integrate the spots on the image. Although the data quality will not be good, it may even be possible to solve the structure by assigning spot

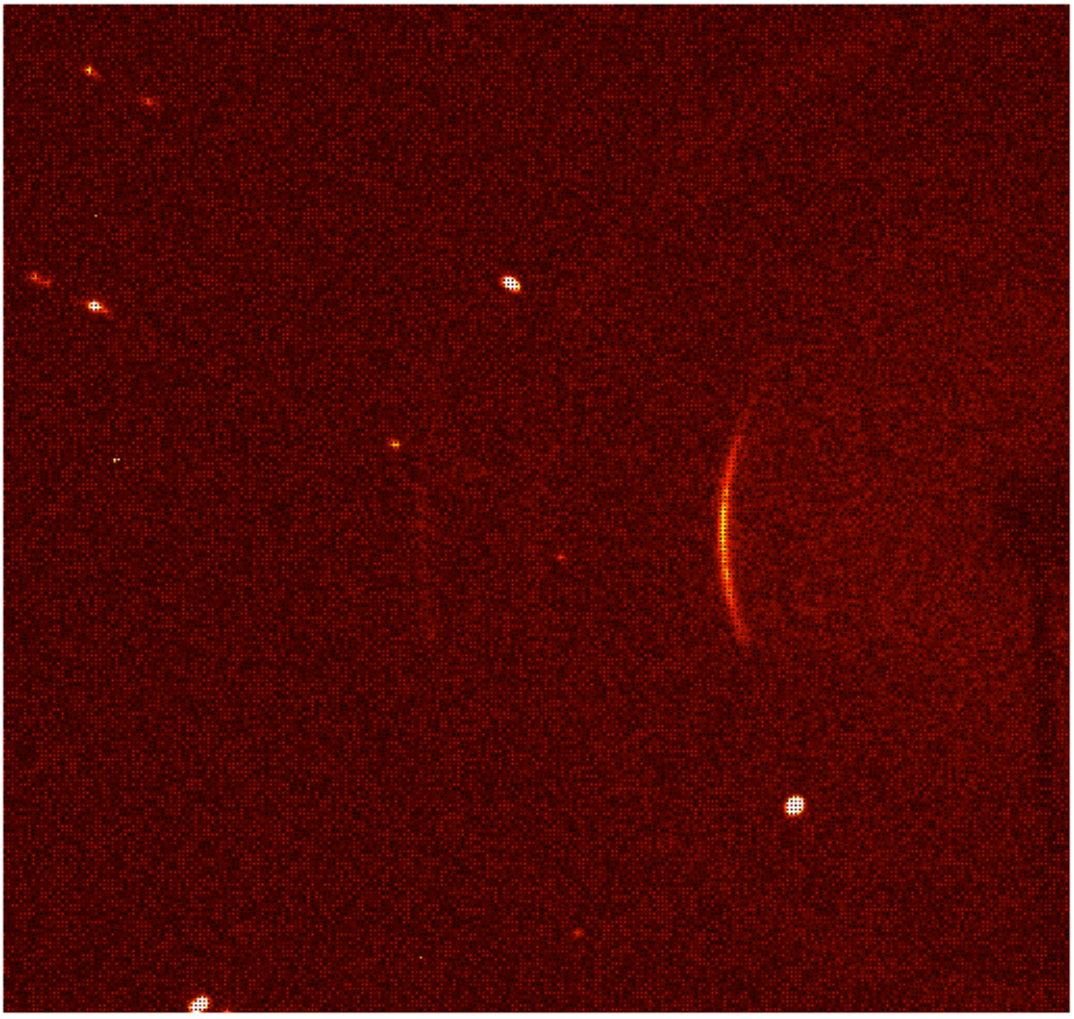

Figure 7.5: An example image produced during a data collection by *XiSpy*, showing the pattern of random pixel values. The diffraction pattern is still visible, showing that the crystal is still in place and diffracting well, but accurate extraction of reflection intensities is made much more difficult.

intensity as 'strong', 'medium' or 'weak'.

There are several methods designed to counteract this implemented in *XiSpy*. One of these is to include random data within the image. As the image is generated from the diffraction frame, there is a linear correspondence between colour values and spot intensity, up to a certain cut-off. By assigning random values to some of the pixels in the image this correlation between colour and intensity may be disrupted, making it more difficult to automatically integrate these images. An example image is shown in Figure 7.5.

Another feature is that the image chosen to display does not necessarily correspond to the goniometer angles shown. As each frame is collected, *BIS* sends out a status message containing the file name. However in *XiSpy* this has only a 10% chance of being recorded.

XIPHOS Status

Last generated at 09/05/2011 09:58:48

BIS

Item	Status	Last Updated
Generator status	50.0 kV, 108.0 mA	09/05/2011 09:57:50
Angles	2θ: 20.00°, ω: 30.00°, χ: 180.00°, φ: 256.50°	09/05/2011 09:58:45
Detector distance	8.00 cm	09/05/2011 09:58:45
Sample temperature	289.83 K	09/05/2011 09:58:46
CCD temperature	-58.91°C	09/05/2011 09:58:46
Frame number	Frame 13, run 1 (5347 frames remaining)	09/05/2011 09:58:46
Collection started	09/05/2011 09:56:47	09/05/2011 09:58:46
Estimated finish	09/05/2011 17:44:55	09/05/2011 09:58:46

Recent frame Show/Hide

Displex

Item	Status	Last Updated
Temperature	289.8320 K	09/05/2011 09:58:09
Set point	3.0000 K	09/05/2011 09:58:09

Figure 7.6: An example of the status page generated during a data collection by *XiSpy*.

As such, the image displayed when the status is uploaded to the web server is unlikely to correspond to the angles shown.

7.1.5.3 Status Page Generation

XiSpy uses three threads in general operation: one thread for the user interface, one for *BIS* communication and a third thread for generating the status pages. This thread does nothing except wait for the majority of the time, until it awakens to read the status from *BIS* and *Bis2Shore*. At this point the thread copies the status from the *BIS* thread and if it has been enabled, attempts to read the status file written by *Bis2Shore* (see below). This operation takes very little time so does not require a new thread. A function builds the status page in HTML format as a string, putting the status in a table along with the time at which the status was read. Each row of the table is formatted separately, depending on what information it contains. Warnings are displayed if *XiSpy* is not currently connected to *BIS* or if the Displex temperature file is too old or non-present. If data is being collected, the frame image described above is also included.

Warning and error messages are displayed below the table in case *BIS* has reported any of these. These can encompass a variety of information, ranging from hardware collisions to information such as generator surges or that the detector distance has changed during the data collection. These messages can be important if the data collection has stopped unexpectedly to determine whether immediate action needs to be taken or not.

Finally, there is an area in the program user interface where comments may be written. If any comments are present these are written to the end of the status page. This is optional, but may be useful to indicate any action taken by one person if multiple people are monitoring the machine status, so that only one person must be present to examine the instrument physically in case of a fault.

Once the HTML page has been generated in memory, it is copied across the network to a file on a remote web-server using the *SSH*, with a username and password supplied by the user. The recent frame image is also copied at the same time if desired. The time at which the page was generated is present so that it can be seen if the status is recent or if it may contain outdated information. An example of the status page generated is shown in Figure 7.6.

7.2 libcrystal

A library of code written in C++ has also been built. This is used by *Masquerade*, for example, as well as a number of the other small utility programs which have been written for specific needs. While C# is useful for writing GUI programs or other software which is not particularly CPU intensive, for programs which do a lot of calculations it may not be the best choice. A version of *Masquerade* was originally written in C# but generating masks for an experiment took several hours, rather than the few minutes the C++ version takes.

The code library has the name *libcrystal* and is designed to be small, light-weight and not depend on large external libraries. There is code for simple calculations on unit cells, space groups and diffraction geometry; code for reading a variety of file formats which have been encountered, such as *SHELX hkl* files or Bruker formats such as *raw* and *P4P* files as well as old- or new-style diffraction images.

The code is written in portable C++ with as little dependence on a particular operating system or compiler as possible. It compiles on 32- and 64-bit platforms and has been used on Windows®, Mac OS X® and Linux®.

7.2.1 Space Groups

When writing code dealing with crystal structures or reflection data, the crystal space group may play an important role. The code described in this section was written to provide the symmetry operations of any space group, given only the space group name.

7.2.1.1 Background

Symmetry operations equate two points in three dimensional space and can be described in terms of a rotation and a translation operation. This can be represented mathematically by a 4×4 matrix, known as a Seitz matrix (Shmueli, 1993). Various representations are shown in Equation 7.1 below.

$$S = \left(\begin{array}{ccc|c} r_{11} & r_{12} & r_{13} & t_1 \\ r_{21} & r_{22} & r_{23} & t_2 \\ r_{31} & r_{32} & r_{33} & t_3 \\ \hline 0 & 0 & 0 & 1 \end{array}\right) = \begin{bmatrix} \mathbf{R} & \mathbf{t} \\ 0 & 1 \end{bmatrix} = \{\mathbf{R}/\mathbf{t}\} = (\mathbf{W}, \mathbf{w}) \tag{7.1}$$

The matrix $\mathbf{R}$ describes the rotation function, where r_{ij} is either 0, 1 or -1. The vector $\mathbf{t}$ describes the translation operation, where t_k is a fraction of the unit cell. This can have the value 0, ⅙, ¼, ⅓, ½, ⅔, ¾ or ⅚.

From these matrices both systematic absences and equivalent reflections can be calculated. Equivalent reflections are found from the transpose of the rotation matrix, where $\mathbf{h}$ is an *hkl* index as a column vector:

$$\mathbf{h}' = \mathbf{R}^T\mathbf{h} \tag{7.2}$$

There are several ways to input the space group information into a program. One is to specify the Seitz matrices manually (albeit in a more compact representation) and this approach is implemented in *SHELX*. This is cumbersome and potentially error prone for the user, especially for large space groups where there can be up to 192 symmetry operations. Another approach is to store a list of Seitz matrices for each space group and look them up when given a space group name or number, as implemented in *OpenBabel* (O'Boyle *et al.*, 2011). This uses a larger amount of storage space and is not able to handle any alternative space group settings that have not been programmed in beforehand.

A more appealing alternative is to generate the symmetry operations from the space group symbol itself, for which Hall space group symbols were designed (Hall, 1981). These symbols are designed to be unambiguous and allow all the symmetry operations making up

the space group to be generated from the name alone.

The symbols have the following form, where the square brackets represent optional components:

$$L[N_T^A][N_T^A][N_T^A]$$

Each part of the symbol specifies one or more Seitz matrices. The lattice symbol, L, is associated only with translational elements, so the rotation matrices for each are the identity matrix, I. If the space group has a centre of inversion the symbol is given an overbar, $\overline{L}$, and each translation is also associated with $-I$.

The remaining symbols, N_T^A, each describe one Seitz matrix. N^A describes a rotation matrix with order of rotation N about axis A. The axis symbols can be x, y, z, $'$, $''$ or $*$, to specify rotations about the a, b, c, $a+b$, $a-b$ and $a+b+c$ directions respectively. All rotations are in the clockwise direction. As with the lattice symbol, N can be either a positive integer, specifying a proper rotation, or a negative integer, specifying an improper rotation.

T describes the translation vector and uses either numerical symbols, which specify translations as a fraction of the rotation order in the specified axis direction, or the alphabetic symbols a, b, c, n, u, v, w and d which specify translations in fixed directions, given by Hall (1981). A combination of these alphabetic symbols can be used, in which case the translation vectors specified by each are added together.

The Seitz matrices specified explicitly by the Hall symbol are the minimum subset required to generate the complete symmetry information. Multiplying one Seitz matrix by another gives a third matrix as a product, which itself describes a symmetry operation. The complete symmetry of the space group is generated by multiplying the original matrices with the new product to give more Seitz matrices and this process continues until the only new matrices produced are duplicates of those already present.

7.2.1.2 Code

The code in `libcrystal` uses a 3×3 integer matrix to store the rotation and a 3 dimensional vector to store the translation for each Seitz matrix. Although the translation vector has fractional components, it is simple to convert each to an integer by multiplying by 12. As floating point numbers in computers can only represent a finite set of values, rounding errors may accumulate if integers are not used. Separating the rotation and translation like this rather than using a 4×4 matrix simplifies the logic when only the rotation or only the translation is required, while making multiplying the symmetry operations only slightly more complicated.

Listing 7.1: Using the `SpaceGroup` and `SymmetryOperation` classes with *hkl* indices.

```
SpaceGroup sg("P 21/c");  // Names default to H-M symbols.

printf("Hall symbol: %s\n", sg.hallName());
printf("Number of symmetry operations: %d\n", sg.numOperations());

std::list<HKL>::const_iterator iter;
for (iter = hkls.begin(); iter != hkls.end(); hkls++) {
  const HKL &hkl = *iter;

  printf("HKL indices: %d %d %d\n", hkl.h(), hkl.k(), hkl.l());
  printf("Absent? %s\n", sg.isAbsent(hkl) ? "Yes" : "No");

  std::vector<SymmetryOperation> symops = sg.symmetryOperations();
  std::vector<SymmetryOperation>::const_iter sym;

  printf("Equivalent reflections:\n");
  for (sym = symops.begin(); sym != symops.end(); sym++) {
    HKL equiv = sym->equivalentIndex(hkl);
    printf("  %d %d %d\n", equiv.h(), equiv.k(), equiv.l());
  }
}
```

A space group class is provided that will generate the complete set of symmetry operations when given a Hall symbol. As these are still less common than the Hermann-Mauguin symbols, a translation table is also provided which contains the Hall symbols for a total of 530 common standard and non-standard Hermann-Mauguin symbols, as listed in the International Tables. In testing, all the symmetry operations of all 530 space groups were generated in less than a second, so this process is almost instantaneous for a selected space group.

Once the symmetry operations have been generated, the class can be used to perform several useful transformations. It can be used to determine whether a given *hkl* index should be systematically absent, list the symmetrically equivalent *hkl* indices and generate symmetrically equivalent fractional coordinates within a unit cell. An example is shown in Listing 7.1.

7.2.2 Goniometer Calculations

For some applications it is necessary to be able to convert from a pixel position on the detector to an *hkl* index and vice-versa. The ability to calculate the $\mathbf{S}_1$ vector from a detector

position to the crystal is also a requirement for *Masquerade*.

A `Detector` class contains all the detector calculations. Various parameters can be used to modify the calculations for a particular type of detector: the detector pixel size, number of pixels available, X-ray beam centre and which corner of the detector is used as the origin for pixel coordinates. Methods are available for calculating the $\mathbf{S}_1$ vector from a pixel position and *vice versa*, and for calculating the reflection 2θ angle given a pixel position.

A `Goniometer` class contains goniometer calculations, implementing the equations in Section 1.1.4.2. Methods are available to calculate the $\mathbf{h}_4$ vector from an *hkl* index and *vice versa*, and also to calculate scan angles for a given *hkl* index. As this class uses an instance of the `Detector` class internally, single methods are also available to convert directly between *hkl* indices and pixel positions.

The goniometer calculations are designed to be as general as possible to allow machines with different angle conventions to use the same code seamlessly. All calculations internally use left-handed rotations for every angle and the Busing & Levy coordinate conventions. As previously described, Bruker diffractometers use different angle and coordinate conventions. The `BrukerGoniometer` class inherits from `Goniometer`, so it can be used wherever code expects a `Goniometer` object without modifying that code.

Within this `BrukerGoniometer` class, the right-handed 2θ and ω rotations are inverted when set and again when read out again, so that internally they become left-handed rotations but external code never sees the conversion. The **UB** matrix is also transformed in a similar fashion by the matrix in Equation 7.3 to convert it to Busing & Levy (1967) coordinates and by $\mathbf{T}_{UB}^{-1}$ when it is read out again.

$$\mathbf{T}_{UB} = \begin{pmatrix} 0 & -1 & 0 \\ 1 & 0 & 0 \\ 0 & 0 & 1 \end{pmatrix} \tag{7.3}$$

7.2.3 Input/Output

Many different types of file are written as data are collected and the crystal structure is solved and refined. These files contain much useful information that would be useful to access programatically. As there is no standard library for reading these file formats, code has been written in libcrystal for this purpose.

7.2.3.1 Bruker Frame Files

Each frame file contains one diffraction image with a header information about the instrument at the time the frame was collected. This information includes goniometer angles, X-ray wavelength, exposure time and much more. The header section is in plain text using ASCII encoding. Each header item is 80 characters long with a seven byte item name followed by a colon character, ':', then the remaining 72 characters contain data separated by spaces, the number and type of which depend on the item name.

The length of the header is determined by the number of 512-byte blocks are present. As each header item is 80 bytes long, this means that the number of blocks must be a multiple of 5. This is specified with an item in the header named `HDRBLKS`. The code which reads the frame files assumes there must be at least 5 blocks in the file, within which the `HDRBLKS` item will be found, specifying how many further blocks to read. All the frame files collected with the Xiphos have 15 header blocks, making the header 7 680 bytes long and consisting of 96 lines. As there may not be 96 items the last few lines may contain arbitrary data as padding.

The diffraction image comes after the header as a series of binary intensity values read row-by-row. The number of bytes used to represent each pixel intensity is specified in the header and may be 1, 2 or 4. Intensity values that are too large to fit in the number of bytes available per pixel are represented by the largest possible value within the image (*i.e.* 255 for 1 byte, and 65 535 for 2 bytes) and the true value can be found from an overflow table after the diffraction image. The size of this overflow table is also specified in the header. A base offset is also specified in the header which should be added to each intensity value to get the true value.

The pixel values are specified in little-endian format, which means that the least significant byte is specified first, then the next most significant, and so on. For example, a two byte value of `0x1234` would be represented in memory as two bytes of `34` and `12`. This must be taken into account when reading intensity values if they use more than one byte.

The format of the overflows is different depending on the frame format as specified in the header. For older style frames the format is '86' and in these images the overflow table is specified in ASCII. Each overflow value uses 9 bytes for the decimal representation of the true intensity, followed by 7 bytes for the pixel position in the image. This table uses a multiple of 512 bytes like the header, potentially including padding at the end. Any pixels containing 0 also use this table to look up underflows, *i.e.* an intensity less than the base offset.

Listing 7.2: Using the `BrukerFrame` class to read frame files and convert them to *PNG* images.

```
BrukerFrame *frame;

try {
  frame = BrukerFrame::read(filename, true);
} catch (Crystal::IOException &e) {
  fprintf(stderr, "%s: %s\n", filename, e.what());
  return;
}

write_png(frame->image_rows, frame->image_cols, frame->image, output);
```

For newer style frames, *i.e.* those written by *BIS*, the format is '100' and the overflow tables contain binary values like the rest of the image. If the image uses 1 byte per pixel, there will be two overflow tables: one containing 2 byte values, and another containing 4 byte values in case any intensity value also overflows the first overflow table. These tables use a multiple of 16 bytes of storage. The overflows are listed sequentially in the order they are encountered in the image, so a count of the number of overflows that have been read from each table must be kept as the image is read. A separate table contains the underflows, if any exist, which is also padded to a multiple of 16 bytes, and is found before the overflow tables. If the number of underflows is 0, there should be no intensity values of 0 in the image, but if the number of underflows is –1, all values of 0 should be left as they are.

The `BrukerFrame` class hides all these details so that frame images can be read with a minimal number of lines of code. An example is shown in Listing 7.2, with an excerpt of the code used to generate the frame images in this work. The image is a simple array of integer values containing the pixel intensity, each row directly following the previous one in memory.

7.2.3.2 Bruker P4P Files

P4P files contain various useful data that is produced after the frames are collected, such as the unit cell and lattice type, chemical formula, crystal colour and shape, X-ray beam centre and goniometer angle offsets. Many of these are provided before data collection starts and are therefore written into the frame headers, but are subsequently refined during data integration. These values are required by *Masquerade*, for example for producing more accurate mask files, so the refined values from the *P4P* file are preferred to those in the frame headers.

Listing 7.3: Using the `BrukerP4P` class to read the first (or only) unit cell from a *P4P* file.

```
BrukerP4P p4p;

try {
    p4p.readFile(filename);
} catch (IOException &e) {
    fprintf(stderr, "Could not read p4p file: %s\n", e.what());
    return;
}

UnitCell cell = p4p.unitCell();
printf("Unit cell: %lf %lf %lf %lf %lf %lf\n",
    cell.a(), cell.b(), cell.c(), cell.alpha().degrees(),
    cell.beta().degrees(), cell.gamma().degrees());
```

These files have a simple format where each line is processed as a separate item. The line begins with a text string describing the data, followed by a space and then the data itself that is separated by further white-space. The format of this data depends on what it contains. For example, if there is only one unit cell in the file, the line will begin with `CELL`, followed by seven floating-point numbers containing *a*, *b*, *c*, α, β, γ and the cell volume respectively. The cell ESDs are specified on another line starting with `CELLSD`, followed by another seven numbers.

If more than one crystal component is present, as in the case of the two twin components in **6** at 290 K, various item names have numbers appended. Hence, the *P4P* file produced in during integration of this compound contains `CELL` and `CELL2`. The orientation matrix is split into rows already (`ORT1`, `ORT2` and `ORT3`), so the orientation matrix of the other component is specified by `ORT12`, `ORT22` and `ORT32`.

The *P4P* reading code reads this information and performs all the number reading, allowing programs using it to read the file and directly extract useful information from it. A trivial example is shown in Listing 7.3. This shows a number of useful features of `libcrystal`, such as the `UnitCell` class and the `Angle` class which is used for the cell angles that aids conversion between degrees and radians while avoiding confusion about which representation an angle is currently using.

7.3 Conclusions

A new suite of software programs known collectively as *XiphosTools* have been described. These programs provide extremely useful functionality for working with the two Xiphos systems, by providing remote monitoring capabilities, simple but powerful control over the generator power levels and a means to connect the cryosystem to the existing Bruker software as well as allowing remote control of the sample temperature.

In addition to this, a further library of code has also been written to ease the task of working with the data once it has been collected. This forms the back-bone of the previously described *Masquerade* program but could also be used for many more utilities.

Chapter 8

Conclusions and Future Work

The XIPHOS is one of very few single-crystal diffractometers capable of collecting data from crystals cooled to 2 K. Where such diffractometers do exist they are mostly installed in central facilities and operate with neutron radiation rather than X-rays, *e.g.* VIVALDI at the ILL (Wilkinson *et al.*, 2002), or SXD at ISIS (Keen *et al.*, 2006). Neutron diffraction offers valuable information that is more difficult or impossible to obtain with X-rays, particularly with regard to hydrogen atom positions, but also has drawbacks such as a requirement for larger crystals and longer experimental time, due to the lower flux available compared to most X-ray sources.

8.1 The XIPHOS Diffractometer

The XIPHOS offers X-ray diffraction in a laboratory environment and allows studies to be routinely performed with small crystals at ultra low temperatures without requiring an application period before an experiment can be carried out. The ability to collect data on crystals at 2 K allows experiments to be performed in order to improve understanding of the relationship between the solid-state structure and the physical properties of many materials which show interesting and valuable behaviour at ultra low temperatures. Examples of these materials include molecular conductors and superconductors, radical systems and single molecule magnets. Structural studies of materials from all these categories have been presented in this thesis.

Several materials were studied with the XIPHOS that exhibited changes in magnetic behaviour at temperatures below 30 K. Full structural analyses have been presented above and below the temperatures at which the magnetic changes occurred for $[CoL_2](BF_4)_2$ (**4a**;

Chapter 5), 3-cyanobenzo-1,3,2-dithiazolyl (**5**; Chapter 6) and $[p\text{–}ClC_6H_4NH_3]_2CuCl_4$ (**6**; Chapter 6). Due to the difficulty in measuring data at these temperatures it was previously unknown whether the magnetic changes were accompanied by any structural changes. The results of these studies found in each case that they were not; the crystal structures remained identical both above and below the temperatures of interest.

A crystallographic phase transition was, however, discovered in **6** at temperatures much closer to room temperature. At ~ 275 K the crystal undergoes a transition from the monoclinic $P2_1/c$ to the orthorhombic $Pccn$ with an accompanying doubling of the unit cell. This change was observed with the Xiphos and will be explored more thoroughly in a forthcoming publication (Thomson *et al.*, 2012).

A study has also been presented on a charge-transfer salt which undergoes a transition to a superconducting state at 7 K, β″–(BEDT–TTF)$_4$[$(H_3O)Ga(C_2O_4)_3$]$PhNO_2$ (**3a**; Chapter 4). Data on two crystals of this material were measured at a range of temperatures from 160 K to 2 K and no significant structural changes were found. However, a gradual breaking of the *c*-glide symmetry was found over the measured temperature range, which may be a result of increasing disorder in the Ga(oxalate) layer. At 160 K the crystal structure forms in $C2/c$ with a $PhNO_2$ guest molecule sitting on a two-fold rotation axis. By 2 K the $PhNO_2$ molecule is disordered over two positions, lowering the symmetry to $P\bar{1}$, but this process occurs gradually over the temperature range and the effect is more noticeable as the thermal displacement parameters shrink. This suggests that the disorder is present at all temperatures but is masked by the thermal motion at higher temperatures, thus the average structure shows the $C2/c$ symmetry. The related complex β″–(BEDT–TTF)$_4$[$(H_3O)Fe(C_2O_4)_3$]$PhNO_2$ (**3b**; Chapter 4) that also exhibits superconductivity below 7 K was studied at 2 K, and shows the same gradual disorder of the $PhNO_2$ molecule and subsequent breaking of symmetry.

8.2 *Masquerade*

The helium CCR used to reach the ultra low temperatures on the Xiphos requires two shrouds, for maintaining a vacuum around the crystal and shielding against radiation. These two shrouds are made from beryllium, which causes additional scattering from the primary X-ray beam and contaminates the diffraction pattern from the crystal. One solution to this problem would involve the use of Soller slits, as used on beamlines ID30 and more recently ID27 at the ESRF synchrotron facility (Mezouar *et al.*, 2002; Mezouar *et al.*, 2005). These are formed of concentric arcs containing slits arranged such that only

radiation from a particular origin position can pass through to the detector, hence eliminating any scattering from any other source such as the beryllium shrouds in a similar fashion to the point detector on the *Fddd* diffractometer described in Chapter 1. Although this would eliminate the requirement for *Masquerade*, such slits must be carefully aligned to the sample position. Given the range of movement available with the goniometer in both the crystal and the detector positions on the Xiphos this would place some major restrictions on the data collection strategy, which is already restricted by the centre of mass of the CCR.

If the Soller slits were attached to the detector the full range of movement of the goniometer would be accessible, but the detector would have to stay a fixed distance from the sample. It can be useful to move the detector in the case of strongly diffracting crystals or those with large unit cells in which the Bragg spots may overlap on the detector at closer distances, and so removing this ability would place additional restrictions on the types of materials that could be examined with the Xiphos. In contrast, if the slits were attached to the goniometer, they would have to cover a large angle of space which can be accessed by the detector, and would also restrict how close the detector could be moved to the sample. Attaching the slits to the shrouds instead would not be practical as the circumference of the shrouds is not equidistant from the sample position, as described in Chapter 3.

For these reasons, the solution deemed most suitable for use on the Xiphos system to remove the beryllium scattering employs software rather than physical means. A new program called *Masquerade* has been presented which calculates the scattering pattern resulting from the beryllium shrouds and generates 'masks' describing the position of the resulting rings on the detector for each measured diffraction image. The data integration program SAINT (Bruker, 2009), supplied by Bruker AXS, uses these masks to disregard reflections that are contaminated by the beryllium scattering. A new data collection protocol has also been presented which allows disregarded reflections to be measured with the detector at a different distance from the crystal, at which point they are no longer contaminated by beryllium scattering.

The use of *Masquerade* and the new data collection protocol has been tested with a small crystal of Cytidine (**2**; Chapter 3) at 100 K and 2 K and the results have been shown to improve the accuracy of the measured reflection intensities by reducing the internal R factor, R_{int}, as well as the agreement with the structure model in terms of R_1 and wR_2. In addition, the precision of the calculated bond lengths was found to be improved compared to the data that was integrated without masks. Two other compounds, **5** (Chapter 6) and $[ZnL_2](BF_4)_2$ (**4c**; Chapter 5) were also processed with *Masquerade* and the reflection intensity data was again found to be improved. Larger crystals which required shorter expo-

sure times per measured diffraction image were found to benefit to a smaller degree from the use of *Masquerade* than smaller crystals.

8.3 Future Work

Some work on estimating the partial charges of the symmetry-independent BEDT-TTF molecules in **3a** has suggested that the charges are unequal on each molecule at low temperatures but this is still uncertain. The underlying mechanism behind the superconductivity shown by this compound is still unexplained and more investigation is required to explain this phenomenon.

In addition, there are many more systems that display interesting and valuable physical properties at ultra low temperatures which could be studied with the Xiphos. By improving the understanding of the relationship between the solid-state structure and the physical properties of these materials, new materials could be synthesised that show the same solid-state structure and potentially the same physical properties at higher temperatures.

There are several extensions to the Xiphos system which could prove useful for studying an even wider range of materials. If an optical fibre could be introduced into the vacuum shrouds, as in the system described by Kusz *et al.* (2005), this would allow for studies of excited state systems at low temperatures, for instance spin-crossover materials that exhibit the LIESST effect. An alternative approach to introducing light into the vacuum shrouds involves the use of bright LEDs which can be placed within the shrouds. A prototype of such a system has already been built in the laboratory by Mr Sam Parry, which requires further testing to examine its efficacy.

A further modification to the Xiphos could reduce the need for *Masquerade* by replacing the beryllium shrouds with shrouds containing a different material such as Kapton®. This would reduce the background scattering and therefore would result in decreased contamination of the diffraction pattern from the crystal. One shroud made from aluminium foil has already been tested and was used during the collection of **5** and **6**. Although the background scattering was reduced, the lowest available temperature was increased to 3 K. A further shroud made from Kapton has also been made by Dr Mike Probert (Durham University) but testing is still ongoing.

An alternative shroud material, boron epoxy, has recently been introduced for use in high-pressure X-ray diffraction experiments (Lin *et al.*, 2003) and this may provide a superior replacement to Kapton for beryllium. Like Kapton, the material is amorphous and hence generates a more diffuse and smoother background that is easier to subtract during data

integration than the current beryllium shrouds. Additionally, like beryllium the material is more structurally rigid and may provide better shielding for thermal radiation, allowing lower base temperatures to be reached with the CCR. Although to the author's knowledge no vacuum shrouds such as those in use on the Xiphos have yet been made with boron epoxies, they would be worth investigation for use as shrouds if they are possible to manufacture.

Masquerade is currently operated through a command line interface and a GUI would make the program significantly easier to use, especially for users who are unfamiliar with command line programs. Another improvement concerns the calculation of the shroud offsets. Currently, the user must supply the pixel positions of a beryllium ring with a known scattering angle from three diffraction images, separated by 90˚ rotations about the z axis. This process could potentially be automated by designing an algorithm to determine the position of the strongest ring from the diffraction image, which would also improve the ease-of-use of the program.

As the Xiphos uses a detector and control software supplied by Bruker, *Masquerade* only supports Bruker image files at present. As the calculations for the ring positions are universal, the only changes required to support additional manufacturers would be to the pixel position calculations and for writing the resulting mask in a format which could be used by another integration program. This would make *Masquerade* useful on a wider range of diffractometers than is currently supported and allow better quality data to be collected with CCRs at low temperatures.

In conclusion, we have built a new diffractometer, the Xiphos, and demonstrated its effectiveness in the collection of the crystal structures presented in this thesis. We are now entering a new phase of operation to try to apply this machine to well specified problems in which the structural data obtained can provide insights and new understanding into the properties of exciting new materials with useful and desirable characteristics.

Appendix A

Conferences, Schools and Presentations

A.1 Conferences and Meetings

- CCG autumn meeting, 12th November 2008, Newcastle.
- BCA spring meeting, 20th–23rd April 2009, Loughborough. Presented a poster entitled 'Using Multiple Detector Positions to Overcome Beryllium Scattering'.
- ACA annual meeting, 25th–30th June 2009, Toronto, Canada. Presented a poster entitled 'Using Multiple Detector Positions to Overcome Beryllium Scattering'.
- CCG autumn meeting, 18th November 2009, Oxford.
- BCA spring meeting, 12th–15th April 2010, Warwick. Presented a poster entitled 'Functional Programming for Crystallographic Calculations'.
- ECM meeting, 29th August–2nd September 2010, Darmstadt, Germany. Presented a poster entitled 'Functional Programming for Crystallographic Calculations'.
- BCA spring meeting, 11th–14th April 2011, Keele. Presented a poster entitled 'Masquerade: Generating Masks for Beryllium Scattering'.
- IUCr meeting, 22nd-30th August 2011, Madrid, Spain. Presented a poster entitled 'Masquerade: Improving Data Quality with Masks for Beryllium Rings'.
- Bruker Users' Meeting, 9th May 2011, Chester-le-Street. Gave a talk entitled 'Interfacing with BIS (or how to make your life easier when collecting data)'.

A.2 Schools

Attended the 12th BCA/CCG Intensive Teaching School in X-Ray Structure Analysis from the 28th March to the 5th April, 2009.

A.3 Publications

Coome, J. A., Goeta, A. E., Howard, J. A. K., & Probert, M. R. (2012). "Masquerade: removing non-sample scattering from integrated reflection intensities". *J. Appl. Cryst.*, **45**(2), 292–298.

Probert, M. R., Robertson, C. M., Coome, J. A., Howard, J. A. K., Michell, B. C., & Goeta, A. E. (2010). "The XIPHOS diffraction facility for extreme sample conditions". *J. Appl. Cryst.*, **43**(6), 1415–1418.

Appendix B

Experimental Data for Charge Transfer Salts

Table B.1: Crystal data and structure refinement of **3a** (crystal 2) at all the temperatures measured, in space group $C2/c$.

Empirical formula		$C_{52}H_{40}GaNO_{15}S_{32}$	
Formula weight (g mol^{-1})		2014.49	
Crystal system, space group, Z		monoclinic, $C2/c$, 4	
Crystal size (mm^3)		0.6 × 0.18 × 0.15	
Crystal shape, colour		needle, black	
Temperature (K)	2.0(1)	10.0(1)	160.0(1)
a (Å)	10.2388(7)	10.2465(4)	10.2702(4)
b (Å)	19.7981(13)	19.8125(8)	19.8984(6)
c (Å)	34.871(2)	34.8797(14)	35.0689(11)
β (°)	93.452(2)	93.4310(10)	92.9980(10)
Volume (Å^3)	7055.8(8)	7068.2(5)	7156.9(4)
Calculated density (mg mm^{-3})	1.896	1.893	1.870
F(000)	4088	4088	4088
Wavelength λ, Mo K_α (Å)	0.71073	0.71073	0.71073
Absorption coefficient μ (mm^{-1})	1.403	1.401	1.384
Absorption correction type	multi-scan	multi-scan	multi-scan
Ratio min/max transmission	0.7309	0.6643	0.7430
Maximum 2θ (°)	52.84	52.74	52.76
No. of measured reflections	52066	48893	45696
No. of unique reflections	7211	7123	7017
R_{int}	0.0655	0.0589	0.0341
R_1, wR_2	0.0706, 0.1587	0.0717, 0.1585	0.0324, 0.0735
Data/restraints/parameters	7211/8/462	7123/2/462	7017/2/481
Goodness-of-fit on F^2	1.242	1.235	1.065
Largest diff. peak/hole (e Å^{-3})	1.580/−1.410	1.093/−1.163	0.762/−0.451

Table B.2: Crystal data and structure refinement of **3a** (crystal 2) at all the temperatures measured, in space group $P\bar{1}$.

Empirical formula		$C_{52}H_{40}GaNO_{15}S_{32}$	
Formula weight (g mol^{-1})		2014.49	
Crystal system, space group, Z		triclinic, $P\bar{1}$, 2	
Crystal size (mm^3)		$0.6 \times 0.18 \times 0.15$	
Crystal shape, colour		needle, black	
Temperature (K)	2.0(1)	10.0(1)	160.0(1)
a (Å)	10.2392(7)	10.2461(4)	10.2702(3)
b (Å)	11.1429(7)	11.1517(5)	11.1952(4)
c (Å)	34.872(2)	34.8786(14)	35.0695(11)
α (°)	88.328(2)	88.3930(10)	88.6070(10)
β (°)	86.549(2)	86.5700(10)	87.0020(10)
γ (°)	62.679(2)	62.6650(10)	62.7130(10)
Volume (Å^3)	3528.5(4)	3533.9(3)	3578.6(2)
Calculated density (mg mm^{-3})	1.896	1.893	1.870
F(000)	2044	2044	2044
Wavelength λ, Mo K_α (Å)	0.71073	0.71073	0.71073
Absorption coefficient μ (mm^{-1})	1.403	1.401	1.383
Absorption correction type	multi-scan	multi-scan	multi-scan
Ratio min/max transmission	0.7900	0.7437	0.7651
Maximum 2θ (°)	52.92	52.74	52.76
No. of measured reflections	55085	51412	46701
No. of unique reflections	13592	13657	13583
R_{int}	0.0432	0.0452	0.0308
R_1, wR_2	0.0636, 0.1404	0.0707, 0.1571	0.0367, 0.0793
Data/restraints/parameters	13592/4/884	13657/4/896	13583/3/933
Goodness-of-fit on F^2	1.321	1.292	1.054
Largest diff. peak/hole (e Å^{-3})	0.890/−1.216	1.843/−2.700	0.790/−0.435

Table B.3: Crystal data and structure refinement of **3a** (crystal 1) between 2 K and 20 K in space group $C2/c$.

Empirical formula	$C_{52}H_{40}GaNO_{15}S_{32}$					
Formula weight (g mol^{-1})	2014.49					
Crystal system, space group, Z	monoclinic, $C2/c$, 4					
Crystal size (mm^3)	$0.7 \times 0.25 \times 0.15$					
Crystal shape, colour	needle, black					
Temperature (K)	2.0(1)	3.0(1)	4.0(1)	5.0(1)	10.0(1)	20.0(1)
a (Å)	10.2460(3)	10.2460(3)	10.2468(3)	10.2456(3)	10.2458(3)	10.2465(3)
b (Å)	19.8138(5)	19.8104(6)	19.8105(6)	19.8119(6)	19.8136(5)	19.8146(6)
c (Å)	34.8981(10)	34.9001(10)	34.9026(10)	34.9016(10)	34.9083(9)	34.9128(10)
β (°)	93.4150(10)	93.4100(10)	93.4050(10)	93.3990(10)	93.4010(10)	93.3940(10)
Volume (Å^3)	7072.2(3)	7071.4(4)	7072.5(4)	7072.0(4)	7074.1(3)	7075.9(4)
Calculated density (mg mm^{-3})	1.892	1.892	1.892	1.892	1.891	1.891
F(000)	4088	4088	4088	4088	4088	4088
Wavelength λ, Mo K_α (Å)	0.71073	0.71073	0.71073	0.71073	0.71073	0.71073
Absorption coefficient μ (mm^{-1})	1.400	1.400	1.400	1.400	1.400	1.399
Absorption correction type	multi-scan	multi-scan	multi-scan	multi-scan	multi-scan	multi-scan
Ratio min/max transmission	0.8305	0.8236	0.8201	0.8224	0.8250	0.8189
Maximum 2θ (°)	52.78	52.78	52.78	52.78	52.82	52.78
No. of measured reflections	53263	53240	53231	53282	53295	53325
No. of unique reflections	7234	7235	7229	7235	7235	7237
R_{int}	0.0276	0.0272	0.0281	0.0281	0.0281	0.0292
R_1, wR_2	0.0549, 0.1234	0.0542, 0.1218	0.0541, 0.1218	0.0544, 0.1213	0.0533, 0.1196	0.0512, 0.1136
Data/restraints/parameters	7234/2/469	7235/2/469	7229/2/469	7235/2/469	7235/2/469	7237/2/469
Goodness-of-fit on F^2	1.448	1.442	1.439	1.444	1.442	1.436
Largest diff. peak/hole (e Å^{-3})	0.759/−0.691	0.730/−0.647	0.711/−0.801	0.715/−0.682	0.691/−0.715	0.814/−0.664

Table B.4: Crystal data and structure refinement of **3a** (crystal 1) between 40 K and 160 K in space group $C\,2/c$.

Empirical formula	$C_{52}H_{40}GaNO_{15}S_{32}$				
Formula weight (g mol^{-1})	2014.49				
Crystal system, space group, Z	monoclinic, $C\,2/c$, 4				
Crystal size (mm^3)	$0.7 \times 0.25 \times 0.15$				
Crystal shape, colour	needle, black				
Temperature (K)	40.0(1)	60.0(1)	80.0(1)	120.0(1)	160.0(1)
a (Å)	10.2481(3)	10.2518(2)	10.2532(2)	10.2594(2)	10.2652(2)
b (Å)	19.8199(5)	19.8279(5)	19.8380(5)	19.8708(5)	19.9042(5)
c (Å)	34.9244(9)	34.9596(8)	34.9815(8)	35.0418(8)	35.0949(9)
β (°)	93.3800(10)	93.3540(10)	93.2980(10)	93.1550(10)	92.9980(10)
Volume (Å^3)	7081.4(3)	7094.1(3)	7103.6(3)	7132.9(3)	7160.8(3)
Calculated density (mg mm^{-3})	1.890	1.886	1.884	1.876	1.869
F(000)	4088	4088	4088	4088	4088
Wavelength λ, Mo K_α (Å)	0.71073	0.71073	0.71073	0.71073	0.71073
Absorption coefficient μ (mm^{-1})	1.398	1.396	1.394	1.388	1.383
Absorption correction type	multi-scan	multi-scan	multi-scan	multi-scan	multi-scan
Ratio min/max transmission	0.8296	0.8280	0.8222	0.8277	0.8194
Maximum 2θ (°)	52.76	52.78	52.78	52.76	52.78
No. of measured reflections	53389	53581	53690	53903	54099
No. of unique reflections	7236	7249	7260	7283	7306
R_{int}	0.0279	0.0273	0.0276	0.0281	0.0295
R_1, wR_2	0.0428, 0.0887	0.0362, 0.0757	0.0315, 0.0695	0.0309, 0.0689	0.0301, 0.0691
Data/restraints/parameters	7236/2/469	7249/2/469	7260/2/469	7283/2/481	7306/2/481
Goodness-of-fit on F^2	1.395	1.285	1.171	1.119	1.074
Largest diff. peak/hole (e Å^{-3})	0.892/−0.706	0.801/−0.764	0.841/−0.719	0.869/−0.670	0.900/−0.647

Table B.5: Crystal data and structure refinement of **3a** (crystal 1) between 2 K and 20 K in space group $P\bar{1}$.

Empirical formula	$C_{52}H_{40}GaNO_{15}S_{32}$					
Formula weight (g mol^{-1})	2014.49					
Crystal system, space group, Z	triclinic, $P\bar{1}$, 2					
Crystal size (mm^3)	$0.7 \times 0.25 \times 0.15$					
Crystal shape, colour	needle, black					
Temperature (K)	2.0(1)	3.0(1)	4.0(1)	5.0(1)	10.0(1)	20.0(1)
a (Å)	10.2460(3)	10.2461(3)	10.2470(3)	10.2455(3)	10.2457(3)	10.2463(3)
b (Å)	11.1528(3)	11.1508(3)	11.1518(3)	11.1516(3)	11.1514(3)	11.1540(3)
c (Å)	34.8985(9)	34.8990(10)	34.9029(10)	34.9026(10)	34.9068(9)	34.9133(10)
α (°)	88.4430(10)	88.4400(10)	88.4430(10)	88.4420(10)	88.4410(10)	88.4510(10)
β (°)	86.5850(10)	86.5910(10)	86.5950(10)	86.6050(10)	86.6010(10)	86.6060(10)
γ (°)	62.6590(10)	62.6610(10)	62.6590(10)	62.6610(10)	62.6670(10)	62.6560(10)
Volume (Å^3)	3536.12(17)	3535.66(17)	3536.63(17)	3536.12(17)	3536.73(17)	3538.09(17)
Calculated density (mg mm^{-3})	1.892	1.892	1.892	1.892	1.892	1.891
F(000)	2044	2044	2044	2044	2044	2044
Wavelength λ, Mo K_α (Å)	0.71073	0.71073	0.71073	0.71073	0.71073	0.71073
Absorption coefficient μ (mm^{-1})	1.400	1.400	1.400	1.400	1.400	1.399
Absorption correction type	multi-scan	multi-scan	multi-scan	multi-scan	multi-scan	multi-scan
Ratio min/max transmission	0.8527	0.8506	0.8566	0.8566	0.8580	0.8515
Maximum 2θ (°)	52.78	52.78	52.78	52.78	52.76	52.8
No. of measured reflections	54023	54015	54026	54042	54061	54079
No. of unique reflections	14199	14200	14190	14199	14201	14211
R_{int}	0.0234	0.0234	0.0237	0.0238	0.0238	0.0247
R_1, wR_2	0.0599, 0.1315	0.0595, 0.1302	0.0588, 0.1293	0.0590, 0.1285	0.0583, 0.1270	0.0560, 0.1203
Data/restraints/parameters	14199/4/934	14200/4/934	14190/4/934	14199/4/934	14201/4/934	14211/4/934
Goodness-of-fit on F^2	1.460	1.450	1.448	1.458	1.452	1.436
Largest diff. peak/hole (e Å^{-3})	0.876/−0.694	0.853/−0.686	0.866/−0.716	0.839/−0.707	0.802/−0.774	0.783/−0.726

Table B.6: Crystal data and structure refinement of **3a** (crystal 1) between 40 K and 160 K in space group $P\bar{1}$.

Empirical formula	$C_{52}H_{40}GaNO_{15}S_{32}$				
Formula weight (g mol^{-1})	2014.49				
Crystal system, space group, Z	triclinic, $P\bar{1}$, 2				
Crystal size (mm^3)	$0.7 \times 0.25 \times 0.15$				
Crystal shape, colour	needle, black				
Temperature (K)	40.0(1)	60.0(1)	80.0(1)	120.0(1)	160.0(1)
a (Å)	10.2481(3)	10.2519(2)	10.2534(2)	10.2594(2)	10.2657(2)
b (Å)	11.1564(3)	11.1596(3)	11.1646(3)	11.1795(3)	11.1948(3)
c (Å)	34.9248(9)	34.9587(8)	34.9810(8)	35.0411(8)	35.0935(8)
α (°)	88.4500(10)	88.4540(10)	88.4770(10)	88.5340(10)	88.6040(10)
β (°)	86.6210(10)	86.6430(10)	86.7020(10)	86.8460(10)	87.0030(10)
γ (°)	62.6580(10)	62.6700(10)	62.6730(10)	62.7070(10)	62.7420(10)
Volume (Å^3)	3540.76(17)	3546.99(14)	3551.67(14)	3566.20(14)	3580.27(14)
Calculated density (mg mm^{-3})	1.890	1.886	1.884	1.876	1.869
F(000)	2044	2044	2044	2044	2044
Wavelength λ, Mo K_α (Å)	0.71073	0.71073	0.71073	0.71073	0.71073
Absorption coefficient μ (mm^{-1})	1.398	1.396	1.394	1.388	1.383
Absorption correction type	multi-scan	multi-scan	multi-scan	multi-scan	multi-scan
Ratio min/max transmission	0.8613	0.8610	0.8585	0.8622	0.8643
Maximum 2θ (°)	52.78	52.76	52.78	52.78	52.8
No. of measured reflections	54165	54323	54450	54662	54853
No. of unique reflections	14232	14247	14285	14320	14376
R_{int}	0.0244	0.0245	0.0250	0.0260	0.0273
R_1, wR_2	0.0468, 0.0939	0.0399, 0.0814	0.0355, 0.0746	0.0343, 0.0746	0.0347, 0.0755
Data/restraints/parameters	14232/4/934	14247/4/933	14285/4/933	14320/4/933	14376/3/957
Goodness-of-fit on F^2	1.373	1.258	1.157	1.104	1.058
Largest diff. peak/hole (e Å^{-3})	0.789/−0.767	0.809/−0.754	0.715/−0.708	0.757/−0.638	0.893/−0.614

References

Acker, D. S., Harder, R. J., Hertler, W. R., Mahler, W., Melby, L. R., Benson, R. E., & Mochel, W. E. (1960). *J. Am. Chem. Soc.*, **82**(24), 6408–6409.

Akutsu, H., Akutsu-Sato, A., Turner, S. S., Day, P., Tocher, D. A., Probert, M. R., Howard, J. A. K., Le Pevelen, D., Klehe, A.-K., Singleton, J., & Laukhin, V. N. (2003). *Syn. Metals*, **137**(1–3), 1239–1240.

Akutsu, H., Akutsu-Sato, A., Turner, S. S., Le Pevelen, D., Day, P., Laukhin, V., Klehe, A.-K., Singleton, J., Tocher, D. A., Probert, M. R., & Howard, J. A. K. (2002). *J. Am. Chem. Soc.*, **124**(42), 12430–12431.

Alberola, A., Collis, R. J., Humphrey, S. M., Less, R. J., & Rawson, J. M. (2006). *Inorg. Chem.*, **45**(5), 1903–1905.

Albertsson, J., Oskarsson, Å., & Ståhl, K. (1979). *J. Appl. Cryst.*, **12**(6), 537–544.

Aromí, G., Aubin, S. M., Bolcar, M. A., Christou, G., Eppley, H. J., Folting, K., Hendrickson, D. N., Huffman, J. C., Squire, R. C., Tsai, H.-L., Wang, S., & Wemple, M. W. (1998). *Polyhedron*, **17**(17), 3005–3020.

Baker, W. A., Jr. & Bobonich, H. M. (1964). *Inorg. Chem.*, **3**(8), 1184–1188.

Baldé, C., Desplanches, C., Grunert, M., Wei, Y., Gütlich, P., & Létard, J.-F. (2008). *Eur. J. Inorg. Chem.*, **2008**(34), 5382–5389.

Bardeen, J., Cooper, L. N., & Schrieffer, J. R. (1957). *Phys. Rev.*, **108**(5), 1175–1204.

Bechgaard, K., Carneiro, K., Olsen, M., Rasmussen, F. B., & Jacobsen, C. S. (1981). *Phys. Rev. Lett.*, **46**(13), 852–855.

Bruker (2009). SAINT, version 7.68a. Bruker AXS Inc., Madison, Wisconsin, USA.

Bruker (2010). APEX2, version 2010.1-2. Bruker AXS Inc., Madison, Wisconsin, USA.

Busing, W. R. & Levy, H. A. (1967). *Acta Cryst.*, **22**(4), 457–464.

Chapman, B., Jost, G., & van der Pas, R. (2007). *Using OpenMP: Portable Shared Memory Parallel Programming (Scientific and Engineering Computation)*. The MIT Press. ISBN 0262533022, 9780262533027.

Chen, L. & Craven, B. M. (1995). *Acta Cryst.*, B**51**(6), 1081–1097.

Chieh, C., Stokhuyzen, R., & Beck, A. (1977). *J. Appl. Cryst.*, **10**(3), 156–166.

Choudhury, A. R., Islam, K., Kirchner, M. T., Mehta, G., & Guru Row, T. N. (2004). *J. Am. Chem. Soc.*, **126**(39), 12274–12275.

Coffen, D. L. & Garrett, P. E. (1969). *Tetrahedron Lett.*, **10**(25), 2043–2046.

Coome, J. A., Goeta, A. E., Howard, J. A. K., & Probert, M. R. (2012). *J. Appl. Cryst.*, **45**(2), 292–298.

Copley, R. C. B., Goeta, A. E., Lehmann, C. W., Cole, J. C., Yufit, D. S., Howard, J. A. K., & Archer, J. M. (1997). *J. Appl. Cryst.*, **30**(3), 413–417.

Coppens, P., Ross, F. K., Blessing, R. H., Cooper, W. F., Larsen, F. K., Leipoldt, J. G., & Rees, B. (1974). *J. Appl. Cryst.*, **7**(3), 315–319.

Cornia, A., Fabretti, A. C., Sessoli, R., Sorace, L., Gatteschi, D., Barra, A.-L., Daiguebonne, C., & Roisnel, T. (2002). *Acta Cryst.*, C**58**(7), m371–m373.

Cosier, J. & Glazer, A. M. (1986). *J. Appl. Cryst.*, **19**(2), 105–107.

Debye, P. & Scherrer, P. (1916). *Physik Z.*, **17**, 277–283.

Decurtins, S., Gütlich, P., Hasselbach, K. M., Hauser, A., & Spiering, H. (1985). *Inorg. Chem.*, **24**(14), 2174–2178.

Dolomanov, O. V., Bourhis, L. J., Gildea, R. J., Howard, J. A. K., & Puschmann, H. (2009). *J. Appl. Cryst.*, **42**(2), 339–341.

Ewald, P. P. (1913). *Physik. Z.*, **14**, 465–472.

Farrell, A. (2012). Private communication.

Ferraris, J., Cowan, D. O., Walatka, V., & Perlstein, J. H. (1973). *J. Am. Chem. Soc.*, **95**(3), 948–949.

Flack, H. (1983). *Acta Cryst.*, A**39**(6), 876–881.

Flack, H. D. & Bernardinelli, G. (2000). *J. Appl. Cryst.*, **33**(4), 1143–1148.

Fukami, T., Akahoshi, S., Hukuda, K., & Yagi, T. (1987). *J. Phys. Soc. Jpn.*, **56**(6), 2223–2224.

Furberg, S. (1950). *Acta Cryst.*, **3**(5), 325–333.

Furberg, S., Peterson, C. S., & Rømming, C. (1965). *Acta Cryst.*, **18**(3), 313–320.

Galloway, K. W., Whyte, A. M., Wernsdorfer, W., Sanchez-Benitez, J., Kamenev, K. V., Parkin, A., Peacock, R. D., & Murrie, M. (2008). *Inorg. Chem.*, **47**(16), 7438–7442.

Ganguli, P., Gütlich, P., & Müller, E. W. (1982). *Inorg. Chem.*, **21**(9), 3429–3433.

Gatteschi, D. & Sessoli, R. (2003). *Angew. Chem., Int. Ed.*, **42**(3), 268–297.

Goeta, A. E. & Howard, J. A. K. (2004). *Chem. Soc. Rev.*, **33**(8), 490–500.

Gordon, P. (1949). *J. Appl. Phys.*, **20**(10), 908–917.

Graham, A. W., Kurmoo, M., & Day, P. (1995). *J. Chem. Soc., Chem. Commun.*, (20), 2061–2062.

Guionneau, P., Kepert, C. J., Bravic, G., Chasseau, D., Truter, M. R., Kurmoo, M., & Day, P. (1997). *Syn. Metals*, **86**(1–3), 1973–1974.

Guzei, I. A., Bikzhanova, G. A., Spencer, L. C., Timofeeva, T. V., Kinnibrugh, T. L., & Campana, C. F. (2008). *Cryst. Growth Des.*, **8**(7), 2411–2418.

Göbel, H. & Will, G. (1972). *Phys. Status Solidi B*, **50**(1), 147–154.

Gütlich, P., Garcia, Y., & Goodwin, H. A. (2000). *Chem. Soc. Rev.*, **29**(6), 419–427.

Gütlich, P., Hauser, A., & Spiering, H. (1994). *Angew. Chem., Int. Ed. Engl.*, **33**(20), 2024–2054.

Hahn, T., editor (2005). *International Tables for Crystallography, Volume A: Space-Group Symmetry*. Springer. ISBN 978-0-470-68908-0.

Hall, S. R. (1981). *Acta Cryst.*, A**37**(4), 517–525.

Henriksen, K., Larsen, F. K., & Rasmussen, S. E. (1986). *J. Appl. Cryst.*, **19**(5), 390–394.

Hohlwein, D. & Wright, A. F. (1981). *J. Appl. Cryst.*, **14**(2), 82–84.

Holland, J. M., Kilner, C. A., Thornton-Pett, M., & Halcrow, M. A. (2001a). *Polyhedron*, **20**(22-23), 2829–2840.

Holland, J. M., McAllister, J. A., Kilner, C. A., Thornton-Pett, M., Bridgeman, A. J., & Halcrow, M. A. (2002). *J. Chem. Soc., Dalton Trans.*, 548–554.

Holland, J. M., McAllister, J. A., Lu, Z., Kilner, C. A., Thornton-Pett, M., & Halcrow, M. A. (2001b). *Chem. Commun.*, 577–578.

Inglis, R., Jones, L. F., Karotsis, G., Collins, A., Parsons, S., Perlepes, S. P., Wernsdorfer, W., & Brechin, E. K. (2008). *Chem. Commun.*, 5924–5926.

Inglis, R., Taylor, S. M., Jones, L. F., Papaefstathiou, G. S., Perlepes, S. P., Datta, S., Hill, S., Wernsdorfer, W., & Brechin, E. K. (2009). *Dalton Trans.*, (42), 9157–9168.

Ishikawa, J., Asaji, T., & Nakamura, D. (1983). *J. Magn. Reson.*, **51**(1), 95–102.

Jérome, D., Mazaud, A., Ribault, M., & Bechgaard, K. (1980). *J. Physique Lett.*, **41**(4), 95–98.

Keen, D. A., Gutmann, M. J., & Wilson, C. C. (2006). *J. Appl. Cryst.*, **39**(5), 714–722.

Keesom, W. & Taconis, K. (1936). *Physica*, **3**(1--4), 237–242.

Kirchner, M. T., Das, D., & Boese, R. (2008). *Cryst. Growth Des.*, **8**(3), 763–765.

Kurmoo, M., Graham, A. W., Day, P., Coles, S. J., Hursthouse, M. B., Caulfield, J. L., Singleton, J., Pratt, F. L., & Hayes, W. (1995). *J. Am. Chem. Soc.*, **117**(49), 12209–12217.

Kusz, J., Schollmeyer, D., Spiering, H., & Gütlich, P. (2005). *J. Appl. Cryst.*, **38**(3), 528–536.

Langan, P., Robinson, R., Brown, P. J., Argyriou, D., Hendrickson, D., & Christou, G. (2001). *Acta Cryst.*, C**57**(8), 909–910.

Larsen, F. (1995). *Acta Cryst.*, B**51**(4), 468–482.

Leech, M. A., Solanki, N. K., Halcrow, M. A., Howard, J. A. K., & Dahaoui, S. (1999). *Chem. Commun.*, 2245–2246.

Lin, J.-F., Shu, J., Mao, H.-k., Hemley, R. J., & Shen, G. (2003). *Rev. Sci. Instrum.*, **74**(11), 4732–4736.

Lis, T. (1980). *Acta Cryst.*, B**36**(9), 2042–2046.

Little, W. A. (1964). *Phys. Rev.*, **134**(6A), A1416–A1424.

Little, W. A. (1965). *Sci. Am.*, **212**(2), 21.

Martin, L., S. Turner, S., Day, P., E. Mabbs, F., & J. L. McInnes, E. (1997). *Chem. Commun.*, 1367–1368.

Martin, L., Turner, S. S., Day, P., Guionneau, P., Howard, J. A. K., Hibbs, D. E., Light, M. E., Hursthouse, M. B., Uruichi, M., & Yakushi, K. (2001). *Inorg. Chem.*, **40**(6), 1363–1371.

McCoy, H. N. & Moore, W. C. (1911). *J. Am. Chem. Soc.*, **33**(3), 273–292.

McIntyre, G. J. (2009). Private communication.

Meserschmidt, M., Meyer, M., & Luger, P. (2003). *J. Appl. Cryst.*, **36**(6), 1452–1454.

Mezouar, M., Crichton, W. A., Bauchau, S., Thurel, F., Witsch, H., Torrecillas, F., Blattmann, G., Marion, P., Dabin, Y., Chavanne, J., Hignette, O., Morawe, C., & Borel, C. (2005). *J. Synchrotron Rad.*, **12**(5), 659–664.

Mezouar, M., Faure, P., Crichton, W., Rambert, N., Sitaud, B., Bauchau, S., & Blattmann, G. (2002). *Rev. Sci. Instrum.*, **73**(10), 3570–3574.

Mizuno, M., Garito, A. F., & Cava, M. P. (1978). *J. Chem. Soc., Chem. Commun.*, 18–19.

Money, V. A. (2004). *Structural Studies of Iron (II) Spin-Crossover Compounds*. Ph.D. thesis, University of Durham, UK.

Money, V. A., Radosavljevic Evans, I., Halcrow, M. A., Goeta, A. E., & Howard, J. A. K. (2003). *Chem. Commun.*, 158–159.

Montel, M. (1957). *X-ray Microscopy and Microradiography*, X-ray microscopy with catamegonic roof mirrors. Academic Press, New York, 177–185.

More, M., Odou, G., & Lefebvre, J. (1987). *Acta Cryst.*, B**43**(4), 398–405.

Mori, H. (2006). *J. Phys. Soc. Jpn.*, **75**(5), 051003.

Nelson, D. J., Chan, K., Cervantes-Lee, F., & ter Haar, L. W. (1996). *J. Appl. Phys.*, **79**(8), 4715–4717.

O'Boyle, N., Banck, M., James, C., Morley, C., Vandermeersch, T., & Hutchison, G. (2011). *J. Cheminf.*, **3**(1), 33.

Parkin, S. S. P., Engler, E. M., Schumaker, R. R., Lagier, R., Lee, V. Y., Scott, J. C., & Greene, R. L. (1983). *Phys. Rev. Lett.*, **50**(4), 270–273.

Post, B., Schwartz, R. S., & Fankuchen, I. (1951). *Rev. Sci. Instrum.*, **22**(3), 218–219.

Pozzi, C. G., Fantoni, A. C., Punte, G., & Goeta, A. E. (2009). *Chem. Phys.*, **358**(1–2), 68–74.

Probert, M. R. (2005). *Towards a Fuller Understanding of Selected Molecular Compounds*. Ph.D. thesis, University of Durham, UK.

Probert, M. R., Robertson, C. M., Coome, J. A., Howard, J. A. K., Michell, B. C., & Goeta, A. E. (2010). *J. Appl. Cryst.*, **43**(6), 1415–1418.

Rashid, S., Turner, S. S., Day, P., Howard, J. A. K., Guionneau, P., McInnes, E. J. L., Mabbs, F. E., Clark, R. J. H., Firth, S., & Biggs, T. (2001). *J. Mater. Chem.*, **11**(9), 2095–2101.

Rinehart, J. D., Fang, M., Evans, W. J., & Long, J. R. (2011). *Nat. Chem.*, **3**(7), 538–542.

Robertson, J. H. (1960). *J. Sci. Instrum.*, **37**(2), 41–45.

Rudman, R. & Godel, J. B. (1969). *J. Appl. Cryst.*, **2**(3), 109–112.

Samson, S., Goldish, E., & Dick, C. J. (1980). *J. Appl. Cryst.*, **13**(5), 425–432.

Sanner, I., Meißner, E., Köppen, H., Spiering, H., & Gütlich, P. (1984). *Chem. Phys.*, **86**(1-2), 227–233.

Schreurs, A. M. M., Xian, X., & Kroon-Batenburg, L. M. J. (2010). *J. Appl. Cryst.*, **43**(1), 70–82.

Schwenk, H., Parkin, S. S. P., Lee, V. Y., & Greene, R. L. (1986). *Phys. Rev. B*, **34**(5), 3156–3161.

Segall, M. D., Lindan, P. J. D., Probert, M. J., Pickard, C. J., Hasnip, P. J., Clark, S. J., & Payne, M. C. (2002). *J. Phys.: Condens. Matter*, **14**(11), 2717–2744.

Sekine, T., Okuno, T., & Awaga, K. (1996). *Mol. Cryst. Liq. Cryst.*, **279**(1), 65–72.

Sessoli, R., Gatteschi, D., Caneschi, A., & Novak, M. A. (1993). *Nature*, **365**(6442), 141–143.

Sheldrick, G. M. (2008a). *Acta Cryst.*, A**64**(1), 112–122.

Sheldrick, G. M. (2008b). XPREP, version 2008/2. Bruker AXS Inc., Madison, Wisconsin, USA.

Sheldrick, G. M. (2009). SADABS, version 2009/1. Bruker AXS Inc., Madison, Wisconsin, USA.

Shmueli, U., editor (1993). *International Tables for Crystallography*, volume B, 1.4.4. Kluwer Academic Publishers, 112.

Solanki, N. K., Leech, M. A., McInnes, E. J. L., Mabbs, F. E., Howard, J. A. K., Kilner, C. A., Rawson, J. M., & Halcrow, M. A. (2002). *J. Chem. Soc., Dalton Trans.*, 1295–1301.

Stamatatos, T. C., Foguet-Albiol, D., Stoumpos, C. C., Raptopoulou, C. P., Terzis, A., Wernsdorfer, W., Perlepes, S. P., & Christou, G. (2005). *J. Am. Chem. Soc.*, **127**(44), 15380–15381.

Streib, W. E. & Lipscomb, W. N. (1962). *Proc. Natl. Acad. Sci. U. S. A.*, **48**(6), 911–913.

Sun, S., Wu, P., Zhang, Q., & Zhu, D. (1998). *Syn. Metals*, **94**(2), 161–166.

Taniguchi, H., Miyashita, M., Uchiyama, K., Satoh, K., Môri, N., Okamoto, H., Miyagawa, K., Kanoda, K., Hedo, M., & Uwatoko, Y. (2003). *J. Phys. Soc. Jpn.*, **72**(3), 468.

Thomas, J. O. (1972). *J. Appl. Cryst.*, **5**(2), 102–106.

Thomson, R. I., Rawson, J. M., Carpenter, M. A., Goeta, A. E., Probert, M. R., Coome, J. A., & Tuan, H. K. A. (2012). "Elastic coupling and anelastic relaxation associated with multiple phase transitions in para-chloroanilinium tetrachlorocuprate, $[p\text{-}ClC_6H_4NH_3]_2CuCl_4$". Unpublished manuscript.

Vonnegut, B. & Warren, B. E. (1936). *J. Am. Chem. Soc.*, **58**(12), 2459–2461.

Wilkinson, C., Cowan, J. A., Myles, D. A. A., Cipriani, F., & McIntyre, G. J. (2002). *Neutron News*, **13**(1), 37–41.

Will, G., Göbel, H., Sampson, C. F., & Forsyth, J. B. (1972). *Phys. Lett. A*, **38**(3), 207–208.

Willett, R., Place, H., & Middleton, M. (1988). *J. Am. Chem. Soc.*, **110**(26), 8639–8650.

Woodard, C. L. & Straumanis, M. E. (1971). *J. Appl. Cryst.*, **4**(3), 201–204.

Woodley, M. J. A., Hine, R., & Richards, J. P. G. (1971). *J. Appl. Cryst.*, **4**(1), 9–12.

Young, R. A. (1966). *J. Sci. Instrum.*, **43**(7), 449.

Yufit, D. S. & Howard, J. A. K. (2010). *CrystEngComm*, **12**(3), 737–741.

Zobel, D., Luger, P., Dreissig, W., & Koritsanszky, T. (1992). *Acta Cryst.*, B**48**(6), 837–848.